

THE FILE COPY

(2)

WRDC-TR-89-4081

LASER PROBE VAPORIZATION/OXIDATION TESTING OF  
HIGH TEMPERATURE COMPOSITES



J.T. Porter  
G.H. Reynolds  
T.D. Kunz  
M.J. Berry

MSNW, Inc.  
P.O. Box 865  
San Marcos, CA 92069

DTIC  
ELECTE  
AUG 15 1989  
S D<sup>CS</sup> D

July 1989

Final Report for Period June 1987 - December 1987

AD-A211 410

Approved for Public Release; Distribution unlimited

MATERIALS LABORATORY  
WRIGHT RESEARCH AND DEVELOPMENT CENTER  
AIR FORCE SYSTEMS COMMAND  
WRIGHT-PATTERSON AIR FORCE BASE, OHIO 45433-6533

89

8

14

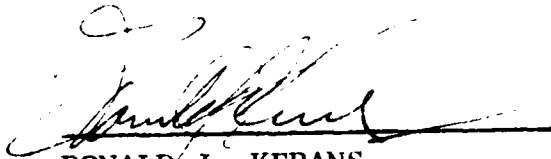
2

# NOTICE

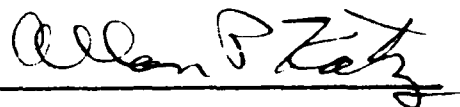
When Government drawings, specifications, or other data are used for any purpose other than in connection with a definitely Government-related procurement, the United States Government incurs no responsibility or any obligation whatsoever. The fact that the government may have formulated or in any way supplied the said drawings, specifications, or other data, is not to be regarded by implication, or otherwise in any manner construed, as licensing the holder, or any other person or corporation; or as conveying any rights or permission to manufacture, use, or sell any patented invention that may in any way be related thereto.

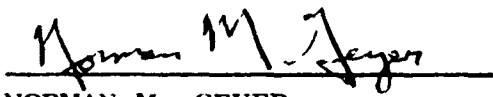
This report is releasable to the National Technical Information Service (NTIS). At NTIS, it will be available to the general public, including foreign nations.

This technical report has been reviewed and is approved for publication.

  
RONALD J. KERANS  
Project Engineer

FOR THE COMMANDER

  
ALLAN P. KATZ  
Technical Area Manager  
Processing and High Temperature  
Materials Branch  
Metals and Ceramics Division

  
NORMAN M. GEYER  
Acting Branch Chief  
Processing and High Temp Temperature  
Materials Branch  
Metals and Ceramics Division

If your address has changed, if you wish to be removed from our mailing list, or if the addressee is no longer employed by your organization please notify WRDC/MLLM, WPAFB, OH 45433-6533 to help us maintain a current mailing list.

Copies of this report should not be returned unless return is required by security considerations, contractual obligations, or notice on a specific document.

# REPORT DOCUMENTATION PAGE

Form Approved  
OMB No. 0704-0188

1a. REPORT SECURITY CLASSIFICATION <b>UNCLASSIFIED</b>			1b. RESTRICTIVE MARKINGS <b>NONE</b>		
2a. SECURITY CLASSIFICATION AUTHORITY			3. DISTRIBUTION/AVAILABILITY OF REPORT Approved for public release; distribution unlimited.		
2b. DECLASSIFICATION/DOWNGRADING SCHEDULE			5. MONITORING ORGANIZATION REPORT NUMBER(S) WRDC-TR-89-4081		
4. PERFORMING ORGANIZATION REPORT NUMBER(S)			7a. NAME OF MONITORING ORGANIZATION Materials Laboratory (WRDC/MLLM) Wright Research and Development Center		
6a. NAME OF PERFORMING ORGANIZATION MSNW, Inc		6b. OFFICE SYMBOL (if applicable)		7b. ADDRESS (City, State, and ZIP Code) Wright-Patterson AFB OH 45433-6533	
6c. ADDRESS (City, State, and ZIP Code) P. O. Box 865 San Marcos CA 92069			9. PROCUREMENT INSTRUMENT IDENTIFICATION NUMBER F33615-87-C-5275		
8a. NAME OF FUNDING/SPONSORING ORGANIZATION		8b. OFFICE SYMBOL (if applicable)		11. TITLE (Include Security Classification)  Laser Probe Vaporization/Oxidation Testing of High Temperature Composites	
8c. ADDRESS (City, State, and ZIP Code)			12. PERSONAL AUTHOR(S) J. T. Porter and G. H. Reynolds, MSNW, Inc. T. D. Kunz and M. J. Berry, Houston Area Rsch Ctr		
13a. TYPE OF REPORT Final		13b. TIME COVERED FROM 22Jun87 to 22Dec87		14. DATE OF REPORT (Year, Month, Day) 1989 July	
15. PAGE COUNT 103		16. SUPPLEMENTARY NOTATION  This is a Small Business Innovation Research Program Report, Phase I			
17. COSATI CODES			18. SUBJECT TERMS (Continue on reverse if necessary and identify by block number)		
FIELD	GROUP	SUB-GROUP	Laser Probe, Vaporization, Oxidation Ceramics		
19. ABSTRACT (Continue on reverse if necessary and identify by block number)  A laser probe technique for the determination of vaporization/oxidation processes of high temperature ceramics was investigated. The technique was found to provide meaningful data on the vapor species near the specimen surface. These data were correlated with changes in specimen microstructure and analyzed by thermochemical and kinetic modeling. Results were found to be in general agreement with the modeling.					
20. DISTRIBUTION/AVAILABILITY OF ABSTRACT <input type="checkbox"/> UNCLASSIFIED/UNLIMITED <input checked="" type="checkbox"/> SAME AS RPT. <input type="checkbox"/> DTIC USERS			21. ABSTRACT SECURITY CLASSIFICATION UNCLASSIFIED		
22a. NAME OF RESPONSIBLE INDIVIDUAL R. J. Kerans			22b. TELEPHONE (Include Area Code) (513) 255-9823		22c. OFFICE SYMBOL WRDC/MLLM

## TABLE OF CONTENTS

1.0	SUMMARY OF PHASE I ACCOMPLISHMENTS.....	1
2.0	MATERIALS.....	3
3.0	DETECTION OF SiO FROM LASER HEATED SAMPLES.....	4
3.1	EXPERIMENTAL APPROACH.....	4
3.2	THE A - X ELECTRONIC TRANSITION OF SiO.....	5
3.3.	FREQUENCY DOUBLING TO 235 nm for SiO DETECTION.....	6
4.0	EXPERIMENTAL RESULTS.....	7
4.1	CARBON FURNACE EXPERIMENTS.....	7
4.2	PLUME DETECTION OF SiO FROM PURE SiO SAMPLES.....	10
4.3	PLUME DETECTION OF SiO FROM MODEL SAMPLES.....	12
4.3.1	VACUUM, 5 TORR and 200 TORR OXYGEN EXPERIMENTS.....	12
4.4	PRE- AND POST-TEST MICROSTRUCTURAL CHARACTERIZATION.....	22
5.0	CORRELATION OF MODELING AND EXPERIMENTAL OBSERVATIONS.....	24
6.0	CONCLUSIONS AND RECOMMENDATIONS.....	26
	REFERENCES.....	29
	APPENDIX 1 - MODELING.....	A1
	APPENDIX 2 - SURFACE TEMPERATURES OF SMALL LASER-IRRADIATED TARGETS A16	



Accession	
NTIS	<input checked="" type="checkbox"/>
DTIC TAB	<input type="checkbox"/>
Unannounced	<input type="checkbox"/>
Justification	
By	
Distribution/	
Availability Codes	
Dist	Avail and/or Special
A-1	

# LASER PROBE VAPORIZATION/OXIDATION TESTING OF HIGH TEMPERATURE COMPOSITES

## 1.0 SUMMARY OF PHASE I ACCOMPLISHMENTS

The objectives of the laser probe investigation of vaporization/oxidation processes of high temperature composite materials were, first, to establish that this technique could provide meaningful data on vapor phase species in the near-surface environment of high temperature composite materials, second, to correlate these observations with changes in microstructure, third, to demonstrate the capability of the laser probe technique to produce useful characterization of bulk materials using microscale samples, and fourth, to carry out modeling to predict and/or explain the degradation reactions observed.

Using c.w. HF laser to heat the sample and a frequency doubled dye laser to monitor the SiO A-X transition, the laser probe clearly demonstrated the evolution of SiO under conditions of active oxidation in reference samples of high purity SiC and Si<sub>3</sub>N<sub>4</sub> in a SiC/SiC composite, and in both SiC- and Si<sub>3</sub>N<sub>4</sub>- coated carbon/carbon composites. Similarly, under passive oxidation conditions SiO<sub>2</sub> films were formed which, depending on the material homogeneity and thermochemical stability, provided varying degrees of oxidation protection. These tests were all carried out on samples of the order of 3 mm square and 1 mm thick. SEM examination of pre-test and post-test samples of each material showed clear changes in surface morphology under the different conditions of active and passive oxidation. Both the active and passive oxidation results are in general agreement with the expectations from thermochemical and kinetic modeling.

The technique provides a rapid and convenient way to vary the temperature at a constant oxygen partial pressure within the active oxidation regime. Therefore, if the processes responsible for active oxidation are gas phase mass transport controlled, only a small and predictable variation of the rate would be expected. If, however, the

processes are controlled by a chemical reaction, then this process should show a substantial heat of activation and the oxidation rate should show a strong temperature dependence. Other laser frequencies or complimentary techniques such as mass spectrometry could be used to follow the degradation of other constituents, such as boron-based inhibitors or active oxidation of carbon.

Section 2. describes the materials examined in this study. Sections 3. and 4. describe the laser probe technique, present the laser probe test results for samples at varying oxygen pressures and observations on the pretest and post-test surface morphology examinations. Section 5. considers the correlation of the observations with modeling predictions. Section 6. summarizes the results of the study and presents recommendations for extension of laser probe investigations of high temperature materials. Appendix 1 presents the underlying modeling considerations, and Appendix 2 presents a one dimensional heat transfer analysis carried out to characterize the expected thermal behavior of samples under laser heating.

## 2.0 MATERIALS SELECTION

Six experimental materials and one reference material (pure "SiO") were utilized in the Phase I program. The experimental materials were as follow:

<u>I.D.</u>	<u>Material</u>	<u>Supplier</u>
MS1	NC430 High Purity SiC	Norton
MS2	NC432 High Purity Si <sub>3</sub> N <sub>4</sub>	Norton
MS3	S.E.P. SiC/SiC Composite	Williams International
MS6	Resin-Densified, Boron-Inhibited Carbon-Carbon Composite	G.A. Technologies
MS7	Same as MS6 but with CVD SiC Coating (Chromalloy)	G.A. Technologies
MS8	LTV ACC-4 Carbon-Carbon Substrate with CVD Si <sub>3</sub> N <sub>4</sub> Coating	United Technologies Research Center

Three other materials were procured but not tested in this program B.F. Goodrich boron-inhibited, CVD-densified carbon-carbon with and without a CVD SiC coating (redundant with MS6, 7) and Babcock and Wilcox AlN-SiC/BN hot pressed composite (eliminated on the basis of PRDA contract results).

Samples were generally diamond saw cut to either a square or round shape, 2-3 mm on a side or diameter, and about 1 mm in thickness. A comparison of the pre- and post-test microstructural characterization of each material is presented in section 4.3.

### 3.0 DETECTION of SiO FROM LASER HEATED SAMPLES

#### 3.1 EXPERIMENTAL APPROACH

Our experimental approach to in situ direct absorption gas phase monitoring of SiO generated from the test samples above entailed 4 distinct steps:

- 1) generation of the appropriate wavelength light for detection of the SiO A - X electronic transition, discussed in Section 3.2.
- 2) detection of SiO by direct absorption in a carbon furnace, discussed in Section 4.1.
- 3) detection of SiO generated from a laser heated SiO sample, discussed in Section 4.2.
- 4) detection of SiO from the laser heated model test samples (MS1-3, MS6-8), discussed in Section 4.3.

"Pure SiO" (99.95%, 3/8 + 10 mesh size) was obtained from Alfa Products. No detailed pre-test properties of any of the materials were conveyed to us. Therefore, we proceeded empirically through the entire laser heating portion of this work. Additionally, a consultant, Dr. Marshall Sparks (BDM Corp.) was employed to model these "1 dimensional" heating experiments. His results, applicable to the experiments described in section 4.3, help predict the final temperature of small target samples under cw laser irradiation. In part, his results state: if a) the transmittance of the target is zero, b) the thermal time constant for thermal diffusion over the target radius and target thickness are short with respect to the heating time, and c) the absorptance and emittance are from very thin surface layers, then the final temperature of the sample is given by:

$$T_f = (P/\epsilon\sigma_{SB}A_s)^{1/4}$$

where P is the absorbed laser power,  $\epsilon$  is the reradiation emittance ( $\leq 1$ ),  $\sigma_{SB}$  is the Stefan-Boltzmann constant and  $A_s$  is the sample surface area.



### 3.2 THE A - X ELECTRONIC TRANSITION of SiO

The SiO A - X electronic transition (Reference 1) is composed of several vibrational transitions, and each vibrational transition is composed of three rotational branches: P ( $\Delta J = -1$ ), Q ( $\Delta J = 0$ ), and R ( $\Delta J = +1$ ). Each rotational branch is composed of many rotational lines. Figure 1 shows a computer simulated SiO spectrum for the (0,0) vibrational band. The top three panels show the individual P, Q, and R branches; the bottom panel shows the entire A - X (0,0) band (P, Q, and R branches convoluted together). Individual line intensities were calculated by multiplying the Hönl - London line strength factor (Reference 2) by the Boltzmann population for each lower rotational quantum state. This simulated spectrum was generated from rotational constants that are a "best fit" (Reference 1) to experimental line positions, and therefore, is not totally accurate. For example, line positions for large J values ( $J > 60$ ) may be substantially ( $0.5 \text{ cm}^{-1}$ ) off, and the "pile - ups" (positions where 2 or more rotational lines have nearly the same central frequency, thereby appearing as a single intense absorption) may be shifted to some other wavelength location.

As a matter of convenience, we have chosen to record SiO spectra in the A - X (0,0) Q(18), P(13), and R(26) wavelength region located at approximately  $42,606 \text{ cm}^{-1}$ . This convenience arises, in part, from the chance wavelength coincidence between the SiO Q(18) absorption line (at  $2\omega = 42,606.86 \text{ cm}^{-1}$ , or  $\omega = 21303.43 \text{ cm}^{-1}$ ) and an intense tellurium absorption line (at  $\omega = 21303.47 \text{ cm}^{-1}$ ). The tellurium absorption line(s) provide absolute wavelength calibrations for the computer controlled laser absorption spectrometer (CCLAS, described below). Figure 2 shows a higher resolution plot of the computer simulated SiO (0,0) spectrum in this wavelength region. Experimental line positions (Reference 1) were used to convolute this high resolution simulated spectrum.

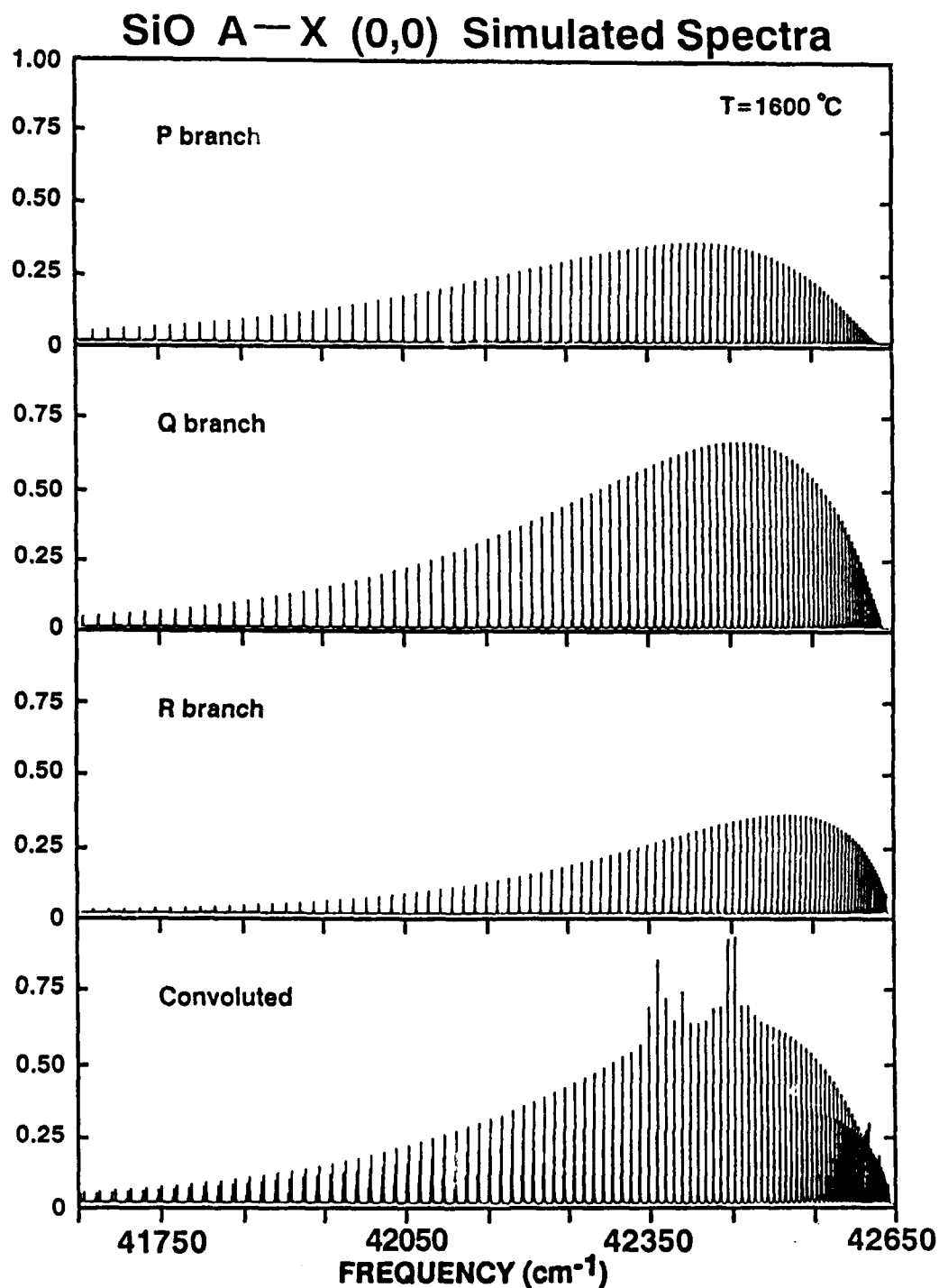


**Figure 1:** Simulated SiO A - X (0,0) electronic transition. Intensities were calculated from the Boltzmann distribution at 1600 C and the Hönl - London line strength factors; a 0.20 cm<sup>-1</sup> FWHM Lorentzian lineshape was imposed on each rotational line. The top 3 panels show only the P branch, Q branch, and R branch, respectively; the bottom panel shows the entire convoluted spectrum. Rotational constants for this simulation were calculated from a "best fit" to experimental line positions (Reference 1). See Figure 2 for a higher resolution plot and labels of individual rotational transitions.

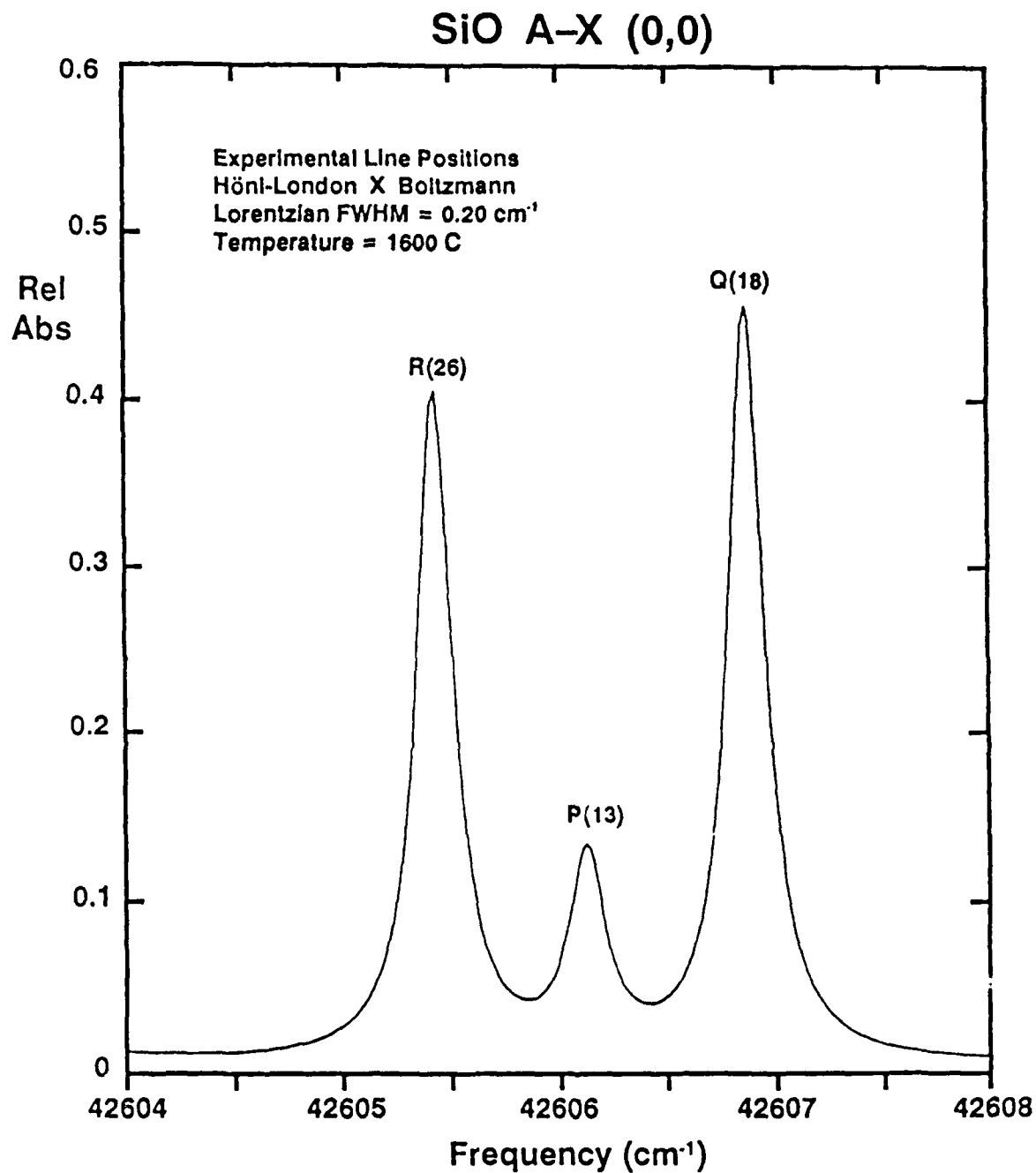


**Figure 2:** Simulated high resolution plot of the SiO A - X (0,0) electronic transition from 42604 cm<sup>-1</sup> to 42608 cm<sup>-1</sup>. Rotational line intensities were calculated from the Boltzmann distribution at 1600 C and the Hönl - London line strength factors; a 0.20 cm<sup>-1</sup> FWHM Lorentzian lineshape was imposed on each rotational line. Experimental line positions were taken from Reference 1.

### 3.3 FREQUENCY DOUBLING TO 235 nm for SiO DETECTION

In order to detect the A - X electronic transition of SiO by direct absorption, tunable light around 235 nm had to be generated. This was accomplished by frequency doubling a tunable, narrow bandwidth ring dye laser. The experimental apparatus, a computer controlled laser absorption spectrometer (CCLAS), is shown schematically in Figure 3. A krypton ion laser (4.5 W, all lines violet) pumped coumarin 460 dye in the ring dye laser. Approximately 400 mW was output coupled from the ring dye laser and optimally focussed by a 100 mm focal length lens into a 65 degree z-cut beta barium borate crystal (BBO, obtained from CSK, Co.). The fundamental and frequency doubled light were separated by a series of three quartz prisms (i.e., a beam discriminator); the frequency doubled power was approximately 1.5 - 2  $\mu$ W.

In order to obtain frequency doubled light, the BBO crystal must be "phase matched". That is, as a function of wavelength, the crystal must be angle tuned about its z - optical axis in order to generate frequency doubled light. Without angle tuning the crystal, phase matching still occurs over approximately a 10  $\text{cm}^{-1}$  interval. With the current setup, a complication for scanning wavelength ranges larger than 10  $\text{cm}^{-1}$  arises from beam walkoff. As the dye laser wavelength is changed and phase matching conditions are maintained by angle tuning the BBO crystal, the frequency doubled light emerges from the beam discriminator at a slightly different angle thereby altering the intended path of the frequency doubled beam. Therefore, the wavelength scanning range was limited to a narrow wavelength range for these experiments.

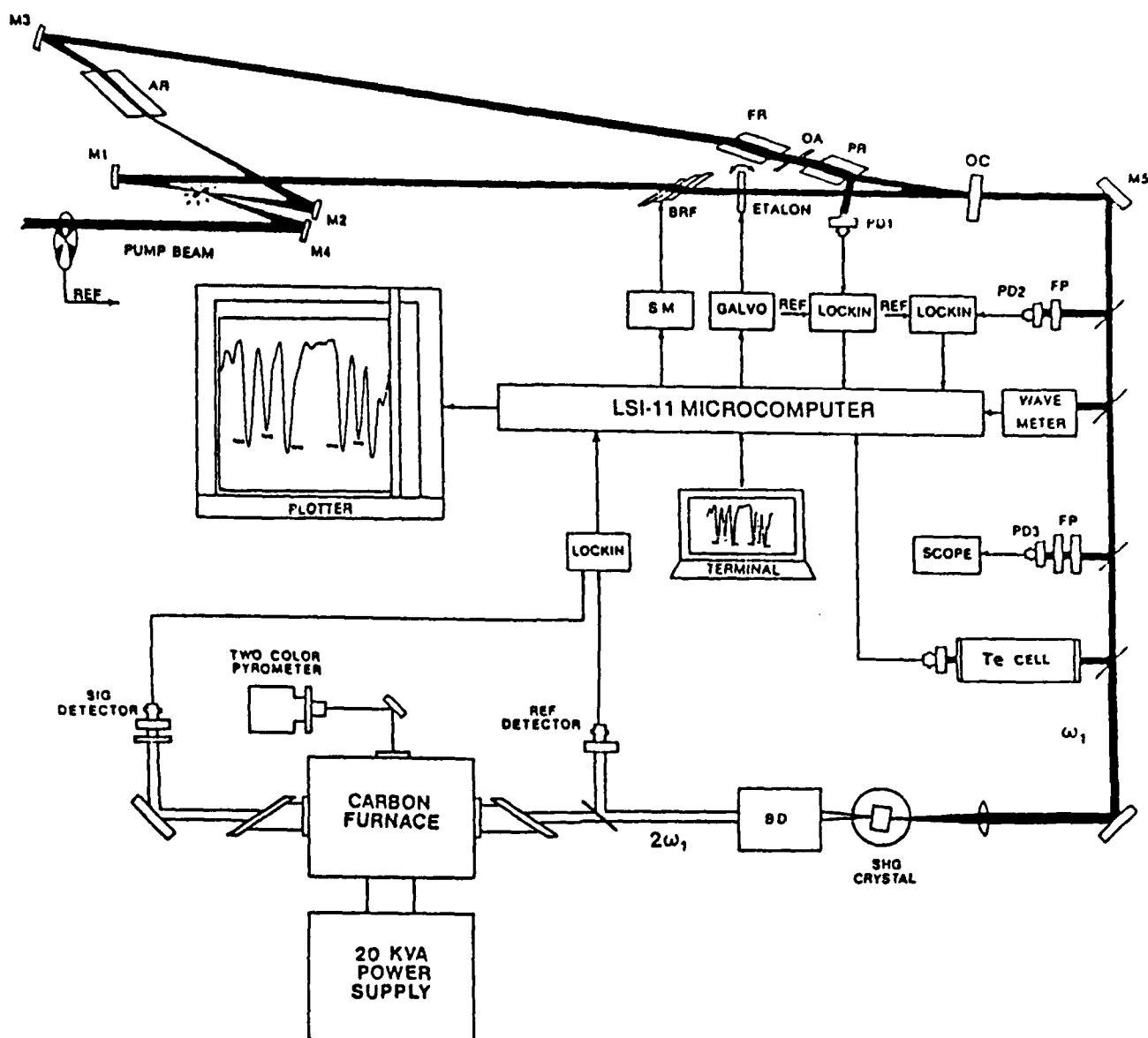


**Figure 3:** Schematic diagram of the computer controlled laser absorption spectrometer (CCLAS system) and carbon furnace. A near single frequency cw tunable dye laser is pumped by an ion laser. CCLAS produces the complete spectrum of visible laser radiation with a wide variety of organic dyes. UV light is produced by second harmonic generation (SHG) by either external cavity frequency doubling (beta barium borate, BBO, as shown) or intracavity frequency doubling (KDP, not shown) nonlinear crystals. For detection of the SiO A - X (0,0) electronic transition, coumarin 460 laser dye was pumped by the all lines violet output of a  $\text{Kr}^+$  laser, and the BBO crystal was phase matched at approximately 58 degrees. Among other diagnostics, a tellurium absorption cell monitored the laser wavelength accurately. An optical pyrometer was used to measure furnace temperature. Absorption data was acquired, processed, and plotted using a microcomputer system.

## 4.0 EXPERIMENTAL RESULTS

### 4.1 CARBON FURNACE EXPERIMENTS

Experiments were first conducted on "pure SiO" to obtain a sample spectrum of the SiO A - X (0,0) band to verify experimental performance of the CCLAS system. Due to the phase matching requirements of the BBO frequency doubling crystal (see section 3.3 above) only a short spectral region could be scanned before crystal realignment was required. Therefore, wavelength scans were limited to less than a  $10 \text{ cm}^{-1}$  range.

An Astro carbon furnace (model 1000-2560-FP20) was modified with custom top and bottom hearths and heating element made of purified (99.999%) carbon. A tantalum crucible containing SiO chunks, supported by the bottom hearth, was positioned in the center of the heated zone. Furnace temperature was measured by focussing an optical pyrometer on the outside wall of the carbon heating element; the pyrometer viewed the center portion of the heating element through a side port oriented perpendicular to the dye laser beam path.

The frequency doubled light was steered along the longitudinal axis of the furnace; entrance and exit ports were 3" suprasil windows. Transmitted light was detected and monitored by a UV sensitive photodiode (Hamamatsu S1336-5BQ). Blackbody radiation from the furnace was reduced by an optical filter (Corning 7-54). Chopping the krypton ion pump beam provided the means to incorporate phase sensitive detection in all subsequent experiments. The apparatus is shown schematically in Figure 3.

Figure 4 shows a typical scan obtained from CCLAS probing gaseous SiO in the carbon furnace. The top panel is the tellurium wavelength reference spectrum; the bottom panel is the SiO spectrum plotted in percent transmission vs. wavelength. Note the chance location of the Te reference absorption line in relation to the SiO Q(18) absorption line. At a temperature of 1400 C, the Q(18) line is absorbing almost 100 % of the incident light.

Several differing values of the oscillator strength for the entire SiO A - X (0,0) vibrational band have been reported in the literature (References 3 - 5). An "order of magnitude" absorption cross section,  $\sigma$ , for the

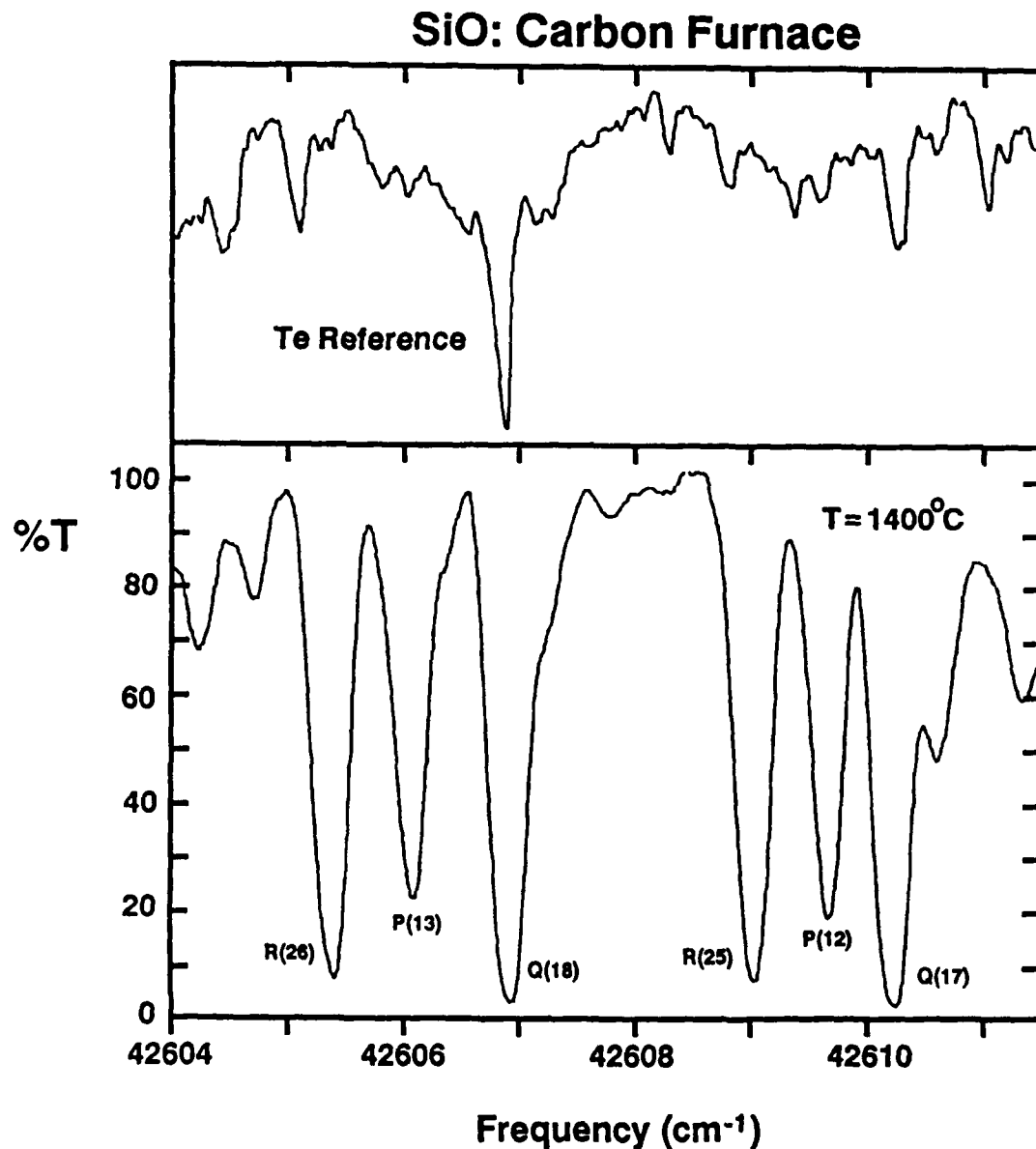


**Figure 4:** Experimental absorption spectrum of "pure" SiO heated to temperature in a carbon furnace. The top plot shows the Te absorption reference spectrum used to accurately monitor the dye laser wavelength. The six labeled absorption peaks in the bottom panel are due to individual rotational transitions in the (0,0) vibrational band of the SiO A - X electronic transition (see Figures 1 and 2 for computer simulations). The temperature, read by an optical pyrometer focused on the outer surface of the carbon heating element, may be incorrect by approximately 100 degrees (see text for discussion).

individual Q(18) rotational line can be estimated from Reference 3 by considering: 1) the absorption cross section for the entire SiO (0,0) band is approximately  $7 \times 10^{-17}$  cm<sup>2</sup>/molecule, 2) more than 400 rotational lines (125 in each P, Q, and R branch) make up the (0,0) vibrational band (see Figure 1), 3) half of the band's intensity is in the Q branch, and 4) the Q(18) line is approximately 50% of the average Q branch intensity. Therefore, a rough estimate of the absorption cross section for the single Q(18) rotational transition is:

$$\begin{aligned}\sigma &= [7 \times 10^{-17} / (400)] \times [2/2] \\ &= 2 \times 10^{-19} \text{ cm}^2/\text{molecule}.\end{aligned}$$

Percent absorption can be calculated from the equation:

$$\text{Abs} = 1 - \exp(-\sigma NL)$$

where N is the number density (molecules/cm<sup>3</sup>), L is the path length (cm), and  $\sigma$  is the absorption cross section (cm<sup>2</sup>/molecule). At an observed outer heating element temperature surface of 1400 C, therefore an estimated inner hot zone temperature of ca. 1500 C,  $N = 1 \times 10^{18}$  molecules/cm<sup>3</sup> (32 torr, Reference 6). Assuming an effective path length of 20 cm results in a calculated absorptance of:

$$\begin{aligned}\text{Abs} &= 1 - \exp[-(2 \times 10^{-19})(1 \times 10^{18})(20)] \\ &= 1 - 0.02 = 98\%.\end{aligned}$$

That is, roughly 98% of the incident light is absorbed; 2% of the incident light is transmitted. Again, this is only a rough calculation.

These initial SiO experiments in the carbon furnace demonstrated that the frequency doubling crystal and CCLAS system were behaving properly. However, an absolute calibration of SiO percent transmission (or absorption) versus temperature was not conducted. Large uncertainties exist in both the true temperature inside the carbon furnace and the effective path length. Uncertainty exists in the furnace temperature because the pyrometer could not view the inside surface of the heating element; instead, the pyrometer viewed



the outside surface of the heating element. Undoubtedly, these two temperatures could differ by more than one hundred degrees. Uncertainty exists in the effective pathlength due to temperature gradients and unknown equilibrium conditions in the furnace. Both problems could be minimized if the probe laser was steered through the transverse rather than the longitudinal path in the furnace. The transverse pathlength would sample only the region directly over the crucible in the center of the hot zone. In this operating configuration, the pathlength (approximately 3 cm) would be much better defined. Additionally, a better value of the single Q(18) rotational line absorption cross section is required to estimate the sensitivity of the method.

#### 4.2 PLUME DETECTION OF SiO FROM PURE SiO SAMPLES

A small chunk of SiO, taken directly from the supplier's bottle, was mounted in a sample holder by 3 alumina rods fitted with three 5 mil diameter tungsten wires (essentially eliminating conductive heat losses into the holders) and placed on the carousel wheel inside the vacuum chamber. The vacuum chamber was evacuated to 0.5 torr via a mechanical roughing pump. Approximately 41 watts HF chemical laser output heated the SiO sample; the beam was ca. 1.5 mm X 1 mm (radius). An IRCON two color optical pyrometer measured the front surface temperature; the viewing area of the optical pyrometer was approximately 3 mm<sup>2</sup> (i.e. a 2 mm diameter circular area). HF laser power was monitored via a calibrated beamsplitter. The frequency doubled light was steered approximately 1 mm in front of the sample front surface; transmitted frequency doubled light was detected by a UV sensitive photodiode. The experimental apparatus is shown in Figure 5.

A typical scan from the CCLAS system is shown in Figure 6; panel a is the HF power, panel b is the front surface temperature (in Kelvin) recorded by the two color pyrometer, panel c is the raw SiO signal plotted in percent transmission, and panel d is the signal from the tellurium reference cell. The SiO sample was heated to a temperature of ca. 1500 C and then the CCLAS system began the wavelength scan. The three absorption peaks in panel c are due to the Q(18), P(13), and R(26) rotational transitions of the A - X (0,0) band of SiO (see Figures 1 and 2 for computer simulated spectra). At 1500 C, the number density (N, molecules/cm<sup>3</sup>), is approximately  $1 \times 10^{18}$ . Assuming an effective pathlength of 0.8 cm (the SiO sample was approximately 6 mm long in the probing dimension and the probe beam was ca. 1mm in front of the sample surface), the calculated percent absorptance is

$$\text{Abs} = 1 - \exp[-(2 \times 10^{-18})(1 \times 10^{18})(0.8)] = 15\%$$

That is, 15 % of the incident probe beam is absorbed; 85% of the probe beam is transmitted. The calculated absorptance of 15% is a factor of 4 less than the experimental value; the following explanations could account for the discrepancy:



# SiO: FREQUENCY SCAN

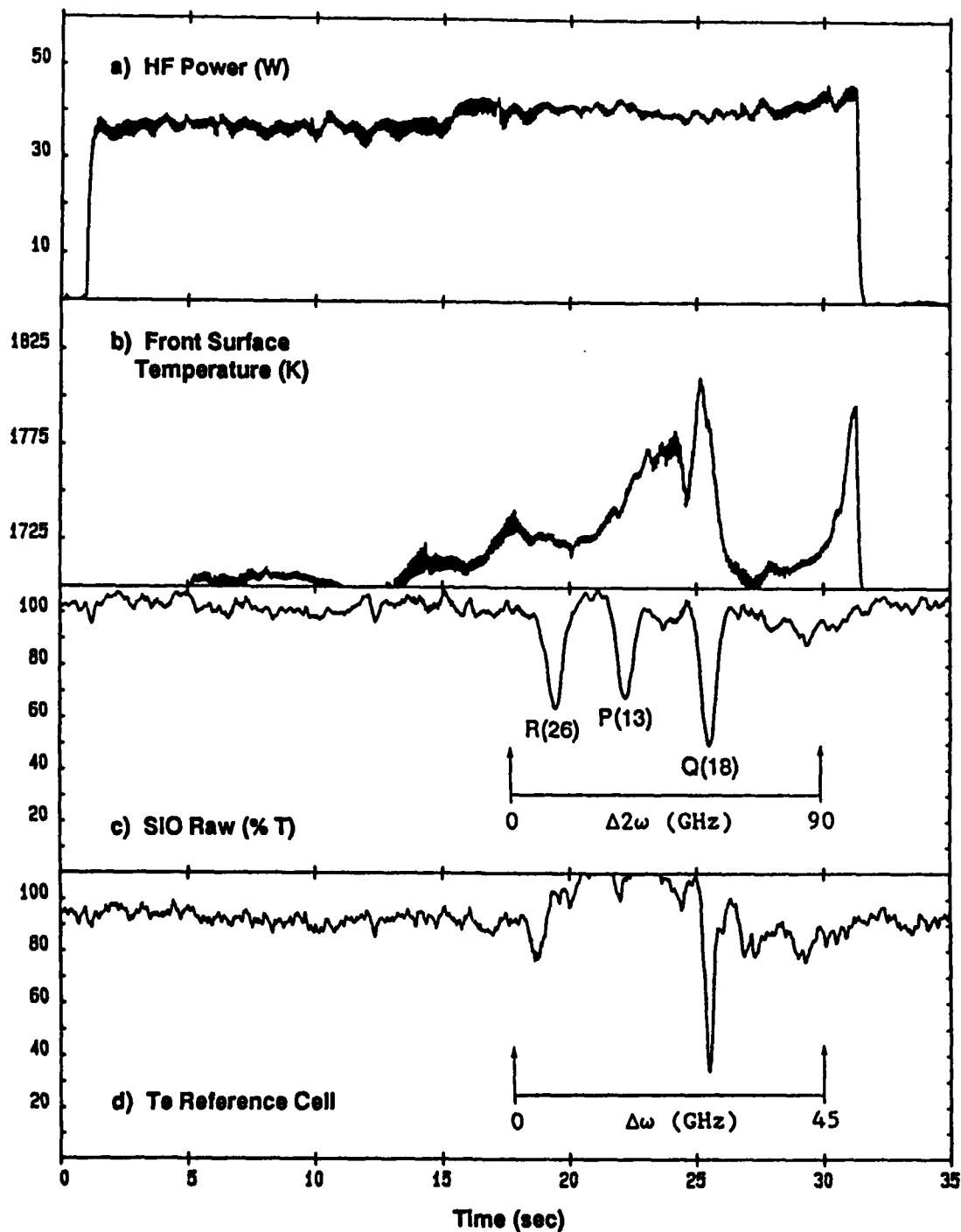


**Figure 6:** Data from "pure SiO" heated by ca. 40 W of HF chemical laser output. Panels a, b, c, and d show the HF laser power, front surface temperature, SiO transmission signal, and Te wavelength reference, respectively. The absorption peaks in panel c are due to the R(26), P(13), and Q(18) rotational transitions of the SiO A - X (0,0) band. Panel d shows a major Te absorption line used as a wavelength calibration for the dye laser. The arrows mark the time CCLAS was scanning frequency, probing for SiO during the heating experiment.

1) the effective pathlength could be longer than 0.8 cm; the sample chamber dimensions are orders of magnitude greater than the sample size, and a white film (presumably  $\text{SiO}_2$ ) was formed on portions of the sample chamber far away from the target,

2) the probe beam, due to convective currents in the gas, may not have sampled the highest density portion of the plume; the highest plume density may be offset vertically from target center at a probe distance 1 mm from the sample surface,

3) the absorption cross section could be incorrect (see section 4.1 above).

The first two theories could be tested by simply probing for SiO in different regions of the plume and vacuum chamber.

These initial laser heating/plume probing experiments on "pure SiO" show the experimental apparatus was behaving properly. Post test visual inspection of the SiO sample showed brilliant purple, blue, and green colors on the front surface of the test specimen. These are possibly due to interference patterns caused by a freshly deposited thin film (possibly  $\text{SiO}_2$  or other oxide) on the substrate surface. Also, white powder and glassy beads, presumably  $\text{SiO}_2$ , were observed on the front surface.

#### 4.3 PLUME DETECTION of SiO FROM MODEL SAMPLES

Samples were machined at HARC with a "diamond coated" cut off wheel. Individual specimens of uncoated samples measured approximately 3 mm X 3 mm X 1 mm (length X width X thickness,  $\pm$  20%). Individual specimens of coated samples (MS7 and MS8) had to be cut by hand and, therefore, were much less reproducible in final fabricated size. Samples were held in a well controlled environment of either a) vacuum (ca. 0.5 torr), b) 5 torr oxygen, or c) 200 torr oxygen, and were heated to a maximum temperature of approximately 1950 C by a normal incidence, 30 - 100 watt cw multiline HF chemical laser operating at ca. 2.7  $\mu$ . The experimental apparatus, unchanged from the pure SiO plume detection experiment, is shown in Figure 5.

##### 4.3.1 VACUUM , 5 TORR and 200 TORR OXYGEN EXPERIMENTS

Machined samples were individually weighed and mounted in holders equipped with 5 mil diameter tungsten wires. The holders were then mounted on the carousel wheel in the vacuum chamber; the vacuum chamber was purged with helium and evacuated. The sample, in vacuum (ca. 0.5 torr), was heated by the output of the HF chemical laser and the plume was probed for SiO by scanning CCLAS over a small wavelength interval; the dye laser scan took approximately 15 seconds. In some instances, visual observation of the sample during laser irradiation were made. The sample was weighed again, remounted in the holder, and the heating/probing experiment was repeated on the same specimen in a 5 torr oxygen atmosphere. The sample was weighed a final time in order to calculate mass loss/gain.

In the 200 torr oxygen experiments, the plume was probed for SiO by scanning the dye laser frequency (i.e. no temperature scan experiments were conducted). In all 200 torr oxygen experiments no SiO was detected; however, interesting observations were made during these experiments. The samples

were weighed, mounted in holders, heated to temperature in a 200 torr oxygen environment while probing for SiO, and weighed a final time. The experimental results are presented below according to sample type.

SiC (MS1):

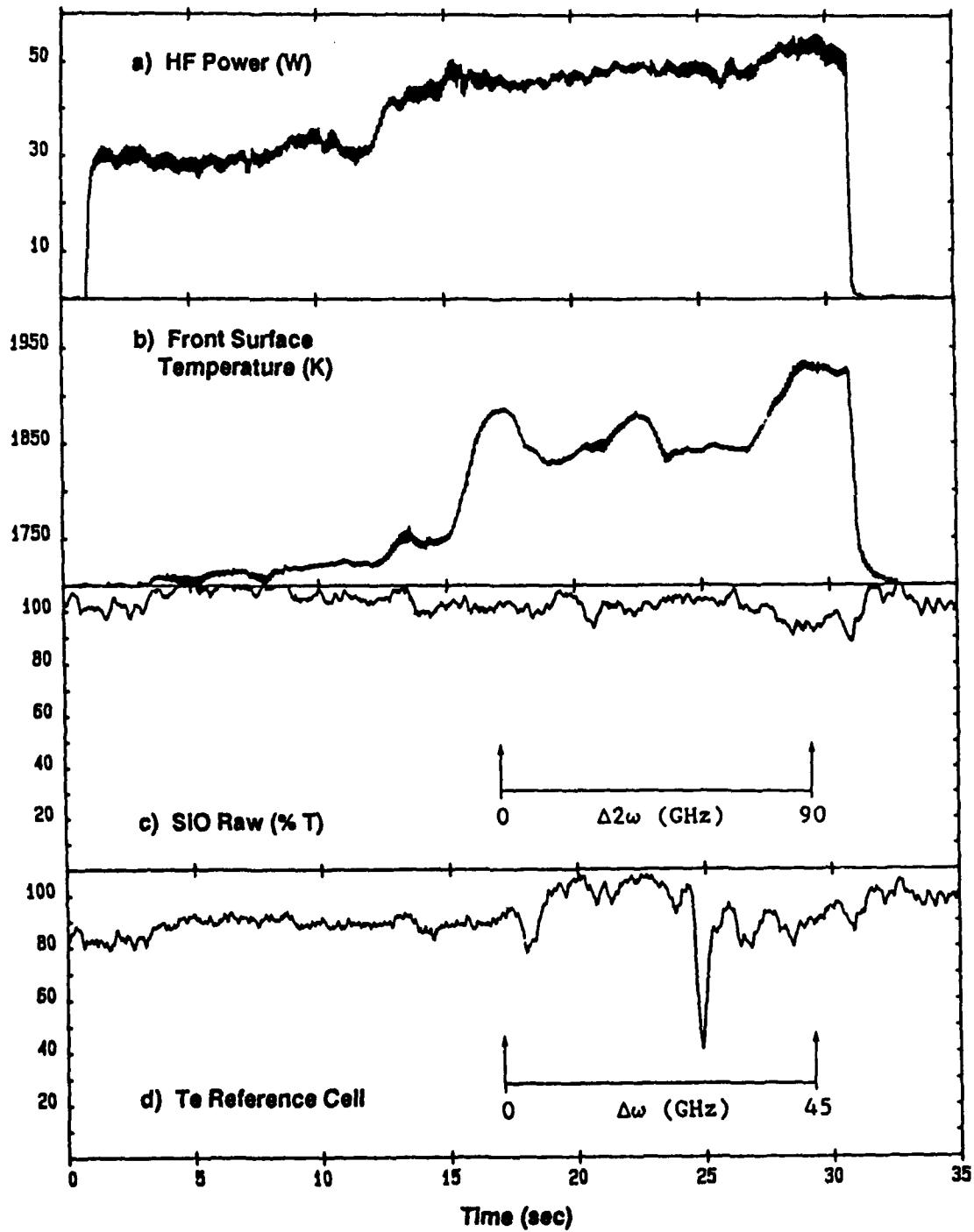
Figure 7 shows the data collected during the vacuum irradiation of MS1; no SiO absorption peaks were recorded. Figure 8 shows the data collected during the 5 torr oxygen experiment; SiO was easily detected as evidenced by the R(26), P(13), and Q(18) transitions. Visual observation of the sample under laser irradiation showed white hot "sparklers" being ejected from and normal to the front sample surface. Post test visual inspection of the oxygen/laser irradiation test specimen showed glassy beads had formed on the sample and on the alumina and tungsten sample supports. Also, white powder and glassy bubbles, presumably SiO<sub>2</sub>, were observed. The pre test sample mass, post vacuum/laser irradiation test mass, and post 5 torr oxygen/laser irradiation test mass were 21.177 mg, 20.884 mg, and 16.535 mg, respectively.

Figure 9 shows data collected during a temperature scan on a MS1 sample in 5 torr oxygen. In this experiment, the dye laser frequency was held fixed on the Q(18) SiO transition while the MS1 sample was heated. Visual observation of the sample during laser irradiation revealed white hot "sparklers" being ejected from and normal to the front sample surface; also, a blue, hemispherical shaped plume was observed. Post test visual inspection of the oxygen/laser irradiation test specimen showed an abundance of white powder and glassy beads/coating had formed on the sample front surface. The pre test and post test masses of this MS1 sample were 24.698 mg and 3.475 mg, respectively - a mass loss of 21.223 mg occurred during this experiment.

Figure 10 shows the data collected on a MS1 sample held in a 200 torr oxygen environment; no evidence of any SiO signal was detected from the dye laser wavelength scan. Post test visual inspection of the sample showed small, dark "mounds" had formed on the front surface of the sample, and a small bead of material had formed on the sample edge. No white powder was formed on the sample supports. The MS1 pre test and post test masses were 23.211 and 23.233 mg, respectively - a weight gain of 0.022 mg occurred as a result of the experiment.

A second MS1 sample was taken to a higher temperature in a 200 torr

# MS1: VACUUM: FREQUENCY SCAN



**Figure 7:** Data collected for a vacuum environment, laser irradiation of MS1. The arrows in panels c and d mark the time CCLAS was scanning frequency, probing for SiO during the heating experiment. From the data shown in panel c, no SiO was detected.



# MS1: 5 TORR OXYGEN: FREQUENCY SCAN

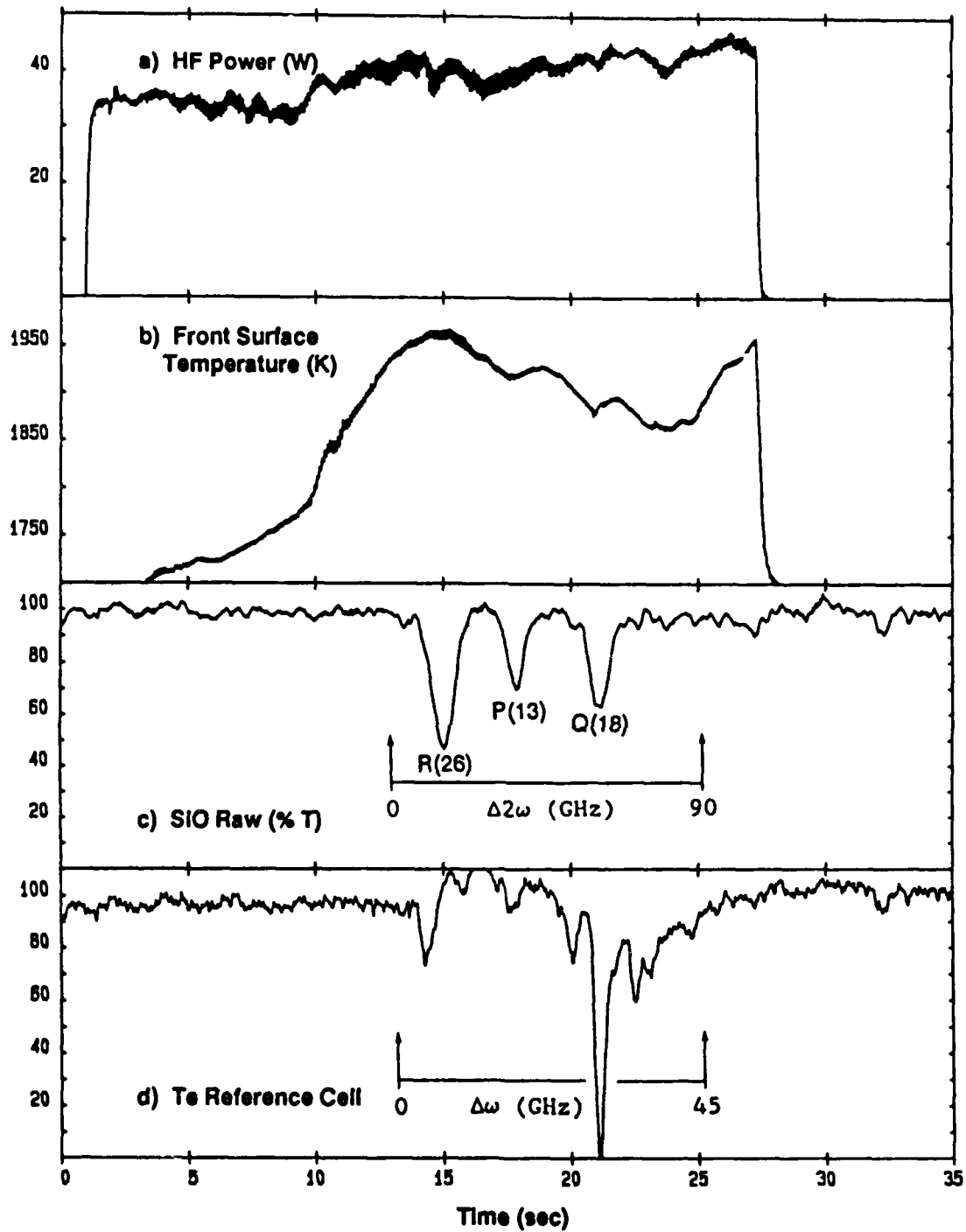


**Figure 8:** Data collected for a 5 torr oxygen environment, laser irradiation of MS1. As evidenced by the R(26), P(13), and Q(18) absorption peaks in panel c, SiO was detected. Note that the sample temperature was higher when the R(26) SiO transition was scanned compared to the sample temperature when the Q(18) SiO transition was scanned; this temperature difference accounts for the anomalous line intensities.

### MS1: 5 TORR OXYGEN: TEMPERATURE SCAN

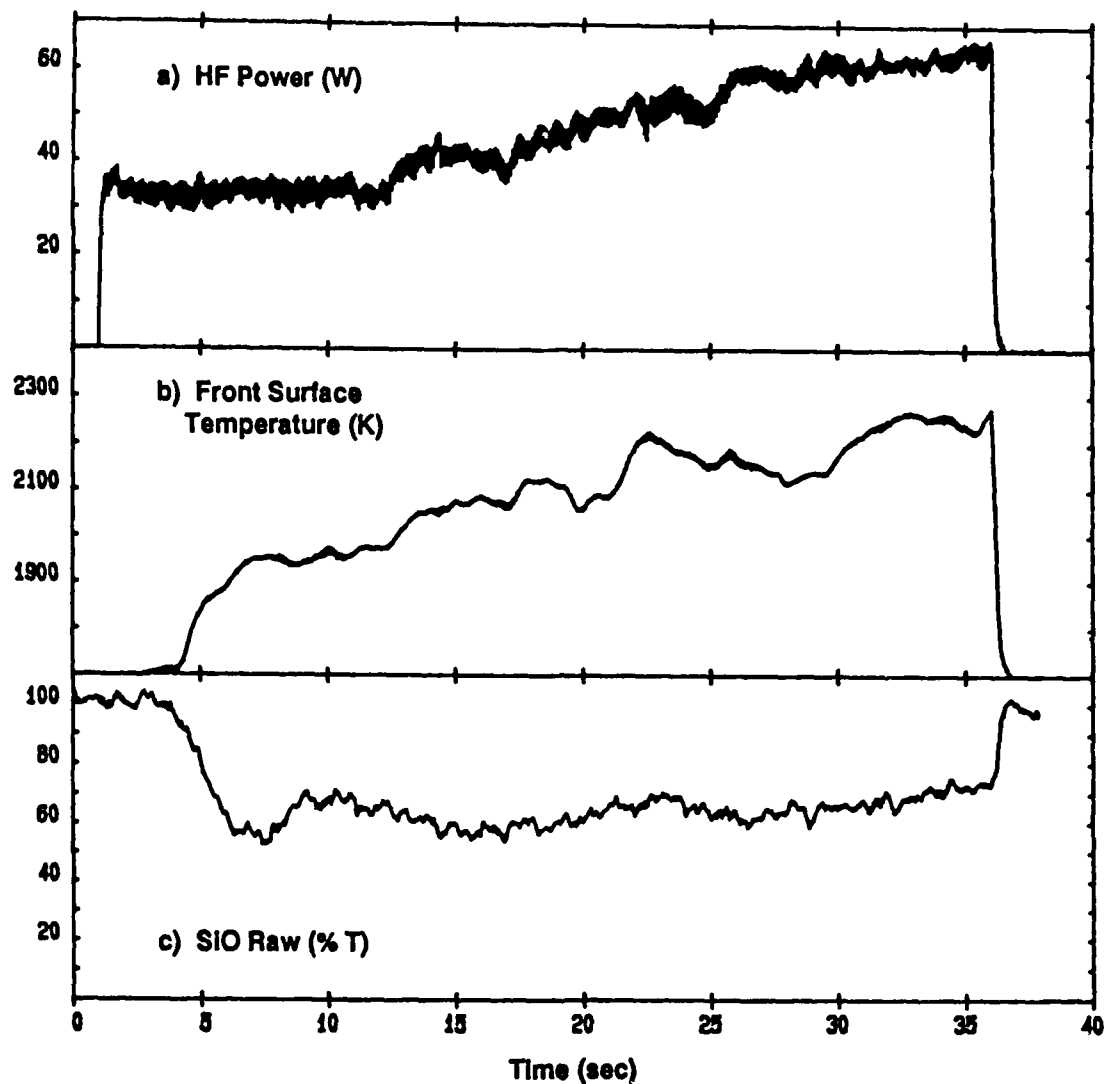


**Figure 9:** Data collected for a 5 torr oxygen environment, laser irradiation of MS1. The temperature of the sample was increased by manually increasing the HF laser power. The dye laser frequency was held stationary at the SiO Q(18) transition. Panel c shows the probe beam attenuation due to SiO.

# MS1: 200 TORR OXYGEN: FREQUENCY SCAN

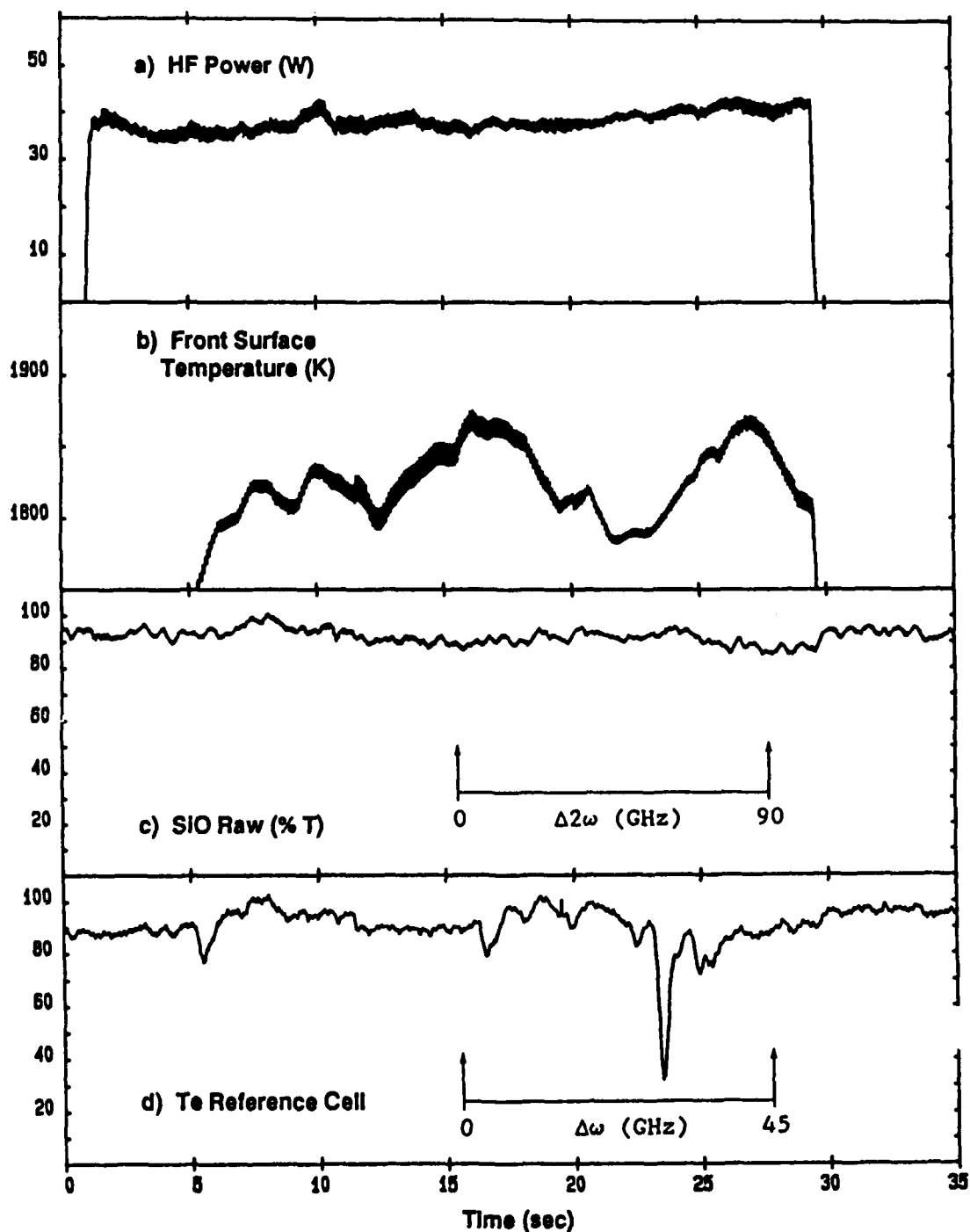


**Figure 10:** Data collected for a 200 torr oxygen environment, laser irradiation of MS1. The arrows in panels c and d mark the time CCLAS was scanning frequency, probing for SIO during the heating experiment. From the data in panel c, no SIO was detected.

oxygen environment with different results than reported above. Figure 11 again shows no evidence of SiO, but at approximately 2030 K the probe beam is strongly attenuated. Indeed, visual observation of the sample chamber at this time proved interesting. The sample chamber became increasingly luminous, the temperature rose quickly, and then the sample chamber "flashed" with bright light. Possibly, at this higher temperature, CO pressure built up at an internal interface which resulted in a explosion near the surface ejecting sample particles which strongly attenuated the probe beam. Visual inspection of the post test specimen showed several small glassy beads had formed on the sample surface. Also, the alumina and tungsten sample supports were heavily coated with white powder. Pre and post test sample mass was 21.881 mg and 8.940 mg, respectively - a mass loss of 12.941 mg occurred during this experiment.

# MS1: 200 TORR OXYGEN: FREQUENCY SCAN

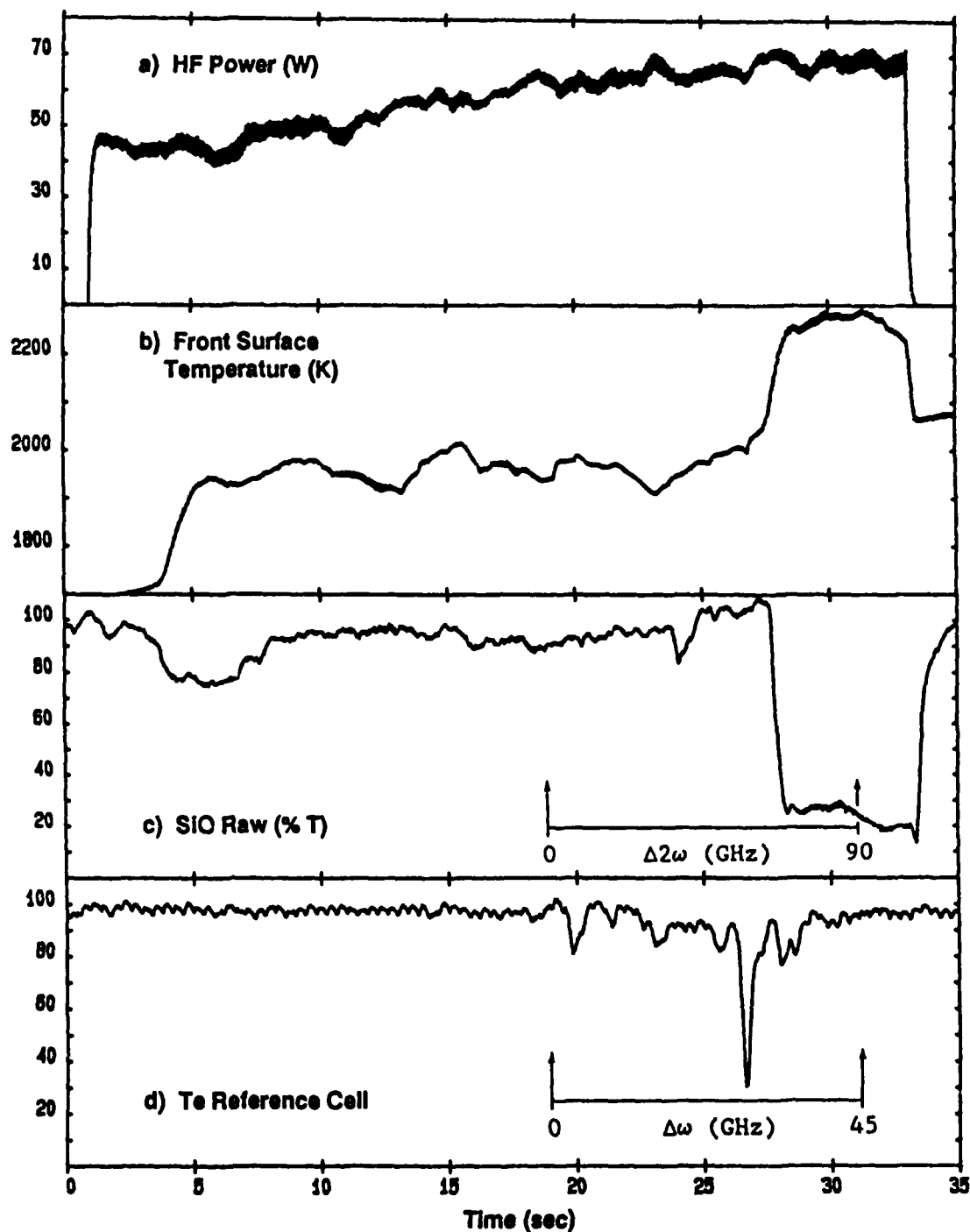


**Figure 11:** Data collected for a 200 torr oxygen environment, laser irradiation of MS1. The arrows in panels c and d mark the time CGLAS was scanning frequency, probing for SiO during the heating experiment. SiO was not detected; however, the probe beam was obviously attenuated. See text for discussion.

Si<sub>3</sub>N<sub>4</sub> (MS2):

Figure 12 shows data collected for the vacuum irradiation of MS2; no SiO was detected. Figure 13 shows the data collected during the heating experiment with 5 torr oxygen in the vacuum chamber; no SiO was detected probably due to the low substrate temperature. Visual inspection of the the post oxygen/laser irradiation test sample showed moderate front surface modification. This MS2 sample's pre test mass, post vacuum/laser irradiation test mass, and post 5 torr oxygen/laser irradiation test mass were 27.473 mg, 27.012 mg, and 26.760, respectively.

Another MS2 specimen was taken to higher temperature in a 5 torr oxygen environment; the data are shown in Figure 14. At this higher temperature, the three distinctive SiO absorption peaks are easily identified. Post test inspection of the sample showed white beads had formed on the front surface edges. This MS2 sample's pre test mass and post 5 torr oxygen/laser irradiation test mass were 35.621 mg and 24.193 mg, respectively - a mass loss of 11.428 mg occurred during this experiment.

Figure 15 shows data collected during a temperature scan; 5 torr oxygen was in the vacuum chamber. Visual observation of the sample under laser irradiation revealed very few white hot "sparklers" being ejected from and normal to the front sample surface; also, a blue, hemispherical shaped plume was observed. Visual post test inspection of the sample showed white beads had formed near the edges, and a white powder coated the sample supports. Also, the bottom portion of the sample had been totally "eaten" away. This MS2 sample's pre test and post test masses were 29.463 mg and 15.193 mg, respectively - a mass loss of 14.270 mg occurred during this experiment.

The temperature scan test was repeated for another MS2 sample; Figure 16 shows a similar temperature scan under the 5 torr oxygen environment. A blue, hemispherical shaped plume was observed which became brighter as the sample temperature was raised. Post test inspection of the sample showed white beads had again formed near the edges, and the same general portion of the sample had been "eaten" away. This MS2 sample's pre test and post test masses were 32.200 mg and 13.743 mg - a mass loss of 18.457 mg occurred during this experiment.

As evidenced by both post test visual inspections of the 5 torr oxygen/temperature scan specimens, an abundance of white powder and white beads had been formed in both the temperature scan experiments. Furthermore, in both temperature scan experiments, the sample was irradiated "on center" yet essentially the same portion of each sample was "eaten" away. One possible explanation for this reactive zone could be local heat convection in the sample and surrounding gas.

Figure 17 shows data collected on a MS2 sample held in a 200 torr oxygen environment; no SiO was detected. Post test visual inspection of this MS2 sample showed, similar to the first MS1 200 torr oxygen experiment, "mound" formation on the front surface of the sample. However, on this MS2 sample, the mounds were much more massive and glassy in appearance. No white powder coating was formed on the sample supports. Pre and post test sample masses were 27.735 mg and 27.856 mg, respectively - a weight gain of 0.121 mg occurred during the experiment.

# MS2: VACUUM: FREQUENCY SCAN

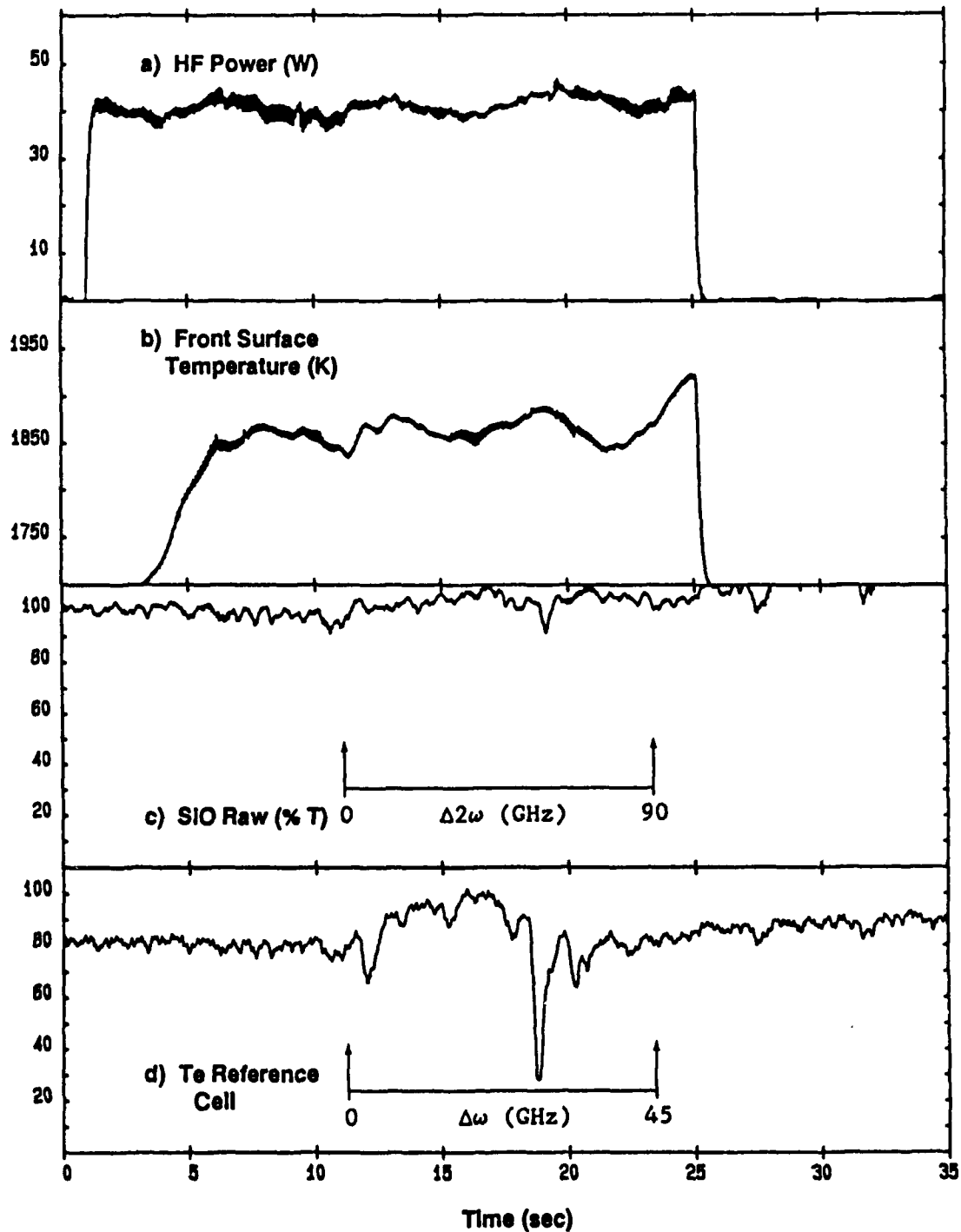


**Figure 12:** Data collected for a vacuum environment, laser irradiation of MS2. The arrows in panels c and d mark the time CCLAS was scanning frequency, probing for SiO during the heating experiment. Panel c shows no probe beam attenuation due to SiO.



# MS2: 5 TORR OXYGEN: FREQUENCY SCAN

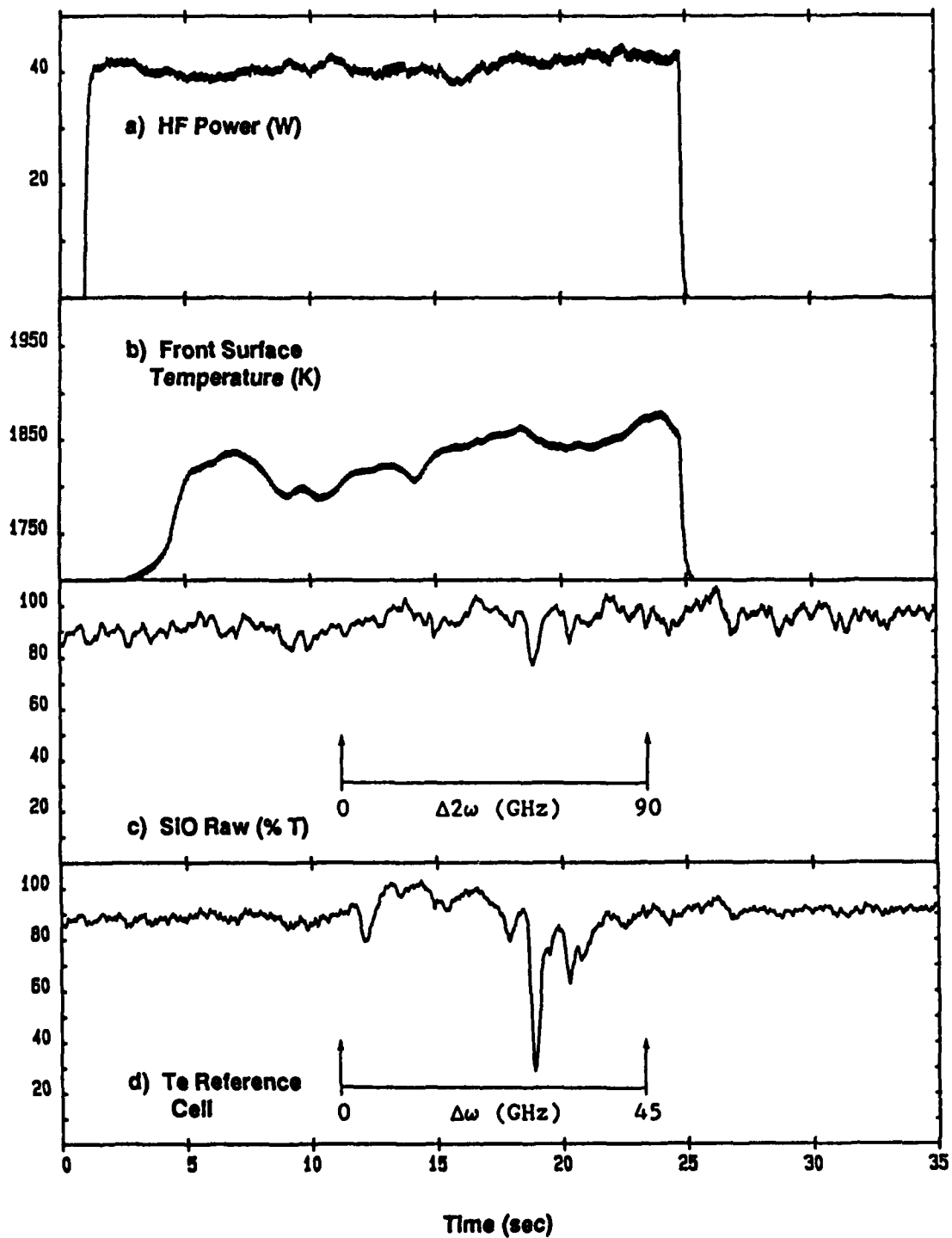


**Figure 13:** Data collected for a 5 torr oxygen environment, laser irradiation of MS2. The arrows in panels c and d mark the time CCLAS was scanning frequency, probing for SiO during the heating experiment. No SiO was detected, probably due to the low substrate temperature.

# MS2: 5 TORR OXYGEN: FREQUENCY SCAN

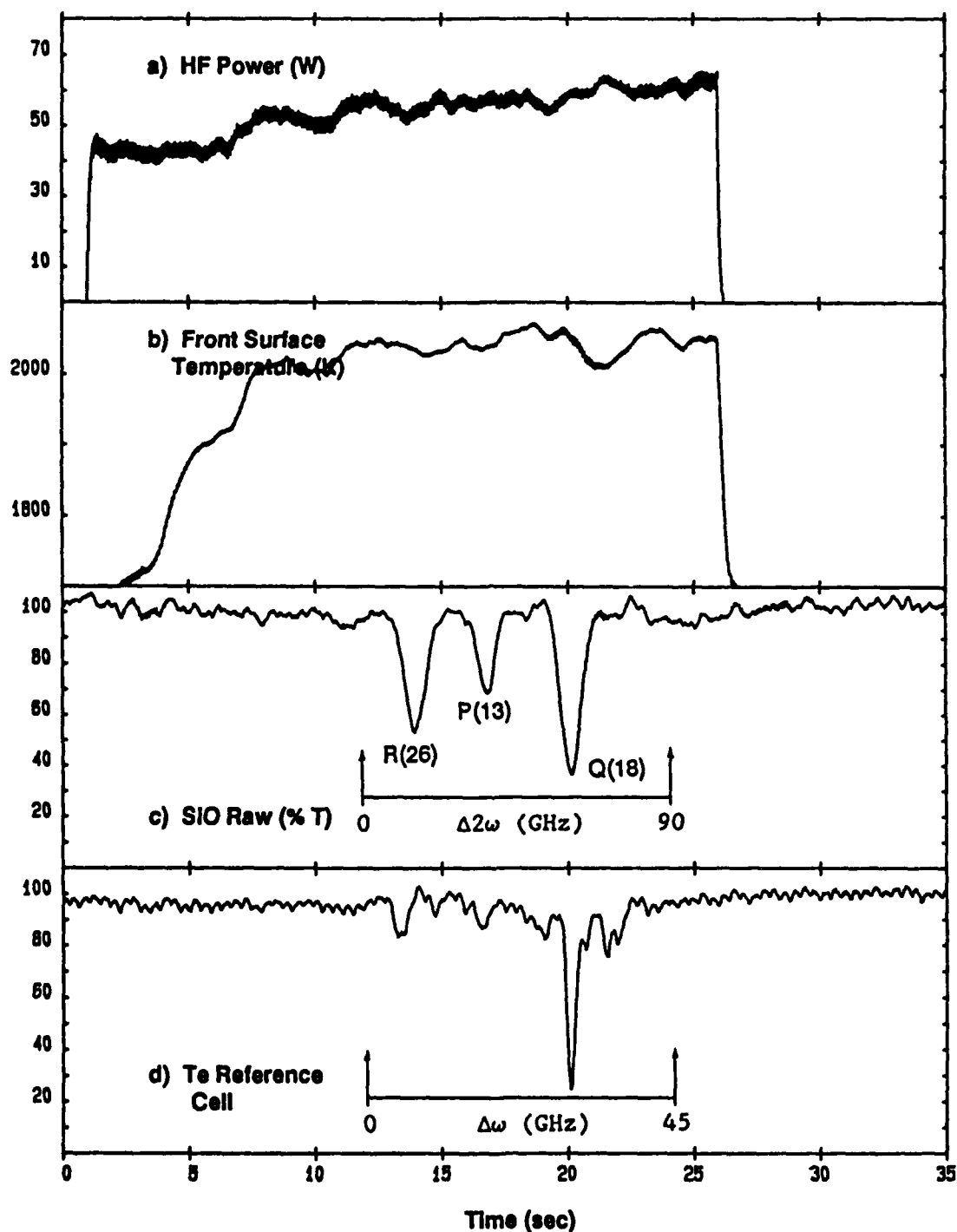


**Figure 14:** Data collected for a 5 torr oxygen environment, laser irradiation of MS2. The arrows in panels c and d mark the time CCLAS was scanning frequency, probing for SiO during the heating experiment. As evidenced by the three rotational transitions in panel c, SiO was detected.

### MS2: 5 TORR OXYGEN: TEMPERATURE SCAN

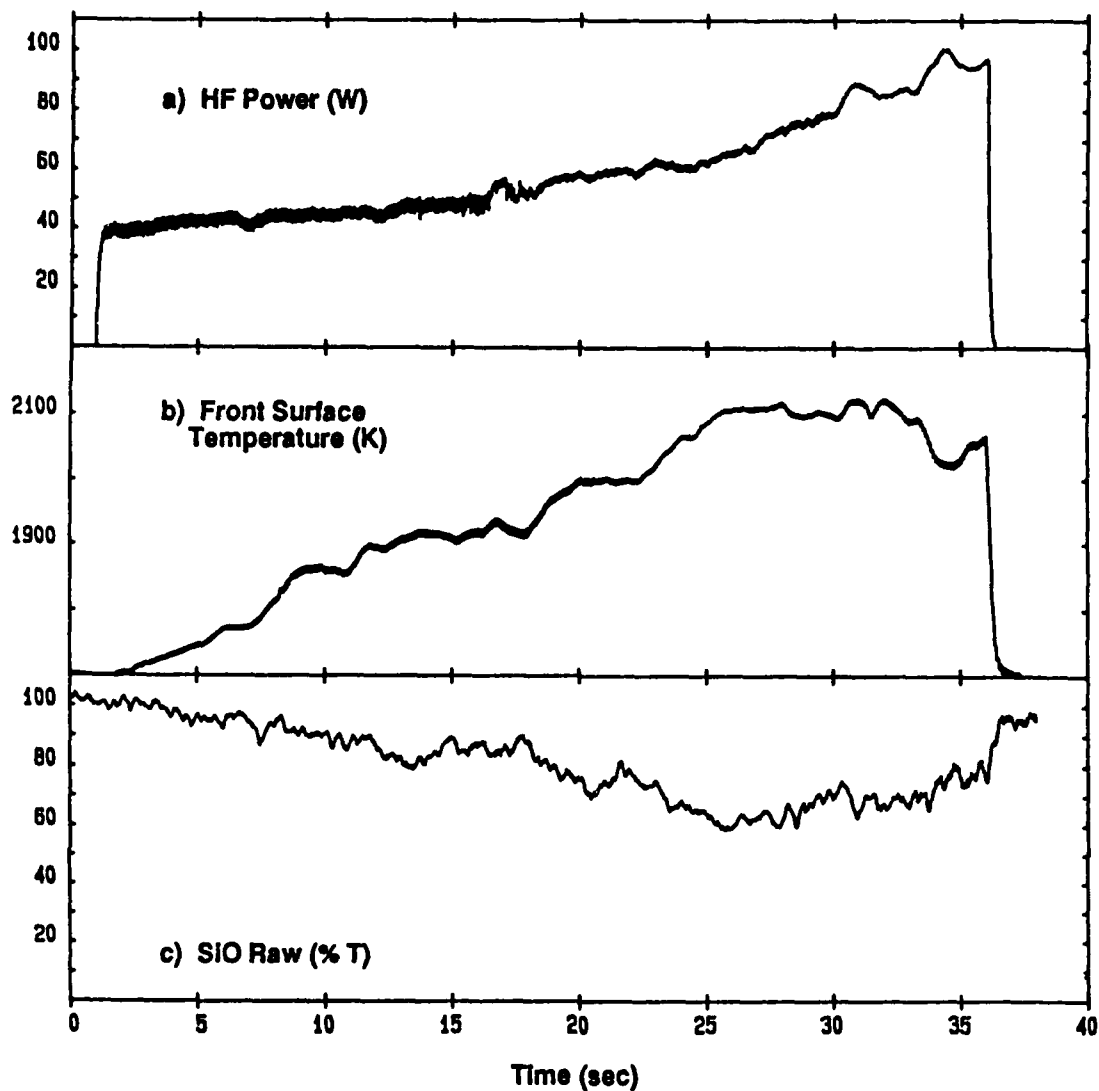


**Figure 15:** Data collected for a 5 torr oxygen environment, laser irradiation of MS2. The temperature of the sample was increased by manually increasing the HF laser power. The dye laser frequency was held stationary at the Q(18) SiO A - X (0,0) transition. Panel c shows the probe beam attenuation due to SiO.

### MS2: 5 TORR OXYGEN: TEMPERATURE SCAN

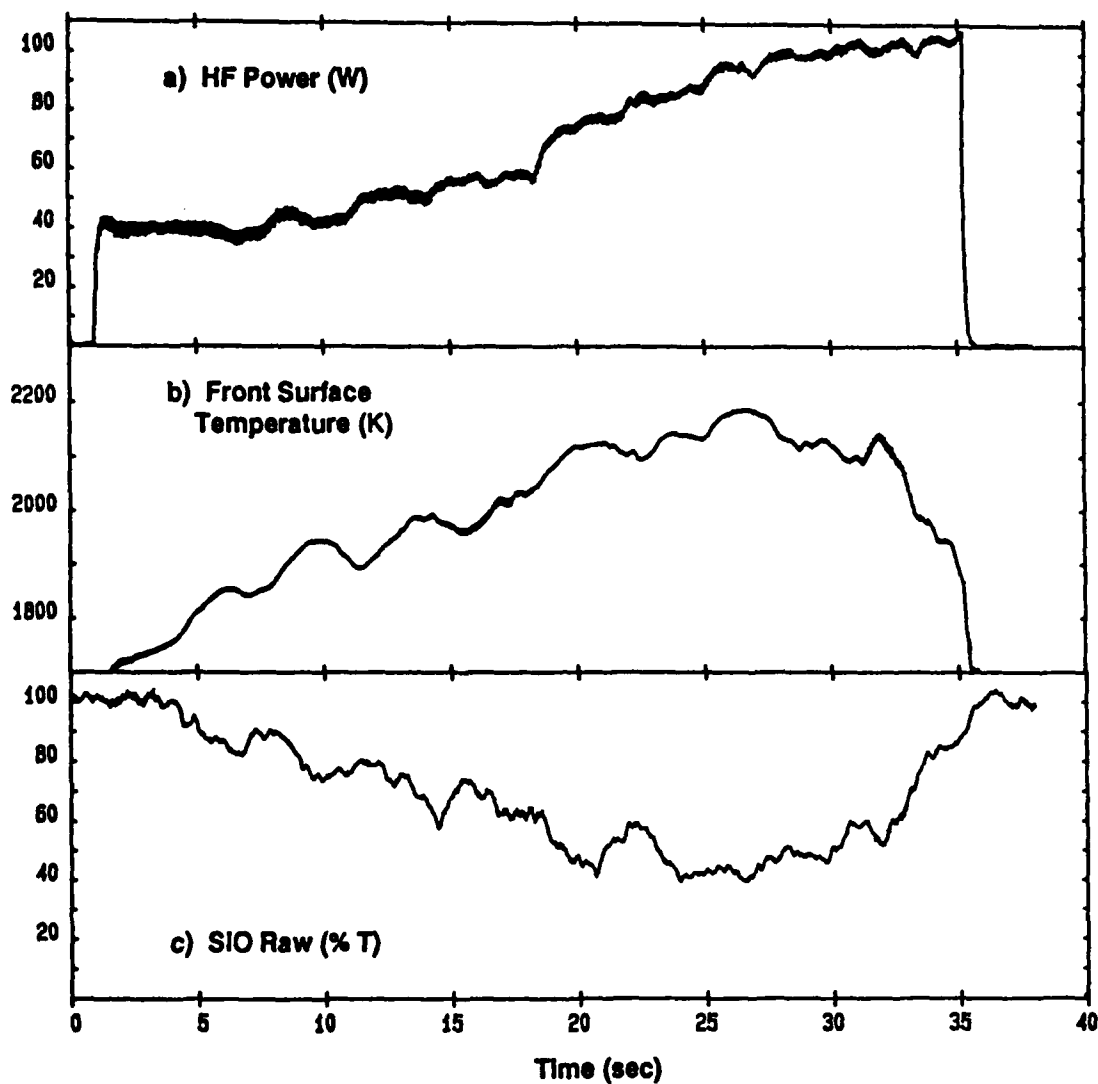


**Figure 16:** Data collected for a 5 torr oxygen environment, laser irradiation of MS2. The temperature of the sample was increased by manually increasing the HF laser power. The dye laser frequency was held stationary at the SiO Q(18) A - X (0,0) transition. Panel c shows the probe beam attenuation due to SiO.

# MS2: 200 TORR OXYGEN: FREQUENCY SCAN

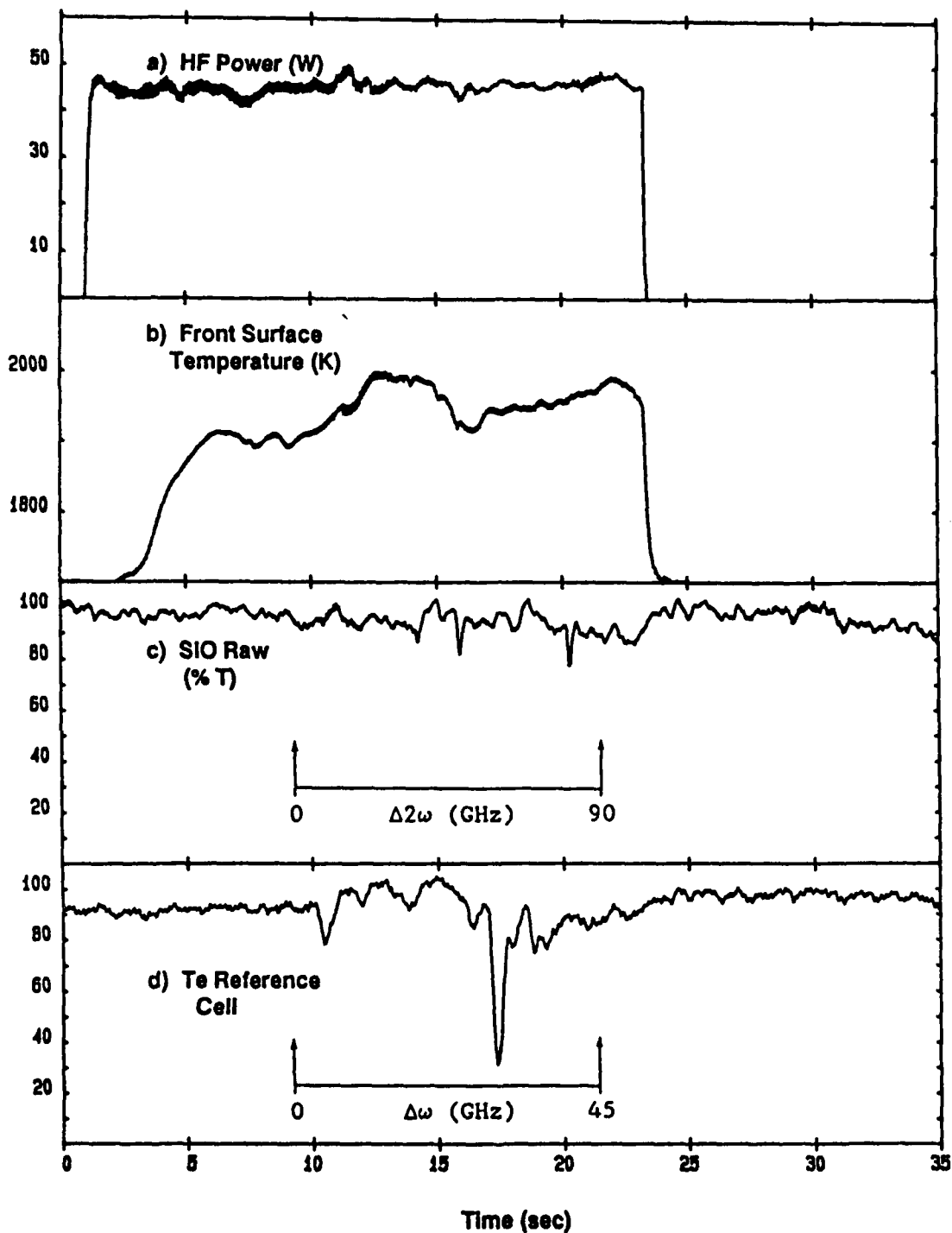


**Figure 17:** Data collected for a 200 torr oxygen environment, laser irradiation of MS2. The arrows in panels c and d mark the time CCLAS was scanning frequency, probing for SiO during the heating experiment. From the data in panel c, no SiO was detected.

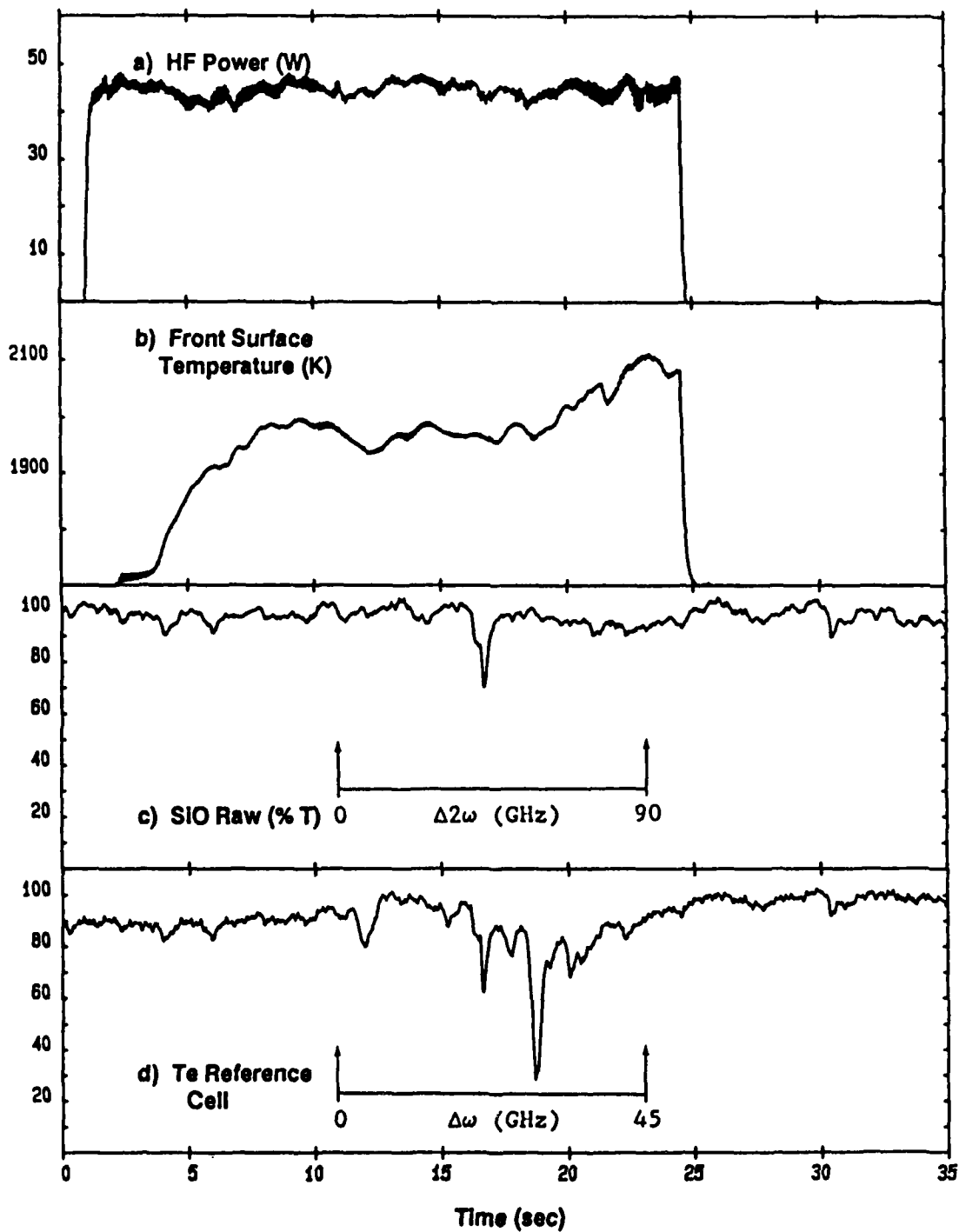
### SiC/SiC COMPOSITE (MS3):

Figure 18 shows data collected during the vacuum irradiation of MS3. No SiO was detected, but probe beam attenuation occurred for approximately 1 second during the experiment. Figure 19 shows data collected during the heating experiment with 5 torr oxygen in the chamber; SiO was detected. Visual inspection of the post oxygen/laser irradiation test specimen showed formation of a small amount of glassy beads on the substrate and supports as well as a glassy coating on the alumina holder. This MS3 specimen's pre test, post vacuum/laser irradiation test, and post 5 torr oxygen/laser irradiation test sample masses were 41.507 mg, 40.748 mg, and 38.755 mg, respectively.

Figure 20 shows data collected during a temperature scan of a MS3 sample; 5 torr of oxygen was in the test chamber. Visual observation of the sample under laser irradiation revealed an orange tinted plume at low temperature and a blue plume at high temperature. Visual observation of the post test specimen showed evidence of white glassy film and bead formation on the sample surface. Additionally, a shiny, blue tinted, white coating had been deposited on the the alumina sample supports. The MS3 sample pre and post test masses were 40.940 mg and 34.453 mg, respectively a mass loss of 6.487 mg occurred during this experiment.

Figure 21 shows data collected on a MS3 sample held in a 200 torr oxygen environment; no SiO was detected, but beam attenuation obviously occurred during the experiment; the observed beam attenuation is unexplained at this time. Visual observation of the post test specimen showed glassy "bubble" formation on the sample front surface. Pre and post test sample masses were 41.330 mg and 39.373 mg, respectively - a mass loss of 1.957 mg occurred during the experiment.

### MS3: VACUUM: FREQUENCY SCAN



**Figure 18:** Data collected for a vacuum environment, laser irradiation of MS3. The arrows in panels c and d mark the time CCLAS was scanning frequency, probing for SiO during the heating experiment. Panel c shows no probe beam attenuation due to SiO, but attenuation may be from particles ejected from the substrate. See text for discussion.

# MS3: 5 TORR OXYGEN: FREQUENCY SCAN

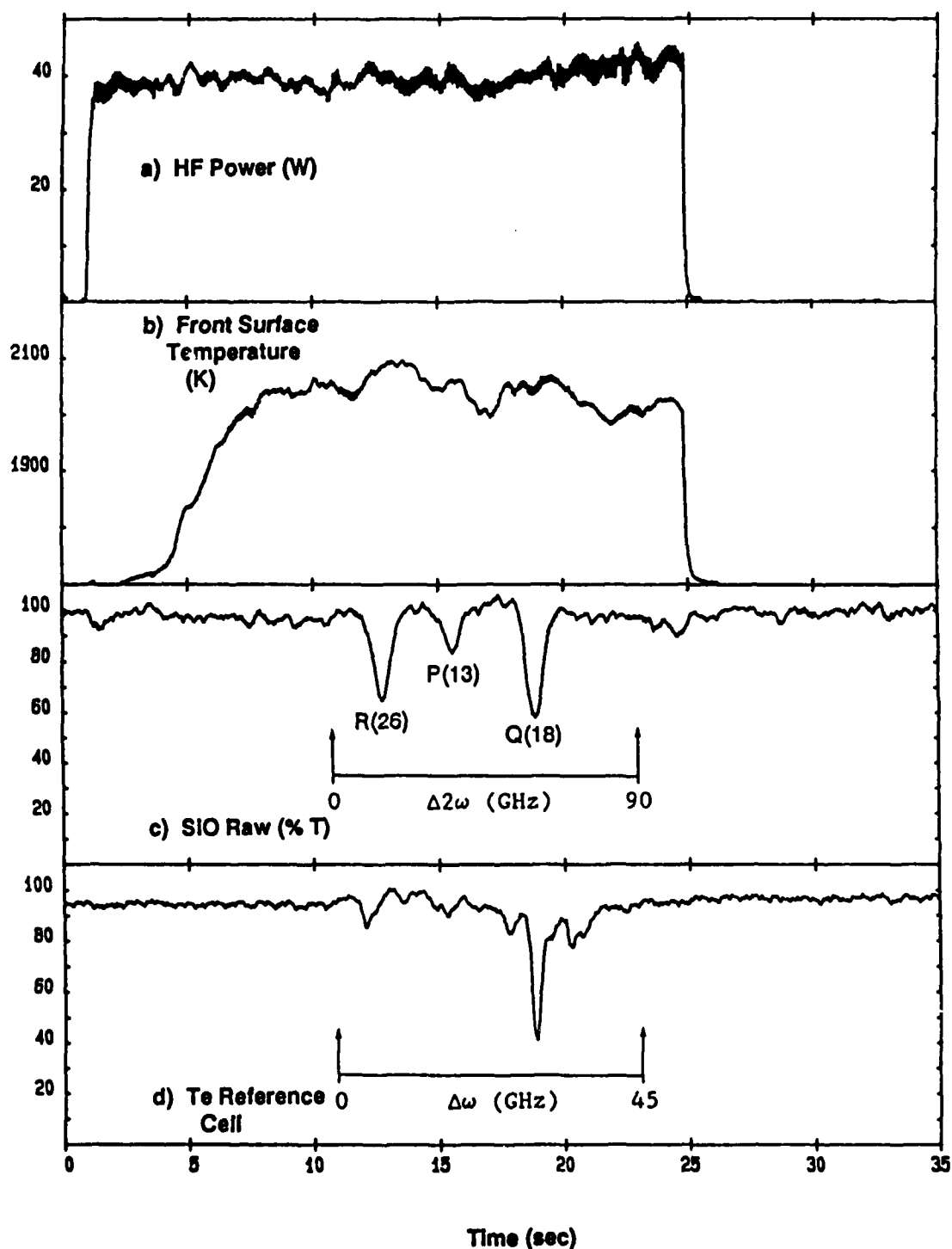


**Figure 19:** Data collected for a 5 torr oxygen environment, laser irradiation of MS3. The arrows in panels c and d mark the time CCLAS was scanning frequency, probing for SiO during the heating experiments. As evidenced by the three rotational transitions in panel c, SiO was detected.



### MS3: 5 TORR OXYGEN: TEMPERATURE SCAN

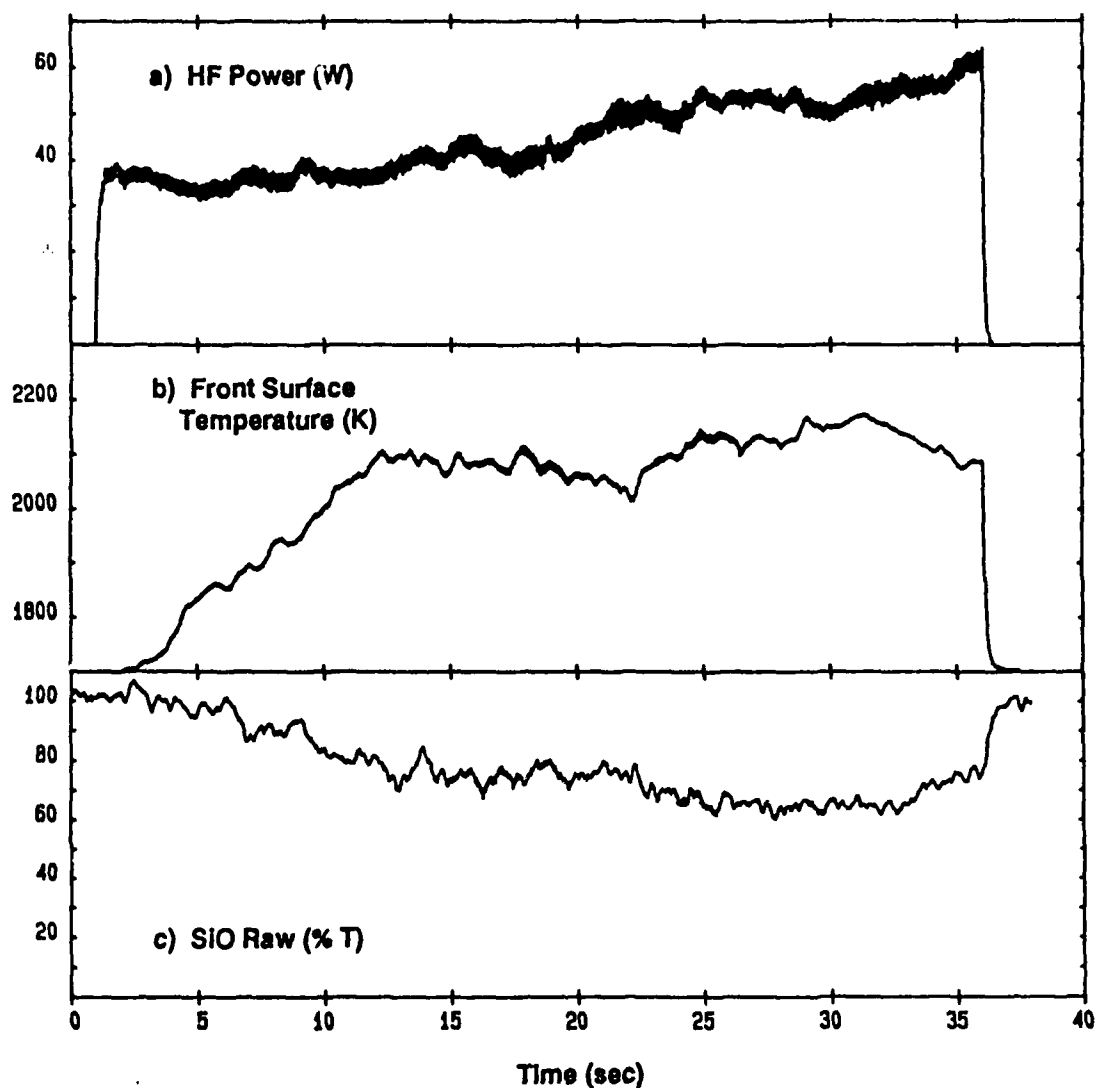


**Figure 20:** Data collected for a 5 torr oxygen environment, laser irradiation of MS3. The temperature of the sample was increased by manually increasing the HF laser power. The dye laser frequency was held stationary at the Q(18) SiO A - X (0,0) rotational transition. Panel c shows the probe beam attenuation due to SiO.

### MS3: 200 TORR OXYGEN: FREQUENCY SCAN

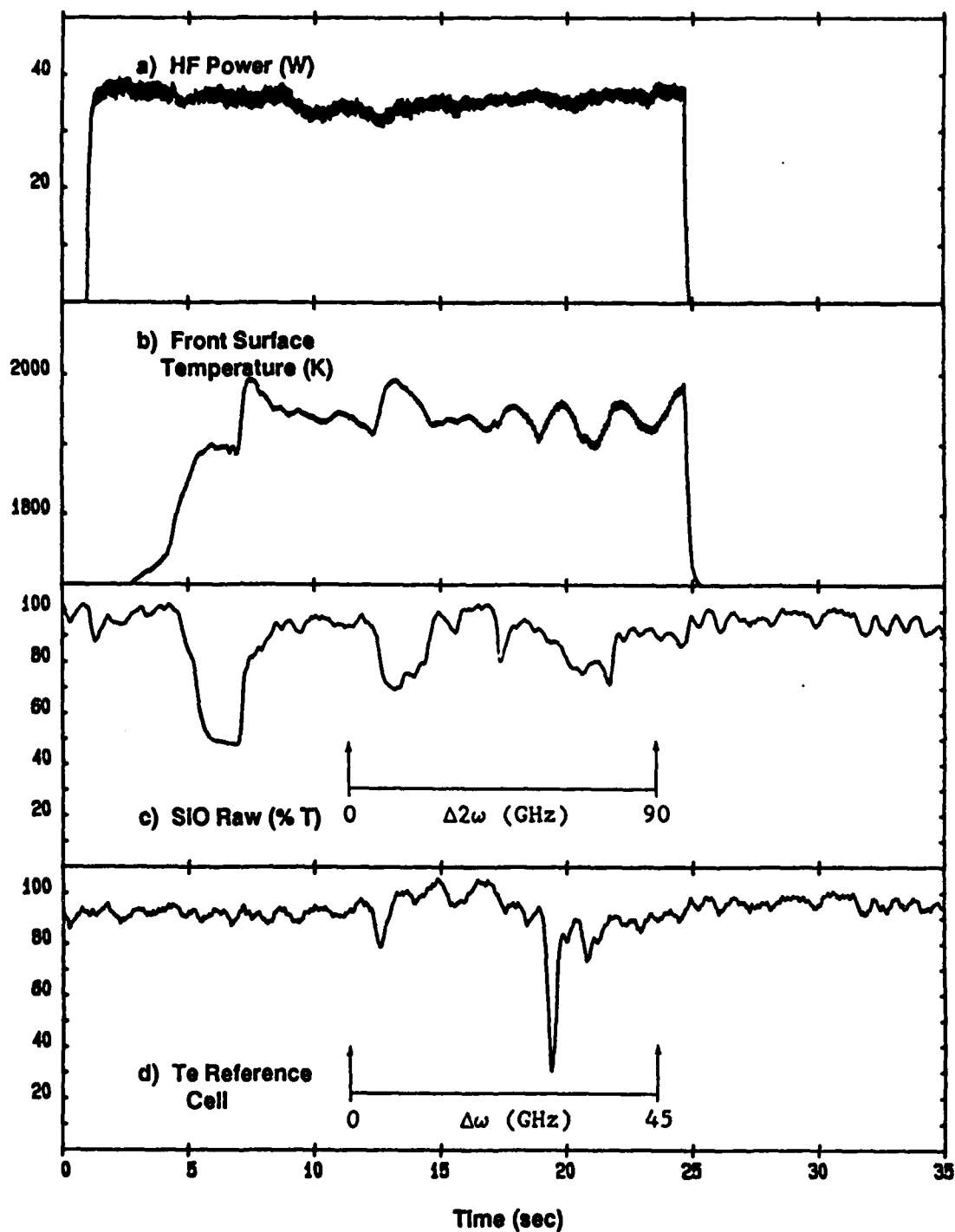


**Figure 21:** Data collected for a 200 torr oxygen environment, laser irradiation of MS3. The arrows in panels c and d mark the time CCLAS was scanning frequency, probing for SiO during the heating experiment. From the data in panel c, SiO was not detected, but the probe beam was obviously attenuated during the experiment.

BORON-INHIBITED MATRIX C/C COMPOSITE with CVD COATED SiC (MS7):

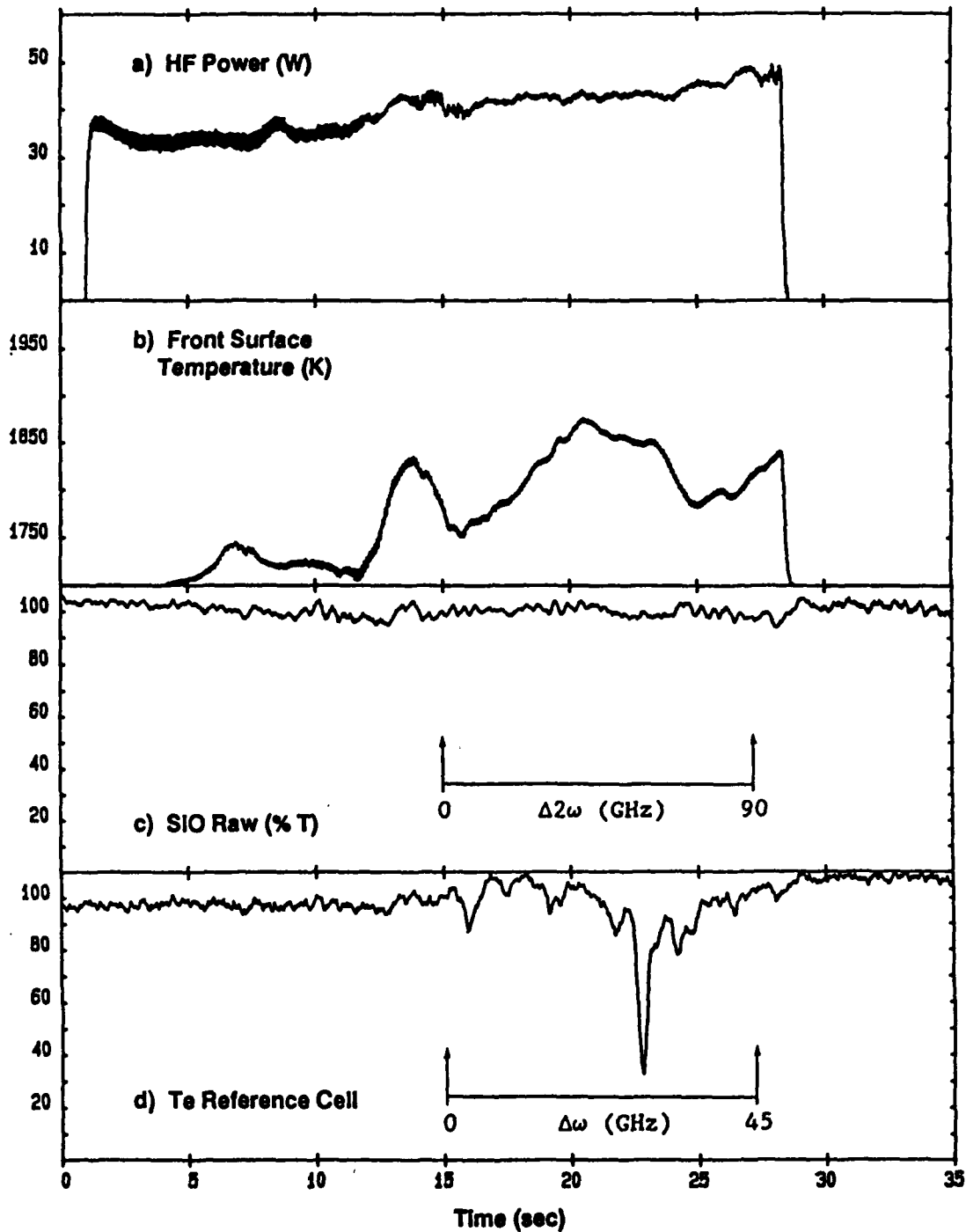
Figure 22 shows data collected during the vacuum irradiation of MS7: no SiO was detected. Figure 23 shows data collected during the heating experiment with 5 torr oxygen in the chamber; SiO was detected. Visual observation of the sample under laser irradiation revealed white hot "sparklers" being ejected from and normal to the front sample surface; also, a blue, hemispherical shaped plume was observed. Visual inspection of the post oxygen/laser irradiation test specimen showed evidence of glassy film and bead formation on the perimeter of the sample surface; also, only a partial coating of SiC appeared to remain on the substrate. The coating on the alumina sample supports appeared, as above, as a bluish white film. This MS7 specimen's pre test, post vacuum/laser irradiation, and post 5 torr oxygen/laser irradiation sample masses were 27.872 mg, 26.742 mg, and 20.896 mg, respectively.

Figure 24 shows data collected during a temperature scan of a MS7 sample; 5 torr of oxygen was in the test chamber. Visual observation of the sample under laser irradiation revealed several white hot "sparklers" being ejected from and normal to the front sample surface; also, a blue, hemispherical shaped plume was observed at low temperature (near the start of the heating experiment), and a green plume was observed at high temperature (near the end of the heating experiment). Visual inspection of the post oxygen/laser irradiation test specimen showed that the entire SiC coating had been eaten away, and a substantial amount of white powder or film remained on the sample surface. The alumina supports are coated with a bluish white film and small black fibers. The MS7 pre test and post test masses were 26.971 mg and 16.939 mg, respectively - a mass loss of 10.032 mg occurred during this experiment.

Figure 25 shows data collected on a MS7 sample held in a 200 torr oxygen environment; no SiO was detected, and no beam attenuation was observed. Visual inspection of the post test specimen showed a bluish white coating had been deposited vertically from the center of the holder - probably a result of heat convection in the gas around the sample. Also, several "bubbles" ca.

0.3 mm diameter and gold colored deposits were observed on the sample front surface. Pre and post test sample masses were 28.661 mg and 24.112 mg, respectively - a mass loss of 4.549 mg occurred during the experimnt.

# MS7: VACUUM: FREQUENCY SCAN



**Figure 22:** Data collected for a vacuum environment, laser irradiation of MS7. The arrows in panels c and d mark the time CCLAS was scanning frequency, probing for SiO during the heating experiment. Panel c shows no probe beam attenuation due to SiO.

# MS7: 5 TORR OXYGEN: FREQUENCY SCAN

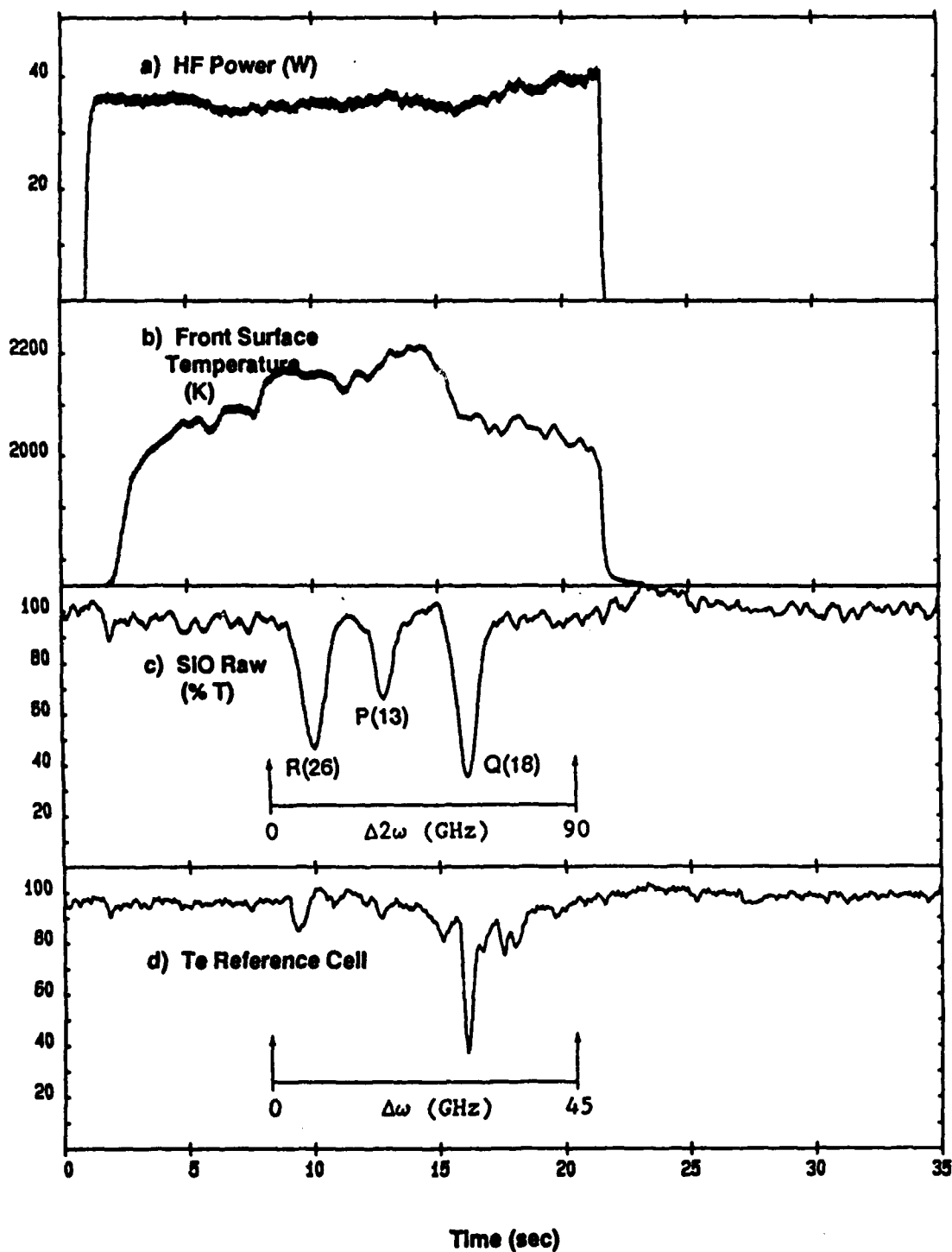


**Figure 23:** Data collected for a 5 torr oxygen environment, laser irradiation of MS7. The arrows in panels c and d mark the time CCLAS was scanning frequency, probing for SiO during the heating experiment. As evidenced by the three rotational absorption lines in panel c, SiO was detected.

### MS7: 5 TORR OXYGEN: TEMPERATURE SCAN

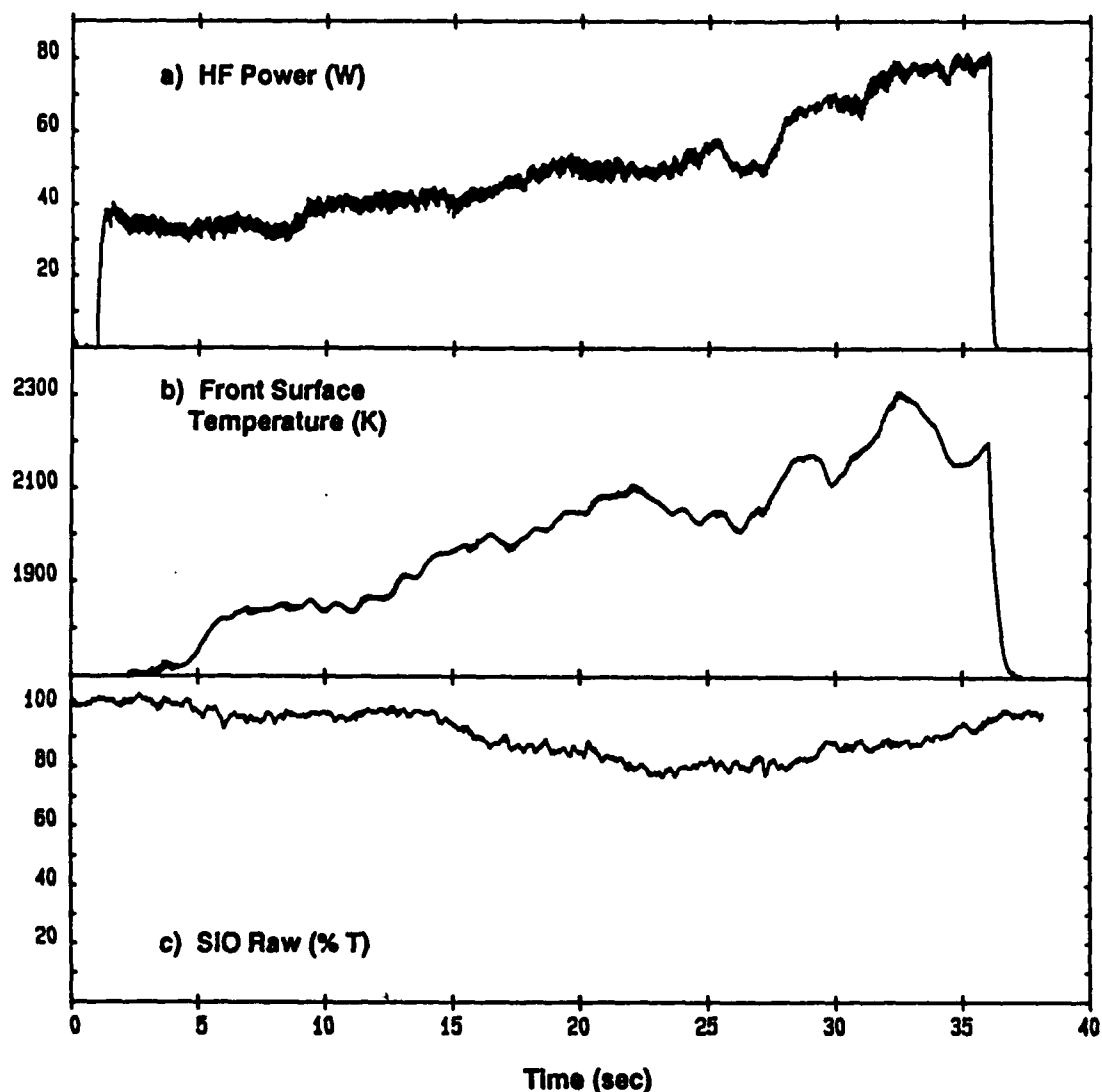


**Figure 24:** Data collected for a 5 torr oxygen environment, laser irradiation of MS7. The temperature of the sample was increased by manually increasing the HF laser power. The dye laser frequency was held stationary at the Q(18) SiO A - X (0,0) transition. Panel c shows the probe beam attenuation due to SiO.

# MS7: 200 TORR OXYGEN: FREQUENCY SCAN

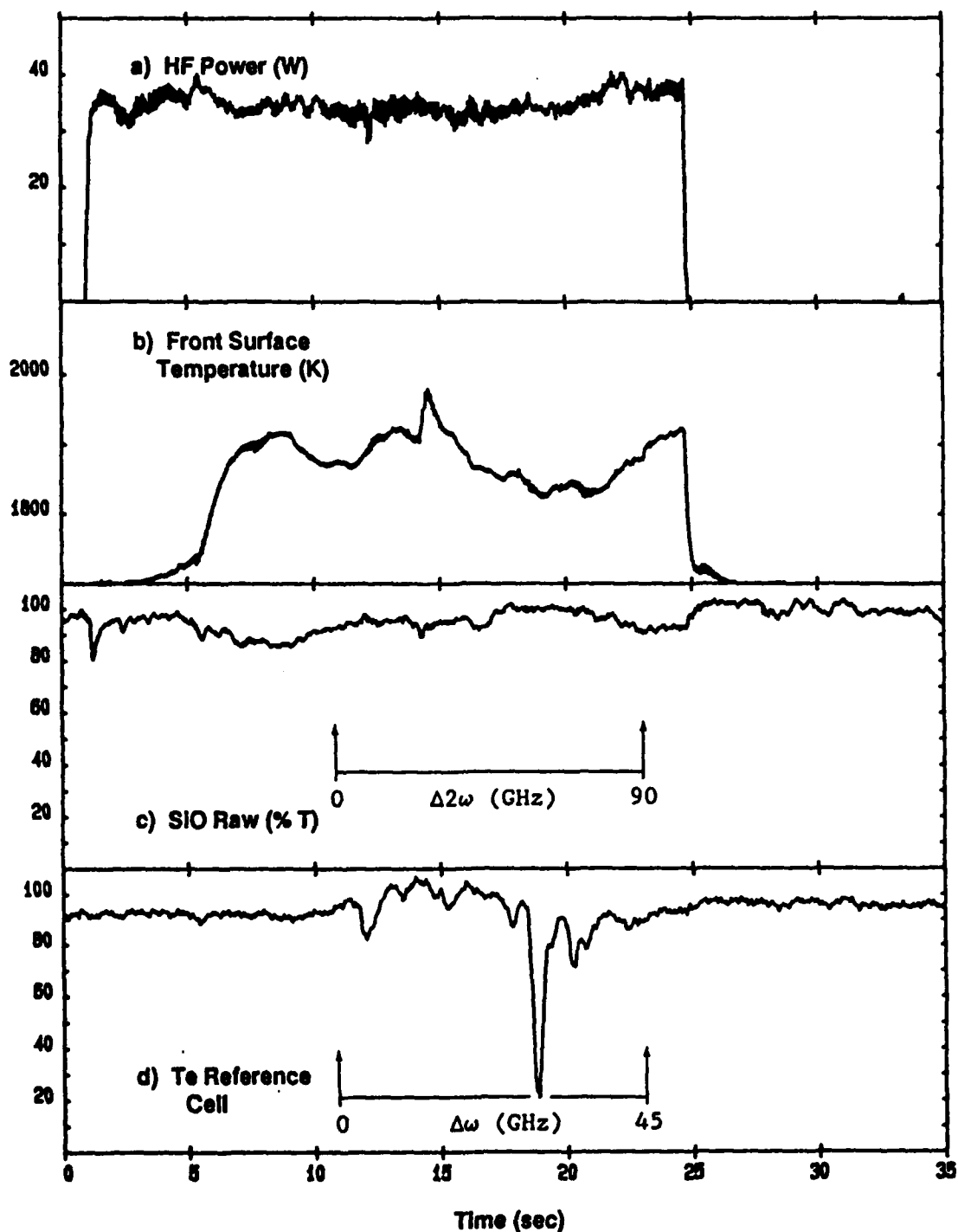


**Figure 25:** Data collected for a 200 torr oxygen environment, laser irradiation of MS7. The arrows in panels c and d mark the time CCLAS was scanning frequency, probing for SiO during the heating experiment. From the data in panel c, SiO was not detected.



#### Si<sub>3</sub>N<sub>4</sub> COATED C/C COMPOSITE (MS8):

Figure 26 shows data collected during the vacuum irradiation of MS8: no SiO was detected. Figure 27 shows data collected during the heating experiment with 5 torr oxygen in the chamber; no SiO was detected probably due to the low substrate temperature. This MS8 sample fell out of the holder during the dismount from the sample carousel. Therefore, the sample surface may have picked up debris from the vacuum chamber bottom plate. This MS8 specimen's pre test, post vacuum/laser irradiation, and post 5 torr oxygen/laser irradiation sample masses were 21.204 mg, 21.197 mg, and 18.256 mg, respectively.

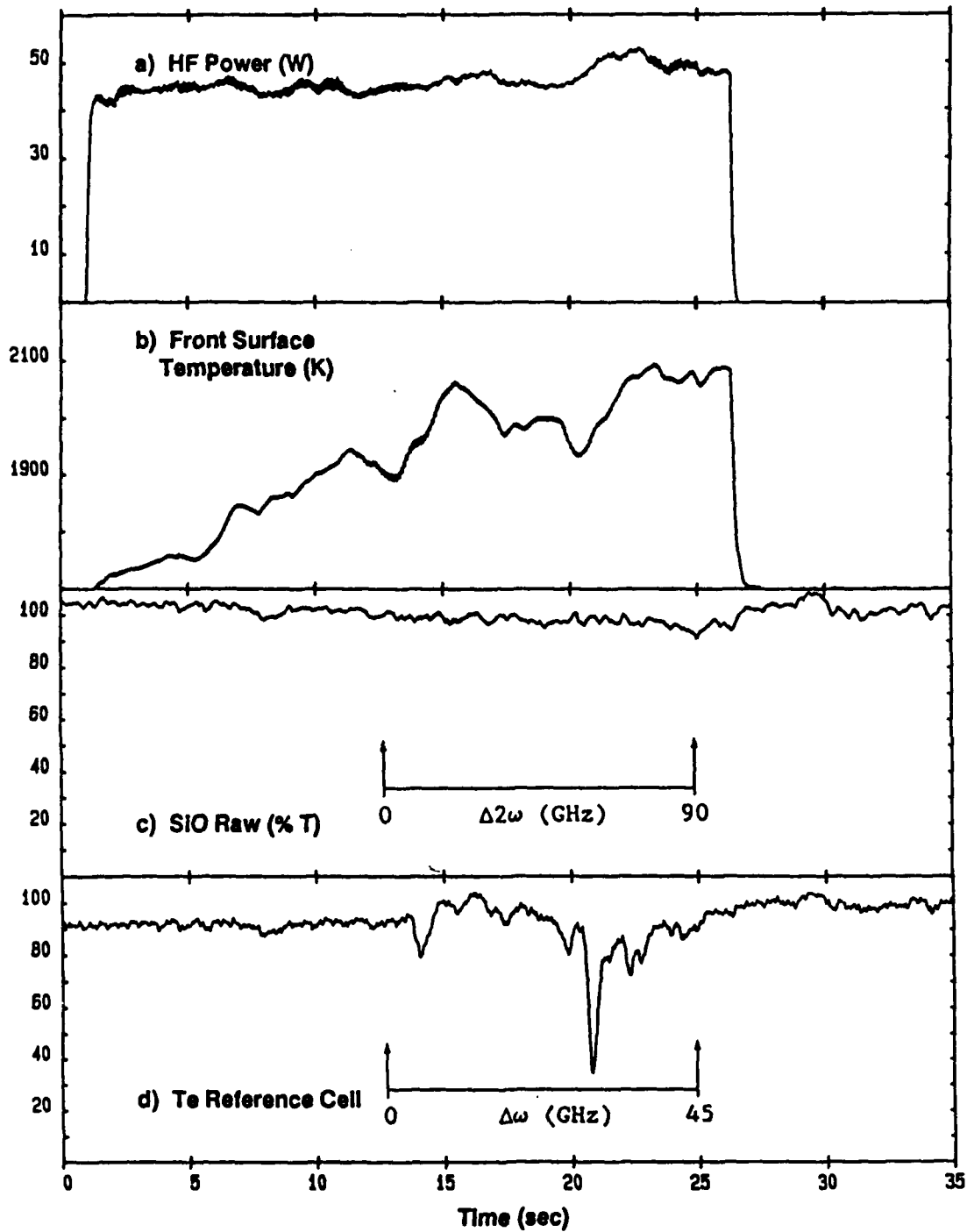
Another MS8 sample was heated to higher temperature as shown in Figure 28; SiO was detected. Visual inspection of the post test specimen showed substantial front surface modification; the entire coating may have been eaten away. Furthermore, glassy beads were formed on the tungsten sample holders and a bluish white coating was formed on the alumina supports. This MS8 specimen's pre and post test masses were 22.715 mg and 12.935 mg, respectively - a mass loss of 9.780 mg occurred during this experiment.

Figure 29 shows data collected during a temperature scan of a MS8 sample; 5 torr of oxygen was in the test chamber. A blue plume was only observed at the higher temperature range near the end of the scan. Visual inspection of post test specimen showed that glassy beads and a bluish white film had deposited on the alumina sample supports. Carbon fibers were found at the edge of the sample, and a "loose" film (or, possibly, a bubble) was formed on the back surface of the sample. This MS8 specimen's pre test and post test masses were 26.307 mg and 16.019 mg, respectively - a mass loss of 10.288 mg occurred during this experiment.

Figure 30 shows data collected on a MS8 sample held in a 200 torr oxygen environment; no SiO was detected, and no beam attenuation was observed. Visual observation of the sample during laser irradiation revealed a blue, hemispherical shaped plume. This MS8 sample fell from the holder during dismount from the carousel wheel. Apparently, the front surface was still intact with moderate film formation. Additionally, post test observation of the sample revealed that the substrate had "beaded" together or contracted

underneath the coating. Pre and post test sample masses were 21.001 mg and 12.561 mg, respectively - a mass loss of 8.440 mg occurred during the experiment.

# MS8: VACUUM: FREQUENCY SCAN



**Figure 26:** Data collected for a vacuum environment, laser irradiation of MS8. The arrows in panels c and d mark the time CCLAS was scanning frequency, probing for SiO during the heating experiment. Panel c shows no probe beam attenuation due to SiO.

# MS8: 5 TORR OXYGEN: FREQUENCY SCAN

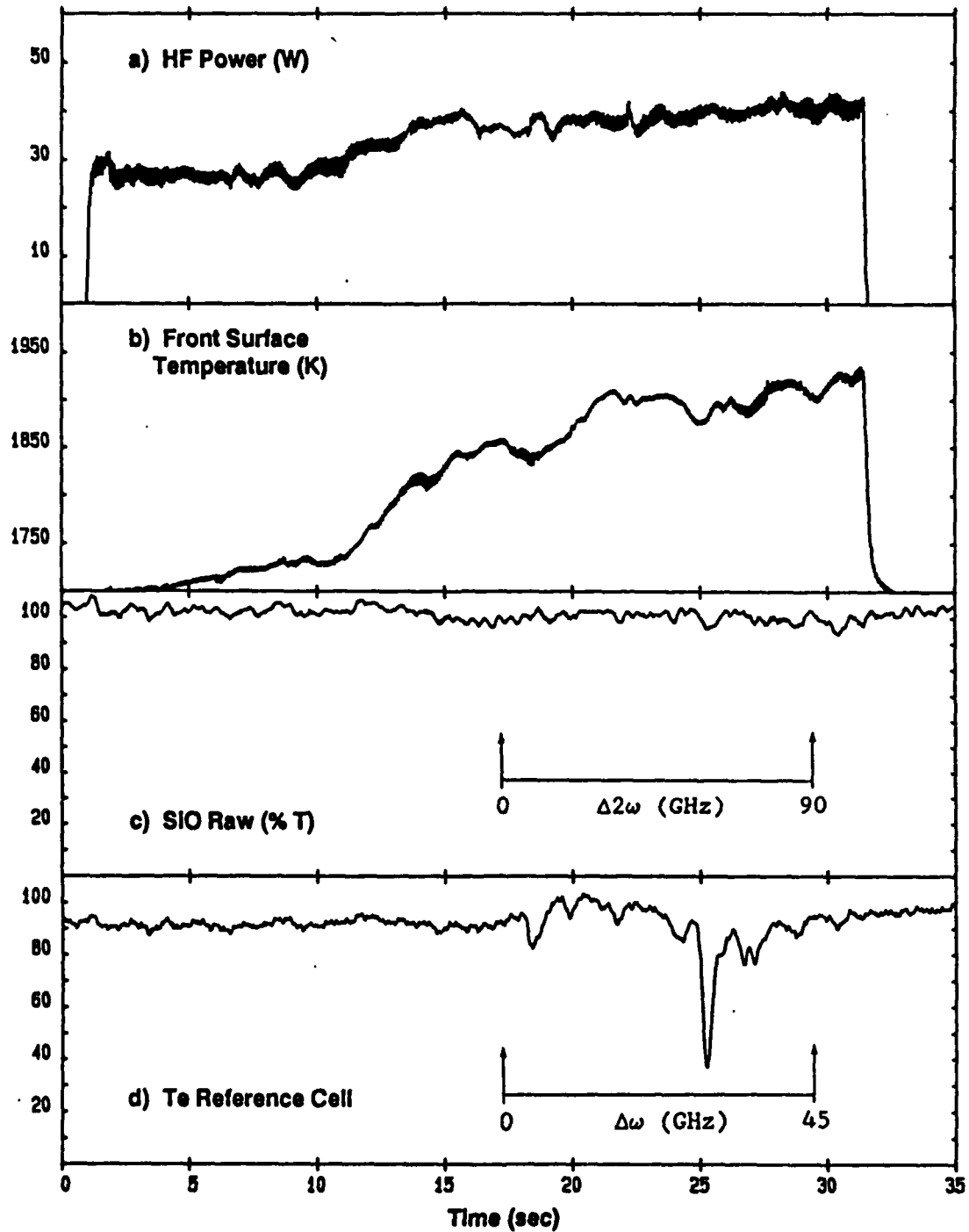


**Figure 27:** Data collected for a 5 torr oxygen environment, laser irradiation of MS8. The arrows in panels c and d mark the time CCLAS was scanning frequency, probing for SiO during the heating experiment. From the data in panel c, no SiO was detected.

# MS8: 5 TORR OXYGEN: FREQUENCY SCAN

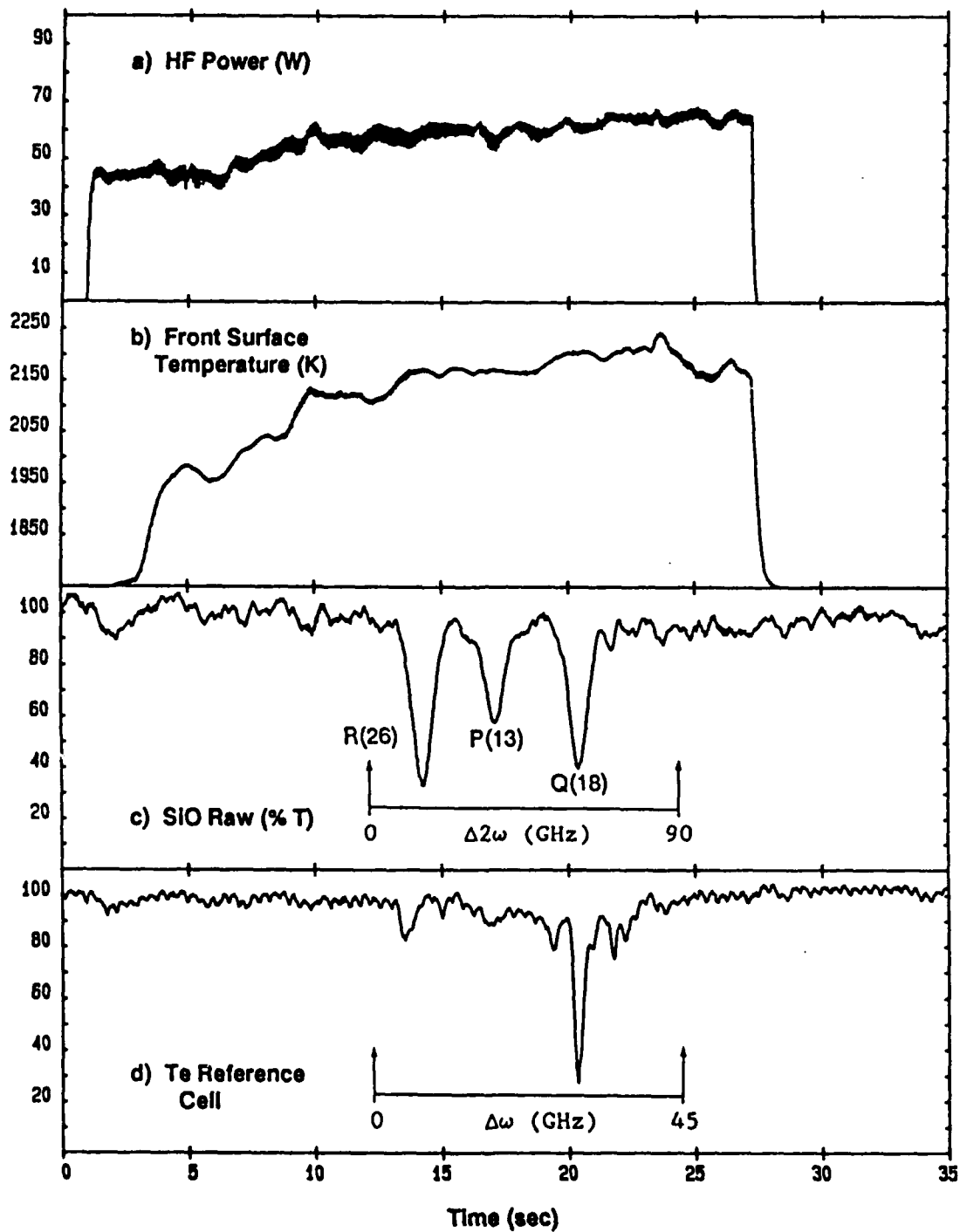


**Figure 28:** Data collected for a 5 torr oxygen environment, laser irradiation of MS8. The arrows in panels c and d mark the time CCLAS was scanning frequency, probing for SiO during the heating experiment. As evidenced by the three rotational transitions in panel c, SiO was detected.

### MS8: 5 TORR OXYGEN: TEMPERATURE SCAN

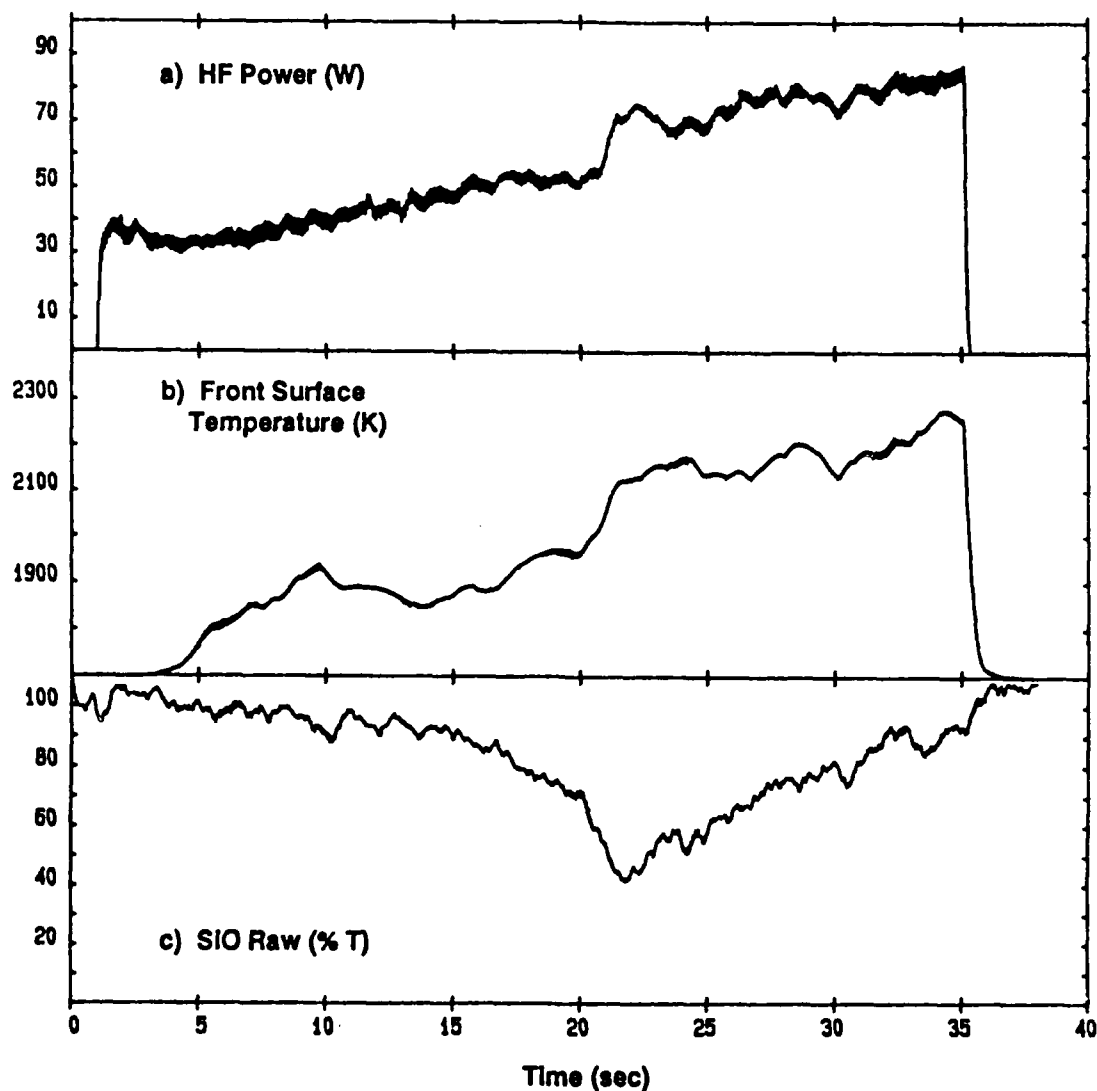


**Figure 29:** Data collected for a 5 torr oxygen environment, laser irradiation of MS8. The temperature of the sample was increased by manually increasing the HF laser power. The dye laser frequency was held stationary at the SiO A - X (0,0) Q(18) transition. Panel c shows the probe beam attenuation due to SiO.

# MS8: 200 TORR OXYGEN: FREQUENCY SCAN

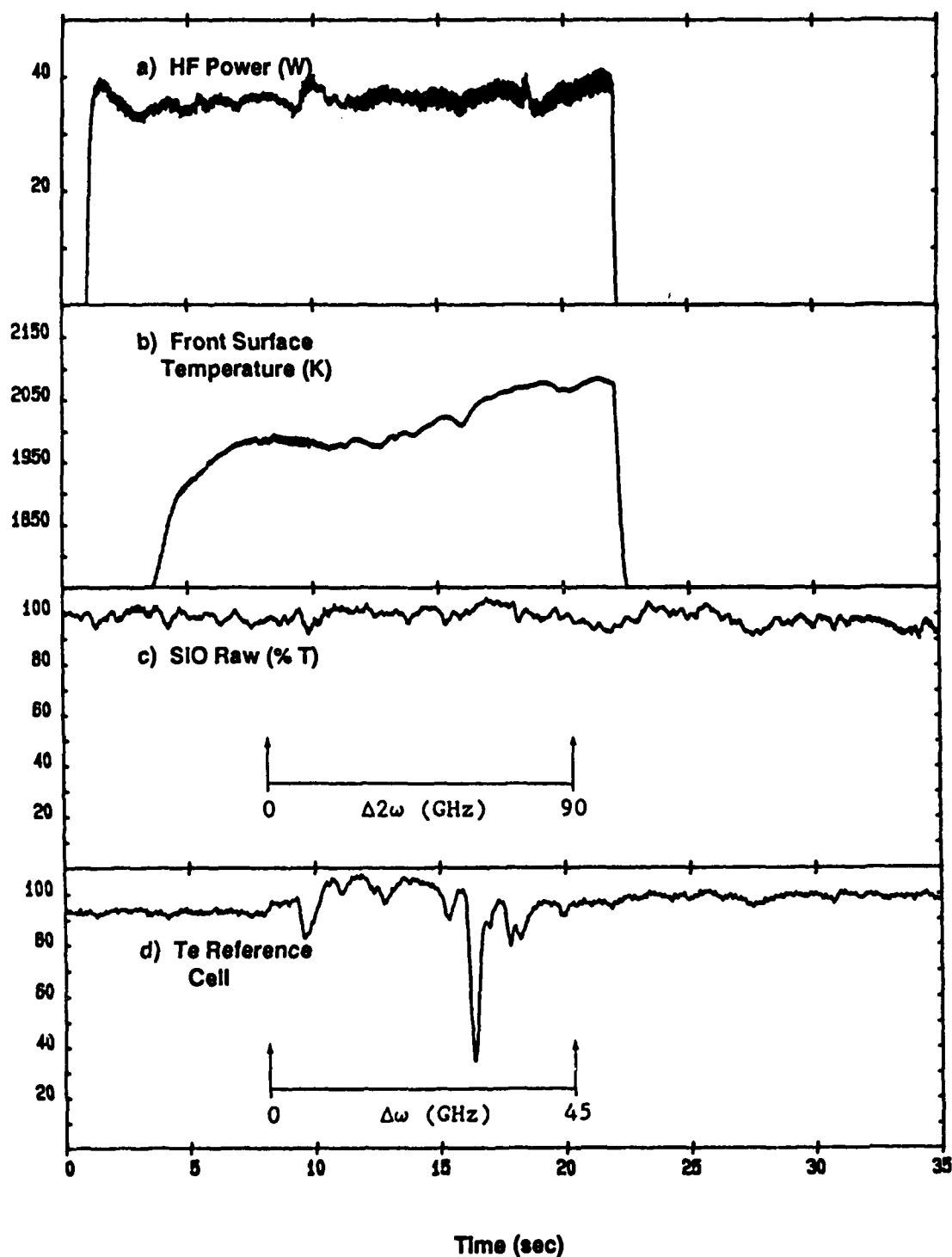


**Figure 30:** Data collected for a 200 torr oxygen environment, laser irradiation of MS8. The arrows in panel c and d mark the time CCLAS was scanning frequency, probing for SiO during the heating experiment. From the data in panel c, no SiO was detected.

#### 4.4 PRE- AND POST-TEST MICROSTRUCTURAL CHARACTERIZATION

Figure 31 shows the surface microstructure of the MS1 SiC standard in the as-received condition (top), after testing at 5 torr of O<sub>2</sub> (center) and after testing at 200 torr of O<sub>2</sub> (bottom). Testing in the active oxidation regime resulted in no protective film formation and heavy attack of the SiC as shown in the center photomicrograph. Attack appeared to be preferential at grain boundaries and was extremely rapid, corresponding to several mils thickness loss in a matter of only 30 seconds. In the center micrograph, some residual SiO<sub>2</sub> is present on the surface. This material probably condensed during cooling after the test. Testing in the passive oxidation regime (200 torr O<sub>2</sub>, bottom photomicrograph) resulted in a uniform, protective SiO<sub>2</sub> film and no significant attack of the substrate. SiO<sub>2</sub> "balls" are distributed over the uniformly oxidized specimen surface.

Figure 32 shows the surface microstructure of the MS2 Si<sub>3</sub>N<sub>4</sub> standard material. Testing in the active oxidation regime (center) resulted in attack of the Si<sub>3</sub>N<sub>4</sub> surface with no protective film formation and with generation of porosity in the surface. The exposure temperatures should have been high enough to cause dissociation of the Si<sub>3</sub>N<sub>4</sub>, generating N<sub>2</sub>. This is believed to be the most likely cause of the porosity. The rate of active oxidation attack was significantly less than for MS1. Testing in the passive oxidation regime (bottom photomicrograph) resulted in heavy SiO<sub>2</sub> film formation. The presence of holes in the SiO<sub>2</sub> film suggests that the Si<sub>3</sub>N<sub>4</sub> dissociation was probably occurring under the SiO<sub>2</sub> layer as might be expected.

Figure 33 shows the surface microstructure of the MS3 SiC/SiC composite. No surface seal coating was present on the as-received surface. Testing in the active oxidation regime (center photomicrograph) resulted in no protective film formation and heavy attack of the composite (several mils in 30 seconds). Note that the matrix phase appears to be attacked somewhat faster than the fiber phase and that the attack of the composite as a whole is quite non-uniform, with one large



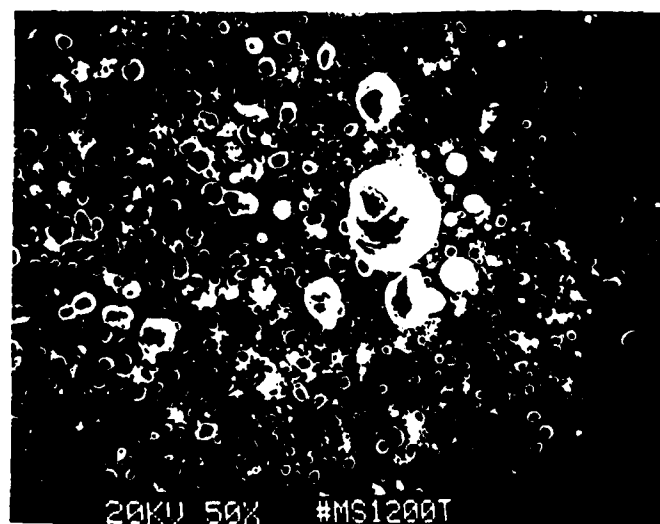
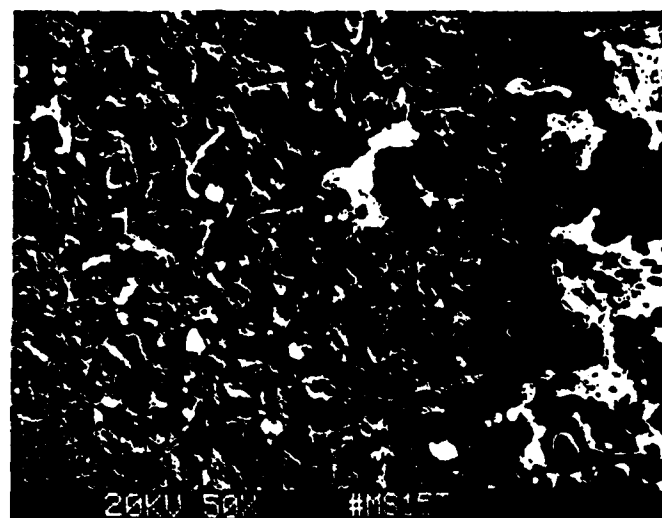
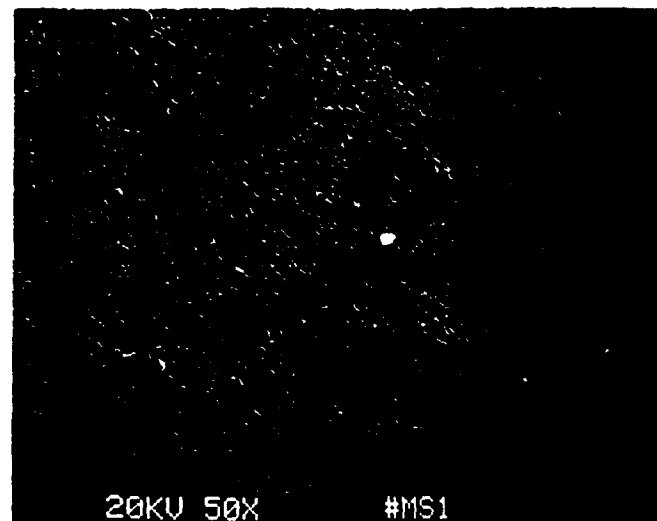


Figure 31. Surface microstructures of material MS1. Top, as received. Center, after testing in 5 torr O<sub>2</sub>. Bottom, after testing in 200 torr O<sub>2</sub>.

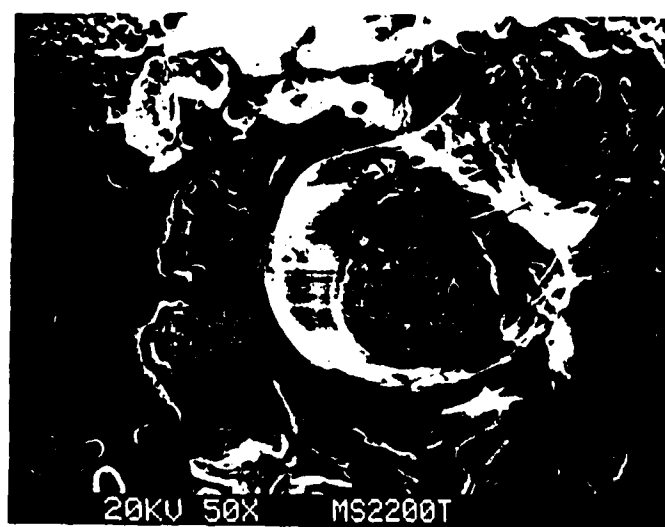
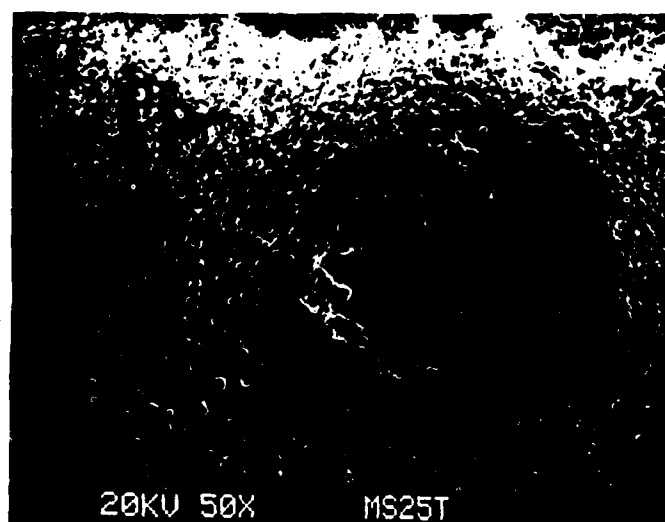


Figure 32. Surface microstructures of material MS2. Top, as received. Center, after testing in 5 torr O<sub>2</sub>. Bottom, after testing in 200 torr O<sub>2</sub>.

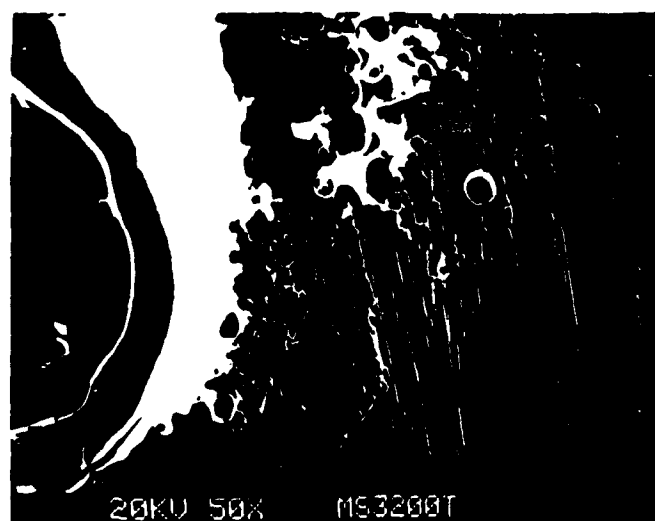
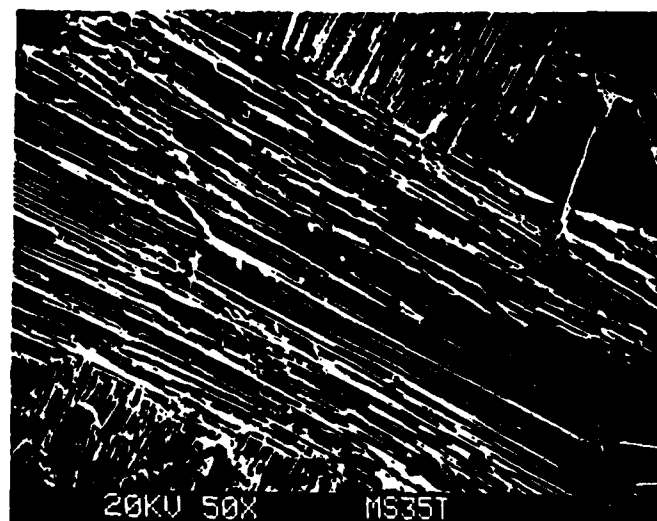
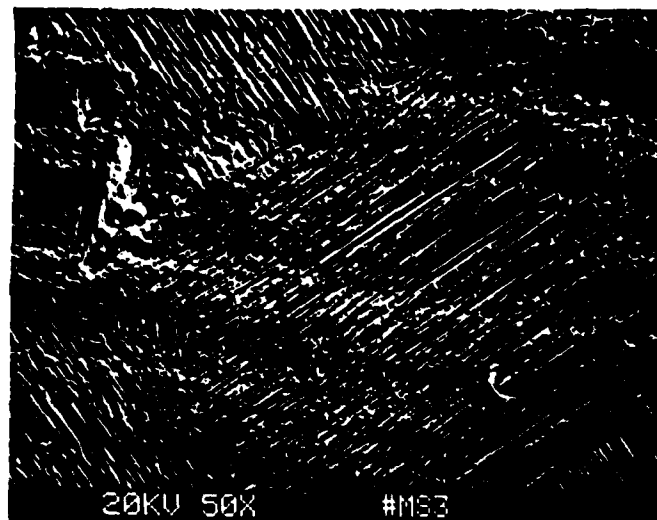


Figure 33. Surface microstructures of material MS3. Top, as received. Center, after testing in 5 torr O<sub>2</sub>. Bottom, after testing in 200 torr O<sub>2</sub>.

hole extending far into the remaining material. In the passive oxidation regime (bottom photomicrograph) the edge of the  $\text{SiO}_2$ -covered region (to the left in the field of view) is shown. Figure 34 shows the center region of the crater in the left half of the bottom photomicrograph of Figure 33 at a higher magnification. Although  $\text{SiO}_2$  was formed and the attack was much less than in the active oxidation regime, Figure 34 shows that fibers have been lost and that an  $\text{SiO}_2$  replica of the matrix phase remains.

Figure 35 shows the surface microstructure of the MS7  $\text{SiC}$ -coated carbon/carbon composite. Testing in the active oxidation regime (center photomicrograph) resulted in virtually complete removal of the coating (ca. 10 mils in 30 seconds), although the remaining sealed, inhibited substrate appears largely undamaged. In the passive oxidation regime (bottom photomicrograph) a  $\text{SiO}_2$  film is present but the film has been disrupted in numerous places by bubble formation, which is not unexpected at the temperatures attained. As noted in the discussion of thermochemical modeling in Appendix 1, such bubble formation may be relatable to inhomogeneities in the coating microstructure. It should be noted that MS6, an uncoated version of MS7, was also tested, but disappeared almost instantaneously, leaving no residual microstructure other than a few beads of a material believed to be a  $\text{B}_2\text{O}_3$ -based glass composition.

Figure 36 shows the surface microstructure of the MS8,  $\text{Si}_3\text{N}_4$ -coated carbon/carbon composite. Testing in the active oxidation regime (center photomicrograph) resulted in slight attack of the coating surface (much less than 1 mil in 30 seconds) and no protective film formation. Fine porosity is distributed over the coating surface, indicating likely  $\text{Si}_3\text{N}_4$  dissociation, but on a much finer and more uniform scale than for the MS2 standard. Several cracks can be seen in the residual coating. Testing in the passive oxidation regime (bottom photomicrograph) resulted in a uniform  $\text{SiO}_2$  film over a virtually undamaged as-received coating surface (compare the top and bottom photomicrographs). Several  $\text{SiO}_2$  "balls" are present on the surface, as are a few "needles" of unknown material. In the upper right there is a structure suggestive of a broken bubble.

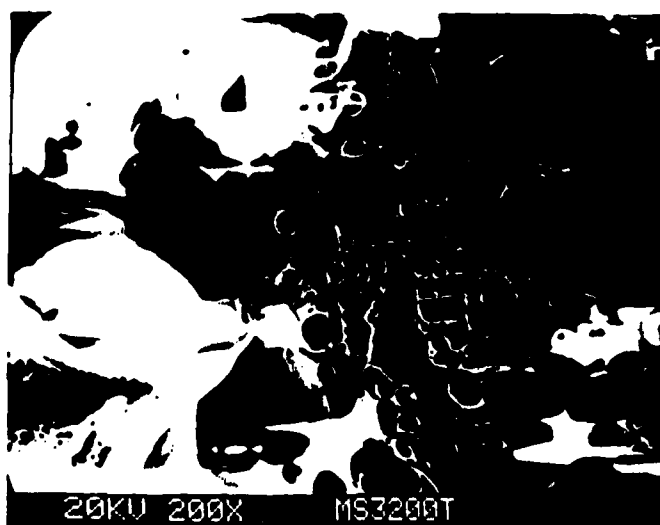


Figure 34. Higher magnification micrograph of the central region of the  $\text{SiO}_2$  crater to the left of Figure 33 (bottom).

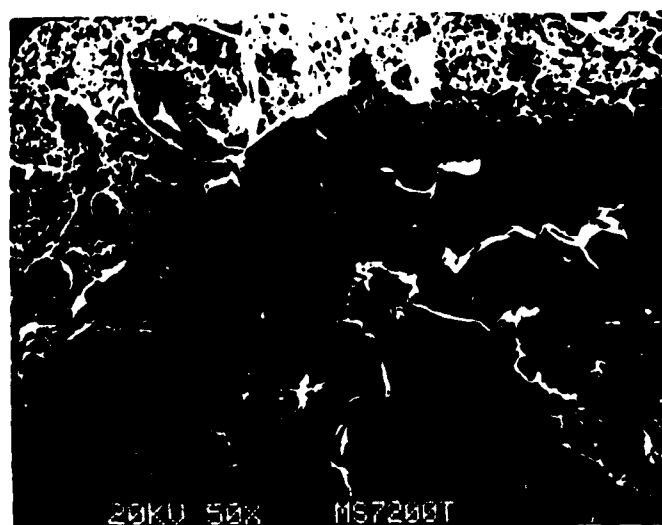
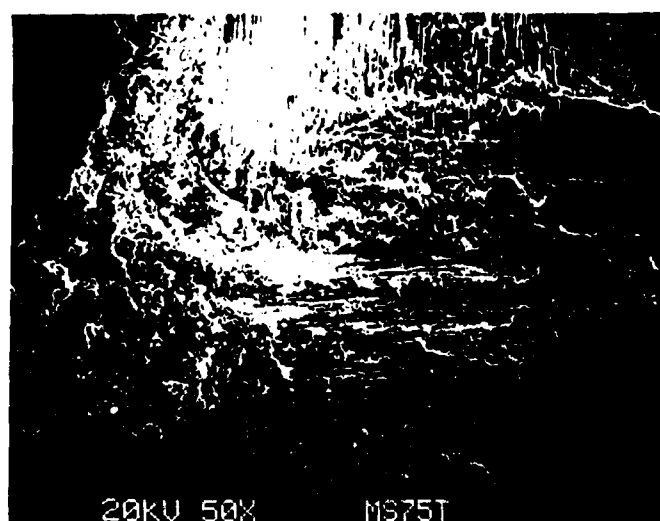
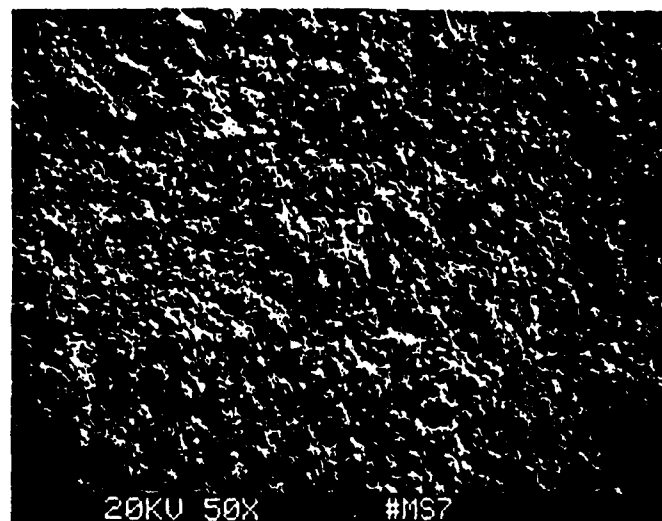


Figure 35. Surface microstructures of material MS7. Top, as received. Center, after testing in 5 torr O<sub>2</sub>. Bottom, after testing in 200 torr O<sub>2</sub>.

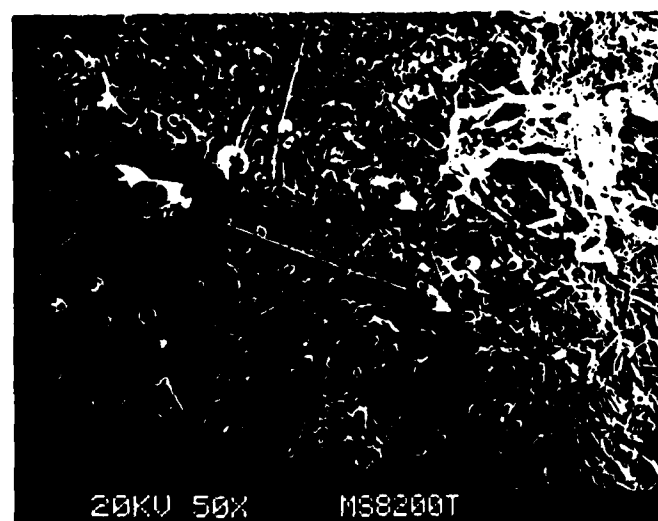
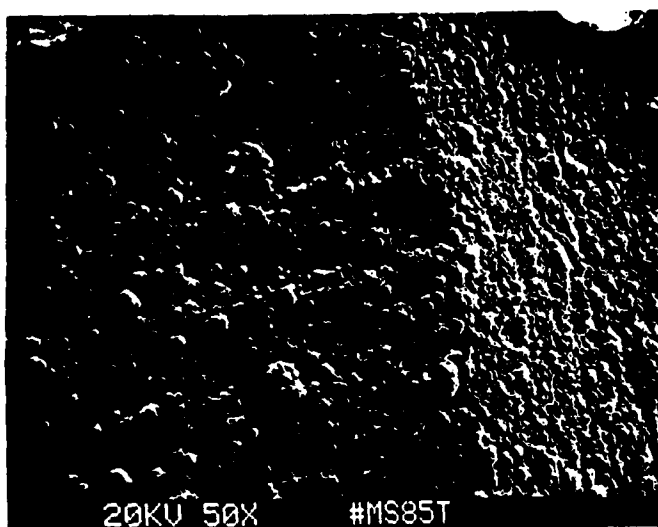
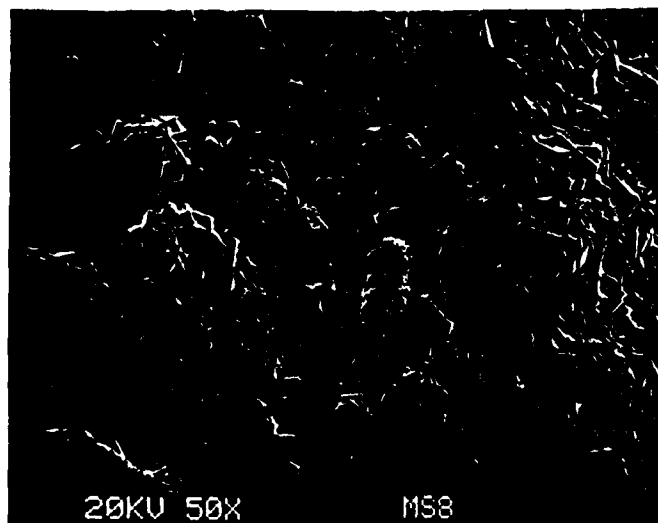


Figure 36. Surface microstructures of material MS8. Top, as received. Center, after testing in 5 torr O<sub>2</sub>. Bottom, after testing in 200 torr O<sub>2</sub>.

## 5.0 CORRELATION OF MODELING AND EXPERIMENTAL OBSERVATIONS

The details of thermochemical and kinetic modeling are presented in Appendix 1.

The general agreement between the modeling predictions and behavior is good. Across the sample set, there was no spectroscopic detection of SiO on vacuum exposure. If there were significant oxygen impurities in the materials, or if they had been exposed to an oxidizing conditions for sufficient time and temperature, a transient release of SiO would be predicted. With the present data an estimate of the expected signal cannot be made, but the method shows promise of significant sensitivity improvements such that measurements of transient phenomena are a reasonable objective.

The general observation in those tests which were carried out under an oxygen pressure of 5 torr was that of active oxidation, with very rapid loss of material from most samples. If the temperature-pressure conditions employed in this series are examined in the light of Figure 7 of Appendix 1, which presents critical oxygen pressures as a function of temperature for various assumed mechanisms for the active/passive transition, it will be seen that the experimental conditions, in general, lie in the active oxidation domain at 5 torr O<sub>2</sub> pressure

Interesting exceptions are to be found in the cases of MS2 and MS8. These materials both present an Si<sub>3</sub>N<sub>4</sub> surface to the heating beam. It will be noted in Figure 13, a frequency scan of MS2, the temperature remained in the 1850 K range, or less. No SiO was detected by the laser probe. In Figure 14, again a frequency scan, the temperature ranges around 2000 K and the SiO spectrum is clearly obtained. Again with MS8, a first frequency scan (Figure 27) reached about 1900 K and the probe detected no SiO. In a second scan (Figure 28) the temperature ranged to perhaps 2150 K and the SiO spectrum is found.

It is possible that there was active oxidation in the lower temperature range, but at a rate too low for probe protection. It can



also be noted, however, that for the lower temperature scans the operating conditions lie above the line defined by the data of Hinze and Graham (Reference 4, Appendix 1) in Figure 7 of Appendix 1. The fact that both the Hinze and Graham active/passive transition data and these two laser probe observations lie significantly below the theoretical lines for simple gas phase transport control suggest that the details of the active/passive transition may be complex.

Testing under 200 torr oxygen pressure failed to detect SiO in any case. In the passive regime there is no release of SiO from the ideal film. If the film is imperfect some transient release may occur that is below probe detection, at current sensitivities. Some clear pressure effects were observed in the 200 torr scans. In the data related to Figure 11, the temperature ranged up to 2200 K,  $1/T = .45 \times 10^{-3}$ . As shown in Figure 1 of Appendix 1, the total interfacial pressure, consisting of SiO plus CO, would reach some 3 atm. under these conditions.

Though the results are ambiguous, the active oxidation regime results suggest a significant correlation between temperature and SiO absorption of the probe. Figures 9, 19, and 20 appear to show such a correlation. In particular, the probe absorption is higher at higher temperatures, indicating a high SiO concentration and rate of production. There are clearly some temperature scans in which this correlation is not found, though some may be attributable to coating burnthrough in the case of coated materials.

The correlation of the temperature and rate in the active regime relates directly to the question of the mechanism. If the process is controlled by gas phase diffusion only a weak temperature dependence is expected. If, on the other hand, the process is limited by a chemical reaction step or other process with a substantial activation energy, the a strong dependence of rate on temperature would be expected.

## 6.0 CONCLUSIONS AND RECOMMENDATIONS

Laser probe spectroscopy has been clearly demonstrated as a method for observing SiO in the near-surface environment of SiC and Si<sub>3</sub>N<sub>4</sub> and of materials coated with SiC or Si<sub>3</sub>N<sub>4</sub> during active oxidation at low oxygen pressures. Samples tested at higher oxygen pressures, predicted to lie within the passive oxidation regime, did not provide measureable SiO signals but visual and micrographic examination of the sample showed evidence of significant interfacial attack in some materials, as predicted from general considerations of the thermochemical and kinetic model.

Both in terms of sample requirements and operational testing time the combination of the laser probe with metallographic examination is extremely promising. Tests to provide preliminary characterization of materials can be carried out with minimal amounts of material

There are a number of ways that the application of this facility to the investigation of high temperature materials can be made more powerful.

All of the tests reported here were carried out using an HF laser to provide the heating source. While this laser provides more than adequate power, it is relatively unstable in output and costly to run for extended periods. In future work a CO<sub>2</sub> laser will be available as the heating source. The CO<sub>2</sub> laser is very stable and can easily be operated for extended time periods.

Coupled with feedback from the pyrometer to provide temperature control, the CO<sub>2</sub> laser would provide the capability of carrying out investigations in which the sample could be carried through a sequence in which a protective layer can be established by controlled, in situ, oxidation at intermediate temperature and subsequently either raised to a temperature that induces failure or return to low oxygen pressures, in the active oxidation domain, and the process of breakdown of passivity explored.

It is doubtful that the perfect film, i.e. uniform and flawless, accurately describes real world materials. It is by no means clear that in, say, a cracked film, SiO will reach the free surface. Exploration of samples in the passive oxidation regime with increased sensitivity would be desirable and there are a number of means by which this could be achieved. At the spectrum selective level, both the vibrational and rotational transition selection could be changed to features with increased transition probability or cross section. It is estimated that a factor of 5 increase in sensitivity should be attainable by this means. Further increase in sensitivity could be achieved by ratioing the signal to the output power of the probe laser. An overall sensitivity increase of three orders of magnitude should be attainable.

The applicability of the method could be extended by identifying an appropriate spectral feature for the determination of BO from boron-containing species. A desirable, but more difficult, extension would involve the direct detection of CO.

Although samples cut from larger pieces can be used, as has been demonstrated, the availability of samples with all sides coated would provide the opportunity to correlate other observations with weight changes. Currently weight changes of samples cut from coated materials would include any reaction of the uncoated edge or back side of the sample.

Modeling development should be fruitful both to more closely examine the results in thermochemical terms, but also to better characterize the technique. Samples have been, and very likely will continue be, heated with a laser beam smaller than the sample dimension. The heat flux into the sample takes the form of a roughly Gaussian distribution. This needs attention in our examination of the data.

With thoughtful development, laser probe testing can be expected to provide a reliable and meaningful tool for the testing and evaluation of high temperature composites and their constituent material. The method

may also provide a basis for estimating long term performance from short term testing.

## REFERENCES

1. R.W. Field, A. Lagerqvist, and I. Renhorn, *Physica Scripta*, 14, 298 (1976).
2. G. Herzberg, Molecular Spectra and Molecular Structure. I. Spectra of Diatomic Molecules. 2nd edition, 1950 (Van Nostrand Reinhold).
3. R.P. Main, A.L. Morsell, and W.J. Hooker, *J. Quant. Spectrosc. Rad. Trans.*, 8, 1527 (1968).
4. W.H. Smith and H.S. Liszt, *J. Quant. Spectrosc. Rad. Trans.*, 12, 505 (1972).
5. A. Czernichowski and W. Zyrnicki, *Acta Physica Polonica*, A37, 865 (1970).
6. O. Kubaschewski and T.G. Chart, *J. Chem. Therm.*, 6, 467 (1974).

## APPENDIX 1

### MODELING

#### 1.0 Introduction and Summary

A major objective of the modeling carried out in this program was to identify the conditions under which the test materials might be expected to fail as a consequence of the interaction between any protective layer formed by oxidation and its substrate, which may be either a protective coating or composite substrate material, and to identify the expected gaseous species. The results are presented in Section 2., thermochemical calculations.

In addition available kinetic models were examined from the viewpoint of expectations in spectroscopic examination of the near-surface gaseous environment. The results of these consideration are presented in Section 3.

#### 2.0 Thermochemical Calculations

In principle, all of the materials examined experimentally, presented an outer surface of SiC or Si<sub>3</sub>N<sub>4</sub>. For each of these of utility in a high temperature oxidizing environment is based on the formation of a protective layer of SiO<sub>2</sub>. One of the limits encountered by such materials derives from the interaction of the SiO<sub>2</sub> layer with its substrate to produce gaseous species at pressures sufficient to disrupt the film. These reactions have been examined, considering both the pressures and compositions of the gaseous products.

Chemically vapor deposited SiC or Si<sub>3</sub>N<sub>4</sub> coatings in general contain some excess Si. SiC, in addition, contains free C and in any case there is the potential for interaction with the carbon substrate when the objective is a carbon/carbon composite protection system. For these reasons, the interaction of SiO<sub>2</sub> with Si and C have also been examined.

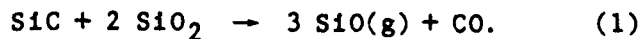
In addition, while not examined experimentally, a number of carbon/carbon composites contain boron as an oxidation inhibitor. The mechanism of protection again depends on the ability of an oxide,  $B_2O_3$  in this case, to limit the access of oxygen to the underlying matrix.

Finally, a proposed complex ultrahigh temperature composite is examined.

The thermochemical evaluation is based on an idealized protective layer. While the analysis points to temperatures at which the protective layer might be expected to fail via film disruption it can neither precisely define these conditions, which depend on viscosity and surface tension factors, nor evaluate the rate of oxidation, which may become unacceptable even with an intact layer.

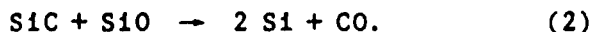
## 2.1 SiC/SiO<sub>2</sub>

Over most of the temperature range the interaction can be described by the reaction



This reaction produces SiO and CO a ratio of three to one.

Both CO and SiO are unusual in that their stability, measured by the free energy of formation, increases with increasing temperature. CO is, however, more stable than SiO, and increasingly so at higher temperatures. At the high end of the temperature interval considered the composition of the gaseous products involves the additional reaction



The equilibrium constant for this reaction takes the form

$$K = P_{\text{CO}}/P_{\text{SiO}} \quad (3)$$

So long as the value of  $K$  is less than  $1/3$  the products are as indicated by reaction (1). From the tabulated thermodynamic data the temperature at which  $K$  for reaction (2) equals  $1/3$  is found to be 2011 K, based on the relation

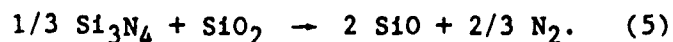
$$T = \frac{\Delta H}{\Delta S - R \ln K} \quad (4)$$

Above this temperature the CO/SiO ratio increases and silicon would be expected from the reaction.

The results for this system are presented in Fig. 1. The total pressure reaches 1 atmosphere at 1800° C (3300° F).

## 2.2 Si<sub>3</sub>N<sub>4</sub>/SiO<sub>2</sub>

The stoichiometric reaction between the protective layer and the substrate can be described by the reaction



In addition, the nitride can decompose directly by the reaction



Above 1652 K the nitrogen pressure from (6) exceeds that estimated from the stoichiometric reaction (5). The procedure for estimating pressures above that temperature was to use the nitrogen pressure from the decomposition reaction in solving the equilibrium equation for reaction (5) for SiO.

The results are shown in Fig. 2. Only the N<sub>2</sub> pressure is shown above



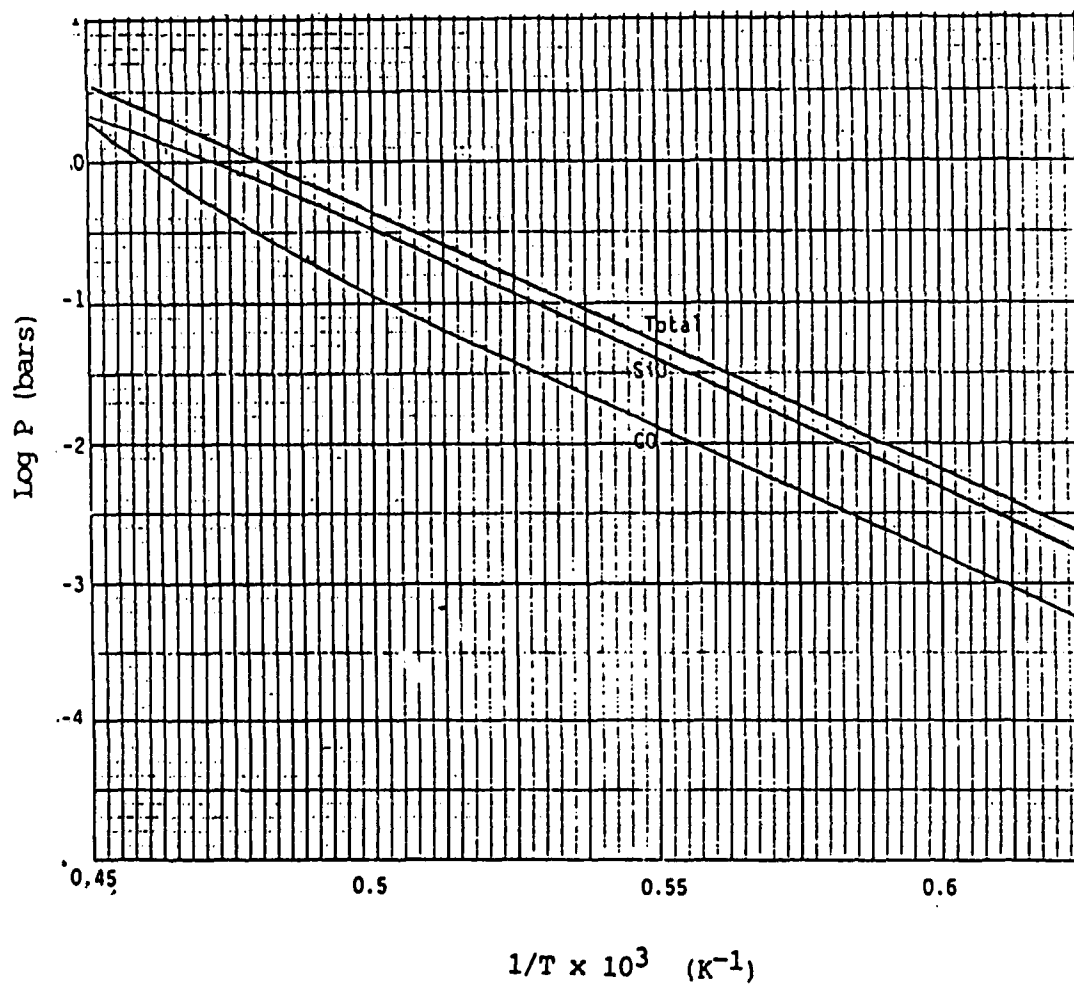


Fig. 1

Log  $P_{\text{SiO}}$ ,  $P_{\text{CO}}$ , and  $P_{\text{total}}$  vs.  $1/T$  for the interaction of  $\text{SiO}_2$  and  $\text{SiC}$ .

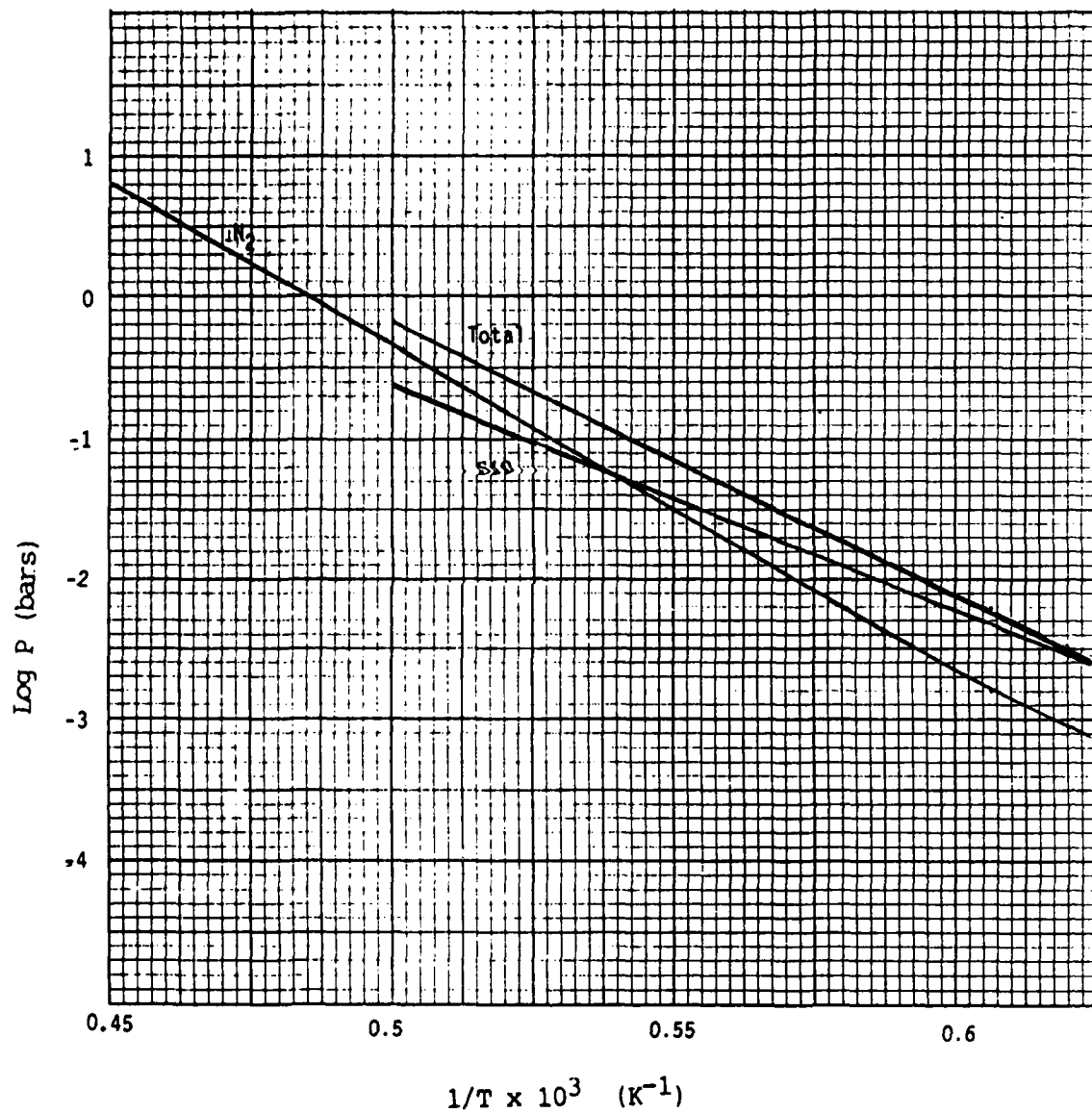
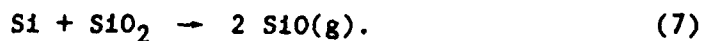


Fig. .  
 Log  $P_{\text{SiO}}$ ,  $P_{\text{N}}$ , and  $P_{\text{total}}$  vs.  $1/T$  for the interaction of  $\text{SiO}_2$  and  $\text{Si}_3\text{N}_4$ .

2000K. The free energy of reaction (6) becomes zero at 2067 K. Assuming a one atmosphere limit, reaction (5) then becomes equivalent to the reaction of  $\text{SiO}_2$  with Si.

### 2.3 $\text{SiO}_2/\text{Si}$

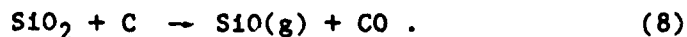
The basic reaction is



There are no complications from multiple species in this case. The calculated results are shown in Fig. 3.

### 2.4 $\text{SiO}_2/\text{C}$

For the reaction of  $\text{SiO}_2$  with carbon it is convenient to start with the stoichiometric reaction



However, since the free energy of formation of CO is more negative than that of SiO, i.e. CO is more stable, it is also necessary to consider the reaction



The equilibrium constant for (7) has the form,

$$K = (\text{SiO})(\text{CO}), \quad (10)$$

while the equilibrium constant for (8) has the form,

$$K = (\text{CO})/(\text{SiO}). \quad (11)$$

The two expressions together determine the system. In evaluation it

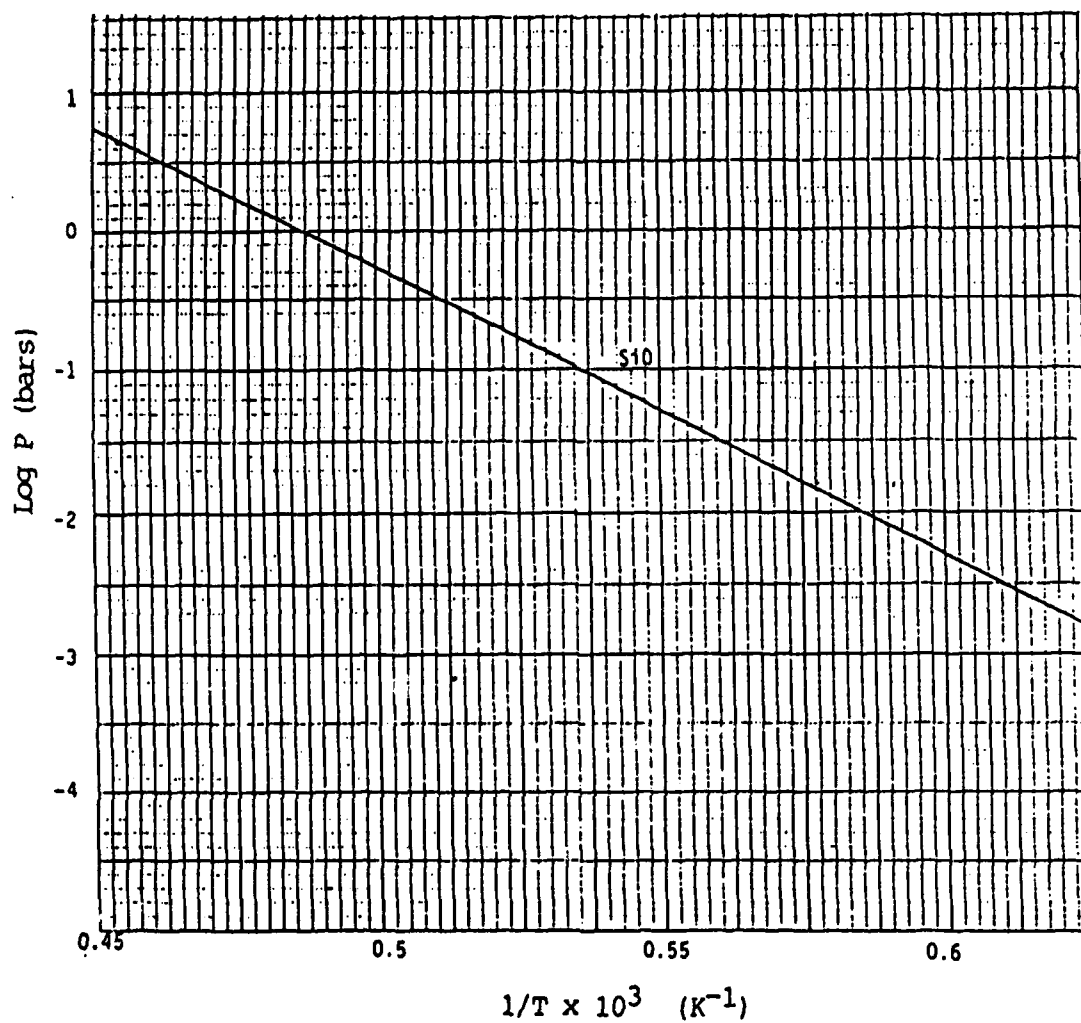


Fig. 3

Log P<sub>SiO</sub> for the interaction of SiO<sub>2</sub> and Si.

will be found that the CO/SiO ratio is always greater than unity. This implies that Si will also form in the SiO<sub>2</sub>/C reaction.

The pressures in the SiO<sub>2</sub>/C system are shown in Fig. 4.

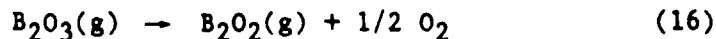
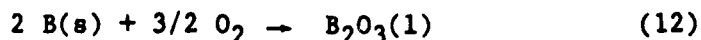
## 2.5 Boron-Based Inhibition Systems

The uncoated substrates for some carbon/carbon composites contain elemental boron and zirconium diboride to inhibit oxidation. It is assumed that the inhibition effect is via the formation of a B<sub>2</sub>O<sub>3</sub> layer which reduces direct access of oxidants to the composite substrate.

Although the equilibrium form for boron in the carbon-carbon composite system would be B<sub>4</sub>C, under fabrication conditions the boron remains primarily as elemental boron, with only a small amount present as the carbide on the basis of x-ray diffraction results (1).

The system is therefore treated to be C, B, B<sub>2</sub>O<sub>3</sub>, and ZrB<sub>2</sub> as condensed phases and the pressures of potential gaseous species are calculated. The oxygen source is the B<sub>2</sub>O<sub>3</sub>. The oxygen activity, or pressure, can be calculated from either the B/B<sub>2</sub>O<sub>3</sub> or the C/B<sub>2</sub>O<sub>3</sub> equilibrium. The former was chosen.

The reactions considered are the following:



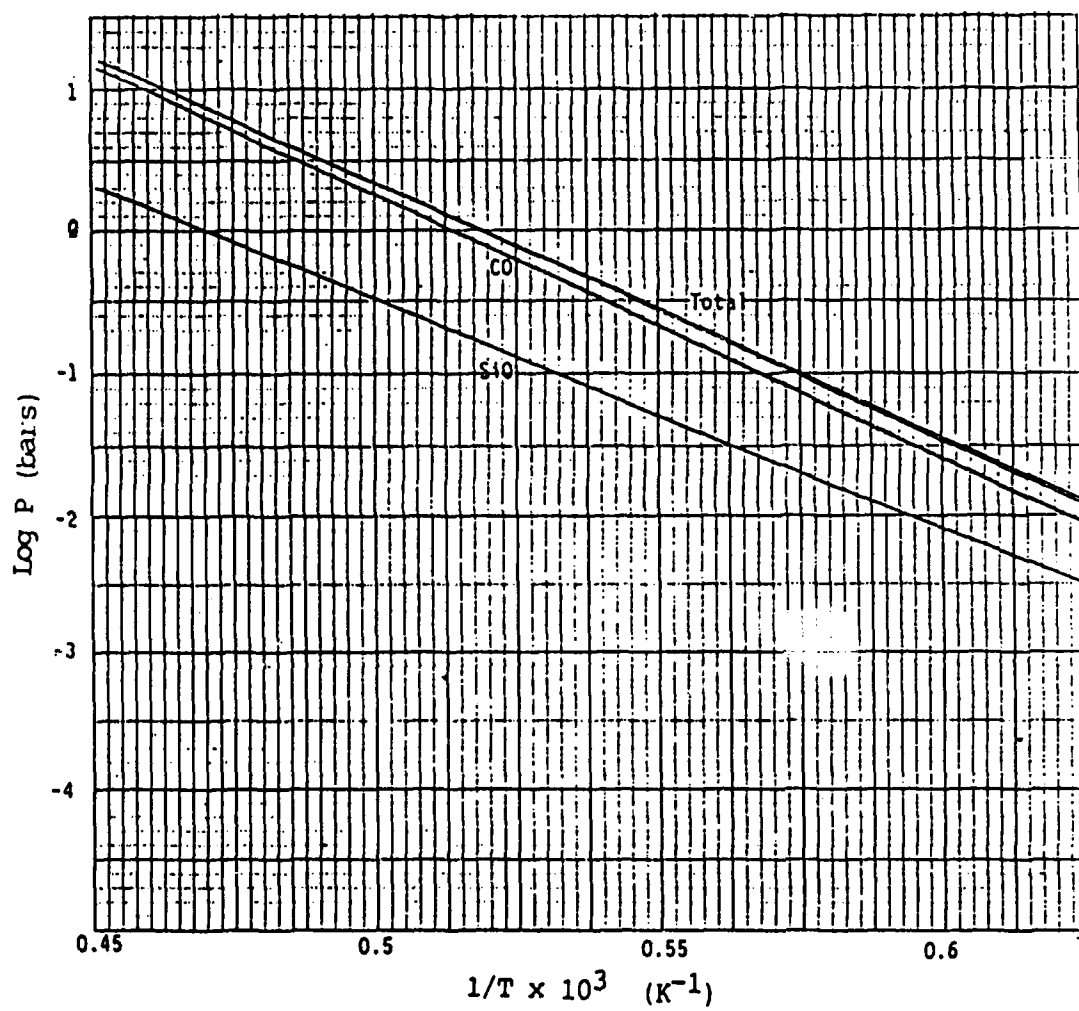


Fig. 4

Log  $P_{\text{SiO}}$ ,  $P_{\text{CO}}$ , and  $P_{\text{total}}$  vs.  $1/T$  for the interaction of  $\text{SiO}_2$  and C.



The results of the calculation are shown in Fig. 5. It will be noted that CO is the dominant species and that BO, the most accessible to spectroscopic measurement, is relatively rare.

## 2.6 Summary of Simple Coating and Inhibition Cases

Gas compositions of the order calculated for the  $\text{SiO}_2$  substrate might be observable in the very earliest stages of  $\text{SiO}_2$  layer formation or, possibly, under bubble failure conditions. It should be recognized that in cases where oxygen access and product removal occur via mechanical defects in the protective  $\text{SiO}_2$  layer the composition of the product gas phase will not, in general, correspond to that of the  $\text{SiO}_2$ /substrate interface. In such cases the kinetics of reactions to the stable oxidized species,  $\text{SiO}_2$  and  $\text{CO}_2$ , will ultimately determine the possibility of observing the predicted interfacial species.

The total pressures at several temperatures in the  $2500^\circ\text{--}3500^\circ\text{F}$  range are presented in Table 1.

Table 1.

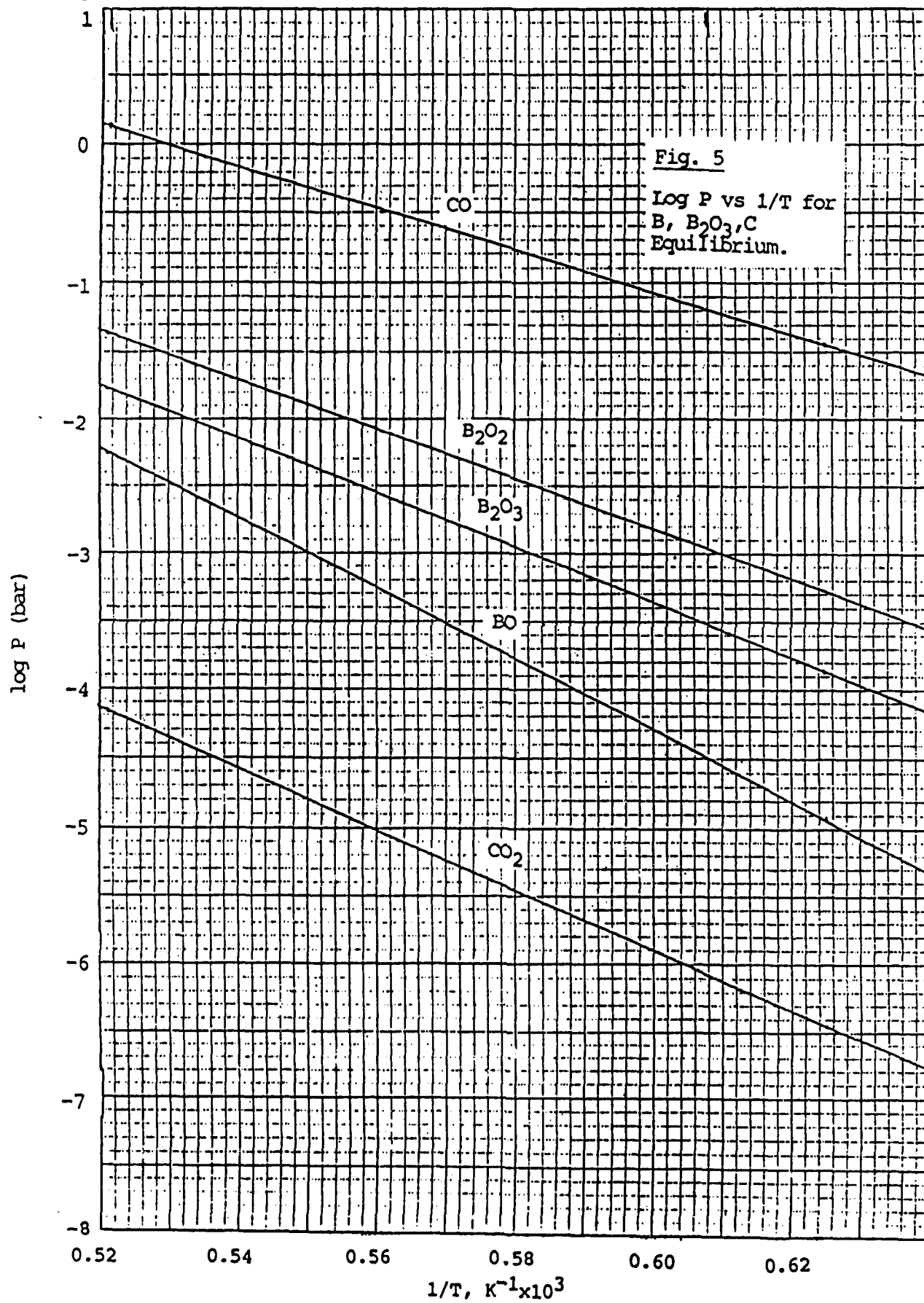
<u>T, °F</u>	<u>Total Pressure, Bars</u>			
	$\text{SiO}_2/\text{SiC}$	$\text{SiO}_2/\text{Si}_3\text{N}_4$	$\text{SiO}_2/\text{C}$	$\text{SiO}_2/\text{Si}$
2500	$5 \times 10^{-3}$	$6 \times 10^{-3}$	$2.5 \times 10^{-2}$	$3.5 \times 10^{-3}$
2750	$3 \times 10^{-2}$	$4 \times 10^{-2}$	0.18	$3 \times 10^{-2}$
3000	0.18	0.26	0.93	0.21
3250	0.98	1.0	4.2	1.0
3500	3	5	15	4

In general, the pressures observed at the  $\text{SiO}_2/\text{X}$  interface are very similar, except in the case of carbon. So far as film disruption by bubble formation is concerned, carbon is clearly the most aggressive.

3000° F

2500° F

Fig. 5

Log P vs 1/T for  
B, B<sub>2</sub>O<sub>3</sub>, C  
Equilibrium.



## 2.7 Complex, Ultrahigh Temperature Composites

One of the materials made available to the program but not tested was a complex composite from Babcock & Wilcox, examined in the course of their PRDA program on ultra-high-temperature composites.

By weight, this material is 67.7% AlN, 22.1% SiC, and 10.2% BN. It was anticipated that the AlN and SiC would form a solid solution, with the BN present as a dispersed toughening phase. X-ray diffraction studies of the material fabricated indicated, however, that the starting materials retained their individual crystallographic phase identities.

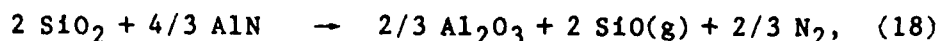
The AlN and SiC were used in such proportions that the oxide surface layer would have a composition corresponding to mullite,  $3\text{Al}_2\text{O}_3 \cdot 2\text{SiO}_2$ . X-ray diffraction of the surface material after high temperature exposure showed mullite and alumina. Amorphous phases also were found in some of the thermally treated samples.

The estimation of gas phase species and pressures in this system is more difficult than the simple binaries considered above. Rigorous equilibrium conditions are ruled out. In the usual model of a protective oxide layer, a diffusion gradient of oxygen is assumed between the exposed surface and the oxide/substrate interface. Precise application of this model would find the most energetic oxidation, that of AlN in the present case, occurring nearest the interface, then SiC at a somewhat higher oxygen potential, and finally BN nearest the free surface. Such a model, however, exceeds our knowledge of kinetic and transport properties.

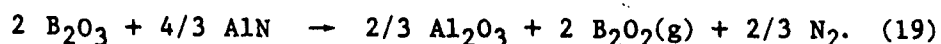
The workable assumption will be made that at the interface the oxide product species may all contact all of the phases in the composite.

As in earlier assessments, the projected attack at the oxide/substrate interface involves the interaction of oxide species, acting as oxidizing agents, with substrate components.

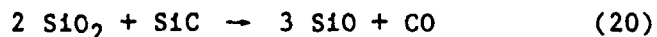
For the present system, AlN is the most powerful reducing agent over the temperature range considered, i.e. up to 2200 K or 3500° F, the processes leading to the highest vapor pressures are:



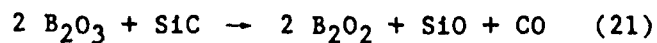
and



(Because of the increasing stability CO with increasing temperature at somewhat higher temperatures the reactions:



and



would become dominant.)

In predicting the thermochemical behavior in these systems there is a problem associated with multiple gaseous products. It has been arbitrarily assumed that the gaseous products will maintain stoichiometric relationships, i.e. their pressures will be in the same ratio as they appear in the chemical equation.

It is probable that this approach will overestimate the SiO(g) and B<sub>2</sub>O<sub>2</sub>(g) pressures at low pressures. The operation of the protective oxide layer assumes that oxygen diffuses in through the oxide layer and reacts at the interface. In the case of nitrides this means that the product nitrogen must diffuse out from the interface. The nitrogen activity at the interface must be equal or greater than that of the surrounding atmosphere.

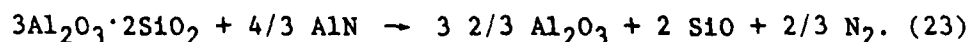
At higher temperatures and pressures, where we may expect to see failures by detecting gas species as the film is ruptured, the arbitrariness is less serious.

In addition to SiO and B<sub>2</sub>O<sub>2</sub>, the partial pressure of B<sub>2</sub>O<sub>3</sub>(g) is easily calculated assuming the activity of B<sub>2</sub>O<sub>3</sub> in the condensed phase is approximately unity. The phase diagram of the Al<sub>2</sub>O<sub>3</sub>/SiO<sub>2</sub>/B<sub>2</sub>O<sub>3</sub> does not show any ternary compounds but at the highest temperatures, above say 2000K (3100°F), the condensed phase would be present in a liquid phase in which it's mole fraction could be as low as 0.14. The pressures of species derived from B<sub>2</sub>O<sub>3</sub> may thus be overestimated in the higher temperature range.

The expected pressure of BO(g), more favorable for spectroscopic determination, is calculated from the reaction,

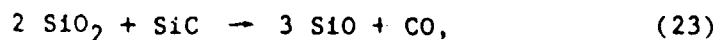


It was noted above that Al and Si were present in the composite in proportions that should yield the composition of mullite upon oxidation. The to the extent that it is combined in mullite the activity of the SiO<sub>2</sub> is reduced. One can substitute the following reaction for the SiO<sub>2</sub> reaction,



The "burying" of the SiO<sub>2</sub> in mullite increases the free energy of reaction by some 25-35 kJ over the temperature range and reduces the SiO pressure to a value comparable to that of B<sub>2</sub>O<sub>2</sub>.

Over most of the temperature range the highest CO pressure derives from the reaction



but at the highest temperature the reaction



results in a higher CO pressure.

Clearly any Si produced would be temporary. As the reaction front moved into the matrix any Si left behind would encounter increasing oxygen potential and revert to  $\text{SiO}_2$ .

The calculated pressures are shown in Fig. 6 as  $\log P$  vs  $1/T$ .

The line for CO shows the crossing from two sources at ca. 2070 K.

When the expected gas species pressures estimated of this ultra-high-temperature composite are compared with the pressures modeled previously for simpler, and presumably also lower temperature, materials it is striking that the total estimated pressures are in fact higher at the same temperatures.

In thermodynamic terms it is the outstanding stability of  $\text{Al}_2\text{O}_3$  that accounts for this. Although AlN is very stable against thermal decomposition to the elements, this stability is not sufficient to offset that of  $\text{Al}_2\text{O}_3$ . As the temperature goes higher the increasing free energy of CO makes SiC more and more powerful as a reducing agent.

In assessing the stability of any metal compound; nitride, carbide or boride, the stability with respect to corresponding metal oxide must be considered as well as the stability of the compound itself if the material is in fact to be exposed to an oxidizing environment.

### 3.0 Kinetic Considerations

It should be noted that all of the thermochemical results that are presented here are based on the assumption that the rate controlling

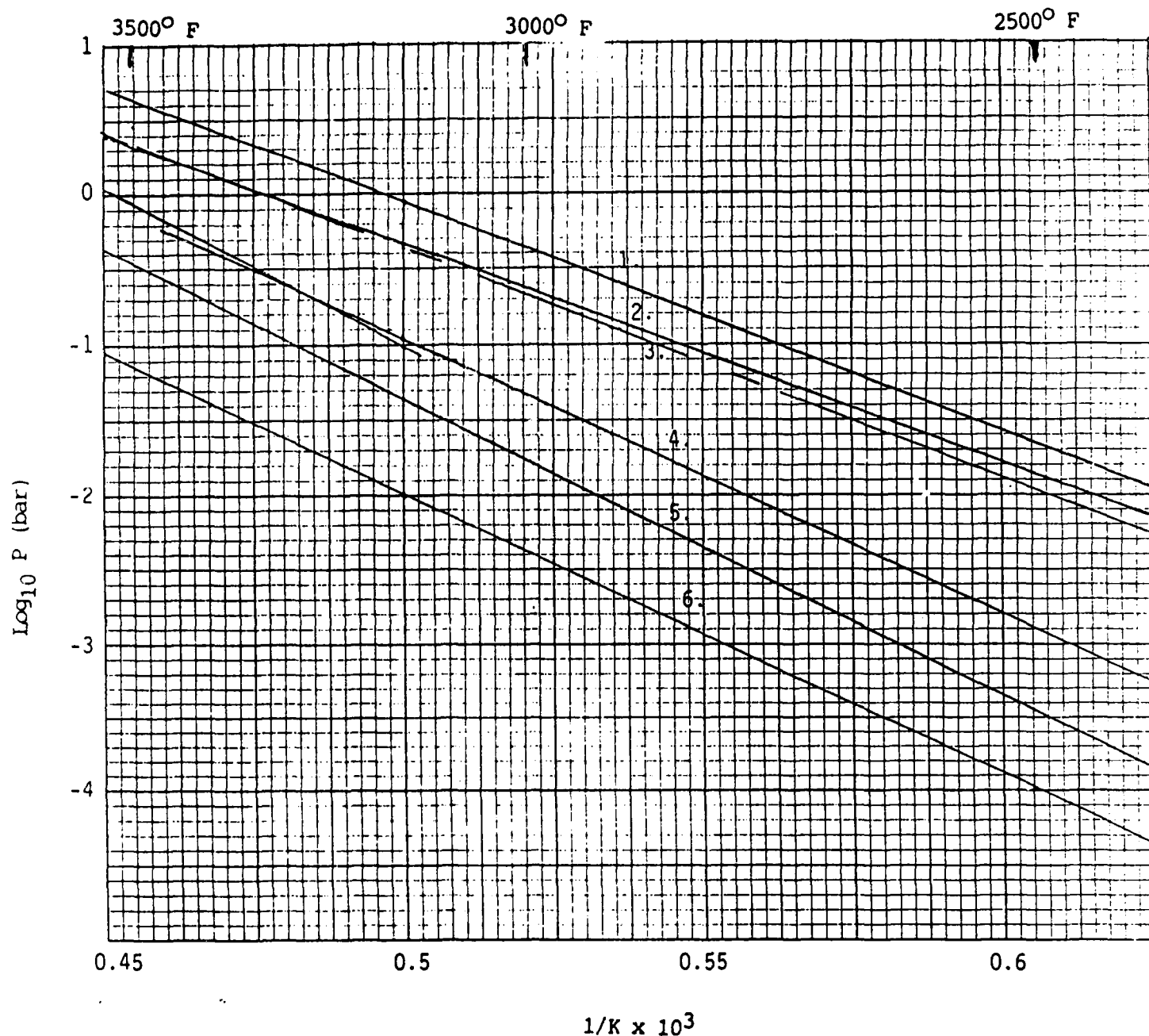


Fig. 6

Calculated pressures at the interface of a product oxide layer in contact with an AlN, SiC, BN composite

1. SiO (SiO<sub>2</sub> source)
2. B<sub>2</sub>O<sub>2</sub>
3. SiO (mullite source for SiO<sub>2</sub>)
4. CO
5. B<sub>2</sub>O<sub>3</sub>
6. BO

process in the development of the protective  $\text{SiO}_2$  layer is the transport of oxygen from the environment to the  $\text{SiO}_2$ /substrate interface. This means that for all of the systems here considered the interface is a strongly reducing environment.

In the case of  $\text{Si}_3\text{N}_4$  the overall development of the reaction requires that  $\text{N}_2$  be removed from the interface. Where either  $\text{SiC}$  or  $\text{C}$  are involved, carbon must be removed from the interface, as  $\text{CO}$  diffusing through the  $\text{SiO}_2$  layer.

In the case of  $\text{SiC}$ , it has been suggested that  $\text{CO}$  diffusion through  $\text{SiO}_2$  might become rate limiting. However Cappelen, Johansen, and Motzfeldt (2) found the rate of oxidation to be almost ten times as rapid with  $\text{H}_2\text{O}$  as with oxygen. The increased rate is attributed to increased mobility and solubility of  $\text{H}_2\text{O}$  compared to oxygen. If  $\text{CO}$  transport through  $\text{SiO}_2$  were rate limiting in oxidation in dry  $\text{O}_2$ , the consequence in  $\text{H}_2\text{O}$  oxidation would be film disruption.

$\text{CO}$  is somewhat smaller than  $\text{O}_2$  suggesting favorable mobility. The writer is not aware of any solubility data.

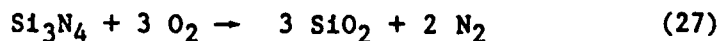
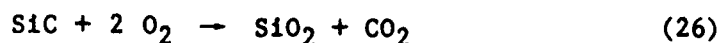
An obvious question is why the inward diffusing  $\text{O}_2$  does not react with the  $\text{CO}$  to produce  $\text{CO}_2$ , which would be practically immobile. Cappelen et al suggest that the concentrations are sufficiently small that interaction is unlikely. An alternative is to consider the required reaction,



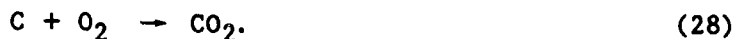
In the absence of the free radical environment of a flame, it seems plausible that a binary reaction would be required. Using gas phase data at 1800 K, the heat of reaction is -5.7 kcal and the free energy of reaction is 1.9 kcal, i.e. the reaction is near neutral even in the gas phase and a sufficient  $\text{CO}$  concentration would remain to carry some oxygen flux. In the condensed phase, the same

increased molecular size of  $\text{CO}_2$  which would reduce mobility would, in all likelihood, increase the free energy of reaction (25), shifting the equilibrium to the left.

If any step in the overall process other than the diffusion of oxygen through the protective  $\text{SiO}_2$  layer becomes limiting or contributes significantly to the limitation, then the oxygen activity (pressure) at the interface will move in the direction of the oxygen pressure of the environment. In this case, the reactions presented previously will be overwhelmed by the following:



and



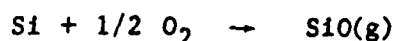
In every case the pressures resulting from these reactions far exceed those from the reactions considered previously, in which  $\text{SiO}_2$  is the oxygen source.

The model of a process limited by diffusion of oxygen through a condensed phase cannot be appropriate to an unoxidized material, though some degree of oxidation may occur in fabrication.

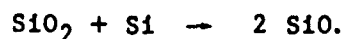
For materials which form volatile lower valent oxides, as do both Si and B, it is sometimes observed that at low oxygen pressures the volatile lower oxide evaporates as fast as oxidation can occur, leaving a fresh surface for oxidation to continue. For such materials, as the oxygen pressure increases a pressure is reached at which the higher valent, non-volatile oxide forms, covering the surface and resulting in a transition to the condensed phase diffusion limited process of the oxide scale is in fact protective.

The classic paper of Wagner (3) provides a mass transport limited model predicting an active-passive transition in Si oxidation at low, and predictable, oxygen partial pressure. Reasonable qualitative agreement with this model was obtained by Hinze and Graham (4) for the oxidation of Si and SiC, though with some complex behavior for Si. Gulbransen and Jansson (5) employed a similar model to elucidate the Si and SiC oxidation processes, but under molecular flow conditions.

The original Wagner model was developed on the postulate of balanced oxygen flow to and from the surface at steady state. In the case of Si, the SiO leaving the surface providing an oxygen atom flux equal to the inward flux of O<sub>2</sub>. The chemical reaction was assumed to be very fast. At low oxygen pressures, the SiO pressures of the reaction

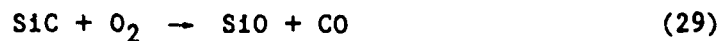


would be less than the equilibrium pressure for the reaction



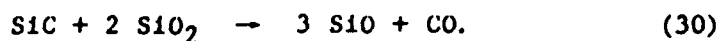
When the oxygen pressure reaches a value such that the surface equilibrium concentration of SiO in reaction (30), SiO<sub>2</sub> forms, the oxygen can reach the interface only by diffusion through the SiO<sub>2</sub>, and the oxidation shifts to the passive regime.

On an analogous basis, one might expect the reaction

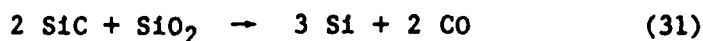


in the case of SiC, with the combined SiO and CO flux balancing the O<sub>2</sub> flux. The critical condition for active passive transition being that the SiO and CO concentrations at the surface reach the equilibrium values for the equilibrium,





Gulbransen and Hinze and Graham found that their experimental data for the active/passive were more nearly in accord with the assumption that the oxygen flux carried by CO in the reaction



Balanced the in  $\text{O}_2$  from the environment.

The critical oxygen concentrations for both equilibrium assumptions and for the analog of (29) and (30) for  $\text{Si}_3\text{N}_4$  are shown in Fig. 7.

Because of its significance in semiconductor fabrication the Si oxidation process has received the greatest attention. A widely cited model is that of Deal and Grove (6). This model, sometimes referred to as the linear-parabolic or LP model, which has correlated a great many observations, assumes an initial linear growth process followed by a parabolic stage. The linear stage is assumed to be associated with a surface reaction rate limitation. In the subsequent parabolic stage the rate limiting process is diffusion of reactants through the thickening oxide layer. Temperature dependence of rates are consistent with observed diffusion processes in the parabolic stage. For the linear stage an activation energy of 45.3 kcal is derived from the data. This is comparable to the estimated Si-Si bond strength. If the surface reaction rate is sufficiently low the Wagner assumption of near zero oxygen concentration at the clean surface would not hold. However, the reaction rates reported by Gulbransen et al exceed the linear rates derived by Deal and Grove for Si. (Though Costello and Tressler applied the Deal, Grove model to SiC (7), the scatter of the data precluded a meaningful estimation of the linear rate constant.)

The available literature indicate that three stages may be required to fully describe the behavior of Si, and Si containing materials such as SiC and  $\text{Si}_3\text{N}_4$ : a gas phase transport limited active regime

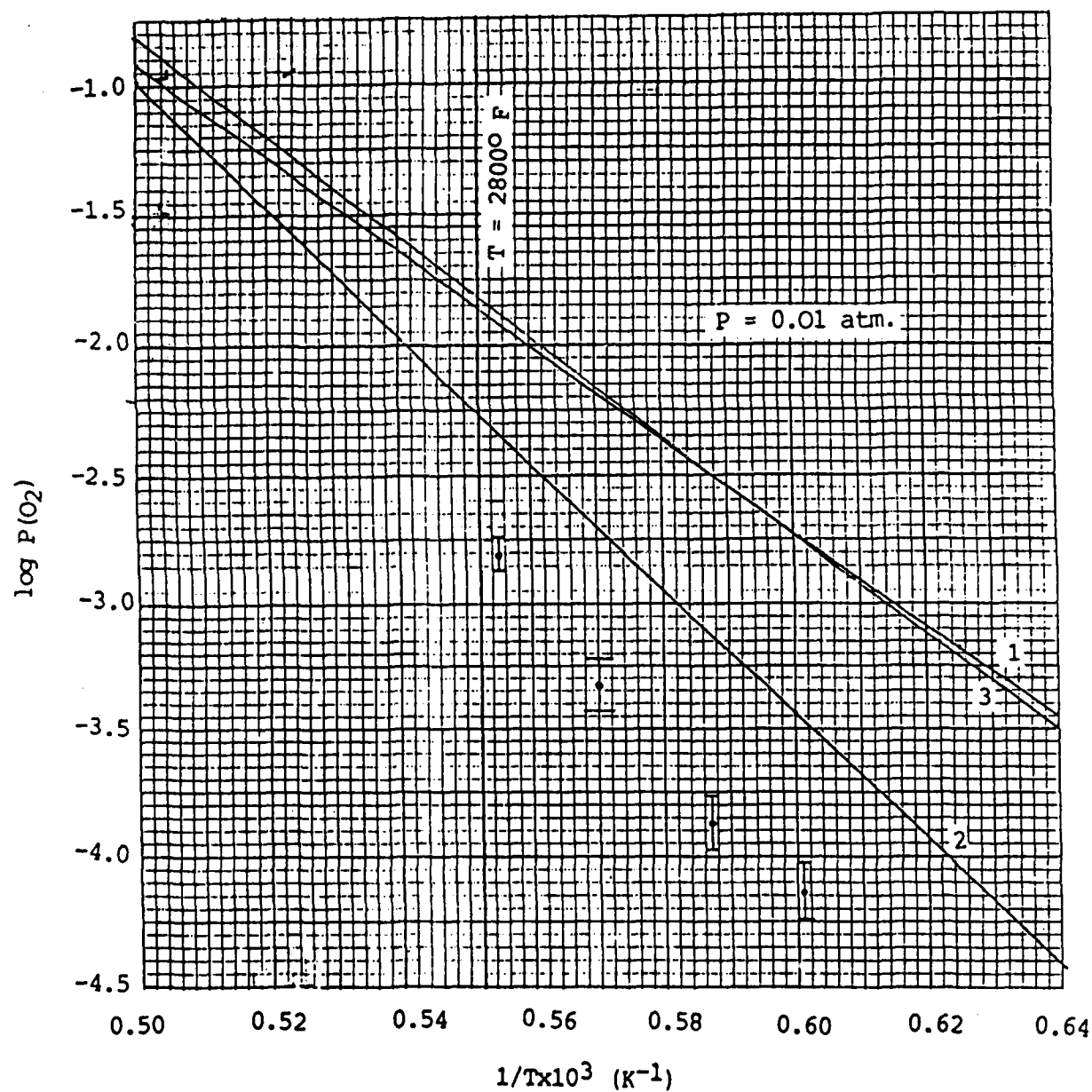


**Fig. 7**

Critical oxygen pressures for active/passive transitions.

1. Based on equilibrium of,  
 $2 \text{ SiO}_2 + \text{SiC} \rightarrow 3 \text{ SiO} + \text{CO}$
2. Based on equilibrium of,  
 $2 \text{ SiC} + \text{SiO}_2 \rightarrow 3 \text{ Si} + 2 \text{ CO}$
3. Based on equilibrium of,  
 $3/2 \text{ SiO}_2 + 1/2 \text{ Si}_3\text{N}_4 \rightarrow 3 \text{ SiO} + \text{N}_2$

Points with error bars taken from ref. (4), Fig. 12

at low oxygen pressures, a linear regime in which the surface is covered but by a layer so thin that surface reaction rate rather than oxygen transport in the condensed phase is limiting, and the parabolic regime in which the oxidation rate is dependent upon the rate of  $O_2$  transport through the surface oxide layer.

References:

- (1) Private communication, Jim Sheehan, General Atomics
- (2) H. Cappelen, K. Johansen, and K. Motzfeldt,  
Acta Chim. Scand. A35 247 (1981)
- (3) C. Wagner,  
J.Appl.Phys. 29 1295 (1958)
- (4) J. W. Hinze and H.C.Graham,  
J.Electrochem.Soc. 123 1066 (1976)
- (5) E. A. Gulbransen and S.A.Jansson,  
Oxid.Met. 4 181 (1972)
- (6) B. Deal and A. Grove,  
J.Appl.Phys. 36 3770 (1963)
- (7) J. A. Costello and R. E. Tressler,  
J.Amer.Cer.Soc. 69 674 (1986)

## SURFACE TEMPERATURES OF SMALL LASER-IRRADIATED TARGETS

M. SPARKS \*

September 30, 1987

There are a number of well known results for the surface temperatures of laser-heated solids that are valid under various conditions. However, none of these apply to the present case of small targets under continuous laser irradiation at irradiance levels below the mass-removal threshold. The results of the calculations for this case below are remarkably simple when the following assumptions are satisfied:

1. The thermal time constant

$$t_{thR} \approx R^2/4k \approx 3.25E-2 \text{ s } [0.7 \text{ s}]^1 \quad (1)$$

for thermal diffusion over distance R (target radius), and the thermal time constant

$$t_{thL} \approx L^2/4k \approx 5.20E-3 \text{ s } [0.1 \text{ s}] \quad (2)$$

for thermal diffusion over distance L (target thickness) are short with respect to the heating time (the time required for the

\* BDM Corporation

laser to heat the target to the final steady-state temperature  $T_f$  in the absence of cooling of the target)

$$t_f = (T_f - T_0)CV/P = 0.62 \text{ s } [0.57 \text{ s}], \quad (3)$$

where  $T_f$  is the final steady-state temperature,  $T_0$  is the initial temperature, and the other parameters are listed under equation (4).

These approximations are summarized as follows:

$$t_{thR} \ll t_f, \quad t_{thL} \ll t_f. \quad (4)$$

2. The transmittance of the target is zero. Specifically, all of the irradiance that is not reflected is absorbed in the target. Thus, the absorptance  $A$  is

$$A = (1 - R_{ref}). \quad (5)$$

3. The absorptance and emittance are from very thin surface layers. That is, the absorption lengths for both the laser radiation and the thermal-radiation spectrum are short with respect to the target thickness.

The numerical values in equations (1) through (4) that are not in brackets are for silicon carbide and those in brackets are

Target radius	$R = 0.15 \text{ cm}$ [same]
Target thickness	$L = 0.06 \text{ cm}$ [same]
Refractive index <sup>2</sup>	$n = 2.56$ [XX value needed XX]
Reflectance	$R_{\text{ref}} = 0.192$ [0.09 measured]
Absorptance $(1 - R_{\text{ref}})$	$A = 0.808$ [0.91]
Heat capacity	$C = 2.42 \text{ J/cm}^3\text{K}$ [2.0 $\text{J/cm}^3\text{K}$ , verify]
Thermal conductivity <sup>3[4]</sup>	$K = 0.42 \text{ W/cmK}$ [ $1.57\text{E-}2 \text{ W/cmK}$ ]44
Thermal diffusivity	$\kappa = 0.173 \text{ cm}^2/\text{s}$ [ $8\text{E-}3 \text{ cm}^2/\text{s}$ ]
Surface area	$A_{\text{srf}} = 2\pi R(R + L) = 0.198 \text{ cm}^2$ [same]
Volume	$V = \pi R^2 L = 4.24\text{E-}3 \text{ cm}^3$ [same]
Reradiation emittance	$\epsilon = 1$ [same]
Absorbed power	$P = 32(0.808) = 28.5 \text{ W}$ [ $26(0.91) = 23.7 \text{ W}$ ]
Laser-beam dimensions	
( $1/e^2$ axis lengths)	$D_{\text{major}} = 0.24 \text{ cm}$ [same]
	$D_{\text{minor}} = 0.18 \text{ cm}$ [same]

The experimental results are as follows:

final (steady-state) front-surface temperature

$$T_{\text{front}} = 1.943 \text{ K} [1903 \text{ K}]$$

final temperature difference  $T_{\text{front}} - T_{\text{rear}}$

$$T_{\text{dif}} = 30 \text{ K} [120 \text{ K, very roughly}]$$

time constant for approach to the steady state

$$t_f \approx 3.5 \text{ s [same]}.$$

Since the approximations of short time constants in equations (4) are well satisfied for silicon carbide, the calculation of the surface temperature is trivial because the temperature remains very nearly spatially constant throughout the target at all times of interest. Thus, the steady-state temperature is obtained simply by equating the absorbed power  $P$  to the power loss by thermal reradiation

$$\epsilon \sigma T_f^4 A_{\text{surf}}.$$

This gives

$$T_f = (P/\epsilon \sigma A_s)^{1/4} = 2,240 \text{ K [2,140 K]}, \quad (6)$$

in excellent agreement with the experimental value of 1,943 K [1,903 K].

The difference between the front-surface and rear-surface temperatures is estimated as follows: Approximately half of the reradiation is from the rear surface for the thin targets. Thermal conduction carries this energy from the front surface where it is absorbed to the rear surface where it is radiated.

Equating the thermal current

$$J\pi R^2 = -K(dT/dx)\pi R^2 = (KT_{dif}/L)\pi R^2$$

to the power radiated from the rear surface

$$P/2$$

gives the steady-state heat-conduction equation

$$(KT_{dif}/L)\pi R^2 = P/2 \quad (7)$$

which gives

$$T_{dif} = PL/2\pi R^2 K = 29 \text{ K [640 K formally]}, \quad (8)$$

in excellent agreement with the experimental value of 30 K for silicon carbide. The value of 640 K for silicon nitride is a poor estimate because the approximations in equation (4) are not satisfied. An improved calculation for silicon nitride is discussed below.

The time  $t_f$  for the approach to the steady state is taken as the intersection of linear temperature increase for the case of no cooling



$$(T_f - T_0) = Pt/CV,$$

(9)

(which is obtained directly from energy conservation) with the constant steady-state value. This gives the expression for  $t_f$  in equation (3).

The numerical value of 0.62 s [0.57s] in equation (3) is a factor of 5.6 [6.1] shorter than the experimental value of 3.5 s [3.5s]. This difference is too great to be explained by known sources of errors. A lower thermal conductivity could give rise to a longer time constant if the thermal conductivity were so low that equations (4) were not satisfied. However, the difference between the front-surface and back-surface temperatures would no longer be correct. Furthermore, the thermal conductivity would have to be lower by two orders of magnitude in order to explain the long time constant for silicon carbide.

A lower absorptance (lower  $P$ ) would give rise to a longer time constant, but the final temperature would then be incorrect. An absorptance that was lower at the beginning of the laser pulse and was equal to one at the end of the pulse possibly could explain both the longer time constant and the final temperature. Such shortening of the absorption length is of course well known in laser damage experiments with pulsed lasers. However, such shortening is unlikely in the present case of continuous (cw) irradiation of impure silicon carbide and silicon

nitride targets. First, these targets are black (in the visible region). Second, the growing absorption sites that are responsible for the shortening in the pulsed case do not become very hot and grow under the slow heating of continuous operation.

In passing, it is important to realize that pure hexagonal silicon carbide is transparent from 0.2 to 12  $\mu\text{m}^2$ . By contrast, the targets used in the experiments are nearly black.

The time dependence of the temperature is easily calculated for the case in which the assumptions above are satisfied. Equating the rate of change of the target energy

$$CVdT/dt$$

to the net power into the target

$$P = \epsilon\sigma(T^4 - T_0^4)A_{\text{srf}}$$

and integrating the simple first-order differential equation gives

$$t_n = (1/4)\ln[(1 + T_n)(1 - T_n)] + (1/2)\arctan T_n, \quad (10)$$

where  $t_n = t/t_f$  and  $T_n = T/T_f$ . Equation (10) is useful as it stands, even though it cannot be solved explicitly for  $T_n$  as a

function of  $t_n$ .

At short times ( $t_n \ll 1$ ), equation (10) gives

$$T_n \approx t_n - (1/5)t_n^5 \quad (11)$$

and for very long times ( $t_n \gg 1$ ), equation (10) gives

$$T_n \approx 1 - \exp(-4t_n). \quad (12)$$

From equation (10) it is easy to show that the temperature follows the linear asymptote (first term in equation (11)) closely for  $t_n < 1$  and follows the constant temperature asymptote (first term in equation (12)) closely for  $t_n > 1$ . Thus, the approximation

$$T_n \approx t_n, \quad \text{for } t_n < 1 \quad (13a)$$

$$\approx 1 - \exp(-4t_n), \quad \text{for } t_n > 1 \quad (13b)$$

is sufficiently accurate for most applications. The asymptotes and a rough plot from equation (10) are shown in Fig. 1.

Next consider materials such as silicon-nitride for which the approximations in equation (4) are not satisfied. The difference between the front-surface and near-surface temperatures must be taken into account. The spatial variations

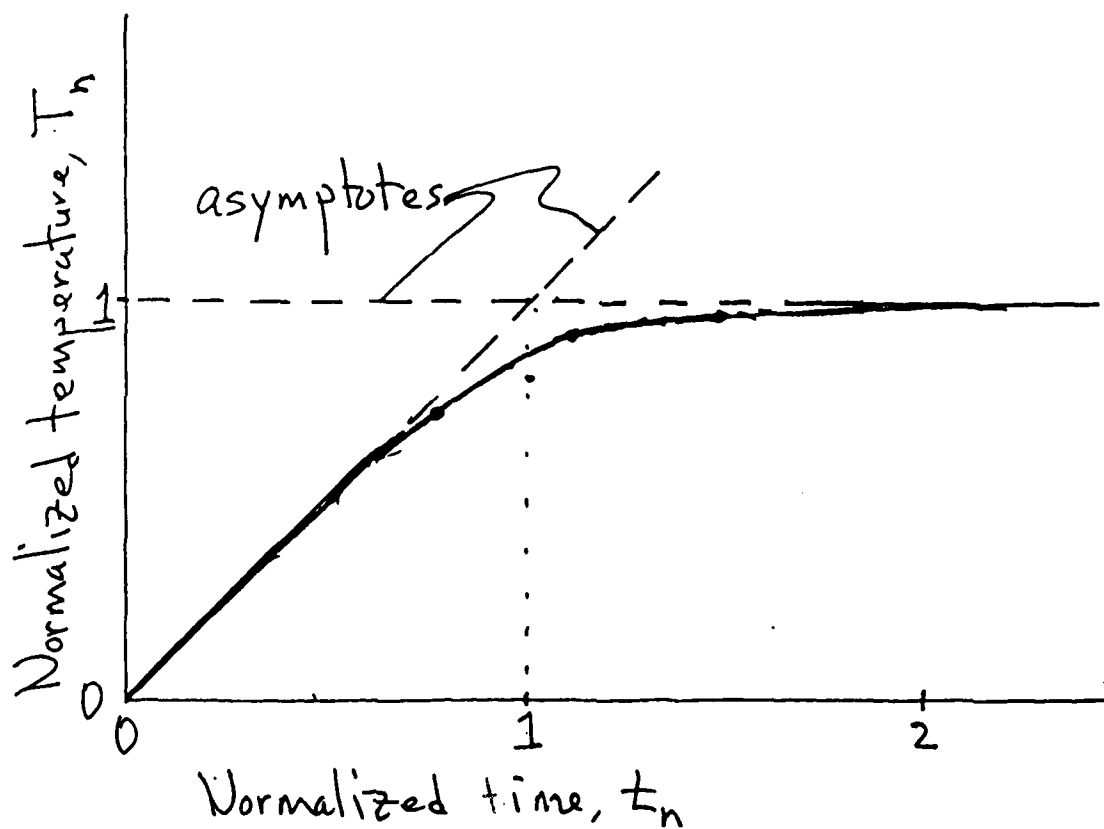


Fig. 1. Time dependence of the target temperature

across the surfaces are neglected. The steady state energy-balance equation (6) must then be replaced by

$$P = \epsilon\sigma\pi R^2 T_{\text{front}}^4 + \epsilon\sigma\pi R^2 T_{\text{rear}}^4 + \epsilon\sigma 2\pi RL(T_{\text{front}} - \Delta)^4, \quad (14)$$

where  $T_{\text{front}}$  is the front-surface temperature,  $T_{\text{rear}}$  is the-rear surface temperature, and  $\Delta$  accounts for the temperature difference between the front-surface temperature and the temperature of the rim of the target. Equation (14) can be written as

$$T_{\text{rear}} = [T_P^4 - T_{\text{front}}^4 - (2L/R)(T_{\text{front}} - \Delta)^4]^{1/4}, \quad (15)$$

were

$$\begin{aligned} T_P &= (P/\epsilon\sigma\pi R^2)^{1/4} \\ &= 2,770 \text{ K} \quad \text{for silicon nitride.} \end{aligned}$$

The temperature difference between the front and rear surfaces is determined by equation (7) with the right-hand side replaced by the correct rear-surface radiation cooling:

$$(KT_{\text{dif}}/L) = \epsilon\sigma T_{\text{rear}}^4 \quad (16)$$

Equations (15) and (16), along with

$$T_{dif} = T_{front} - T_{rear}, \quad (17)$$

determine the values of  $T_{front}$  and  $T_{rear}$ . These equations can be easily solved numerically. A simple estimate is obtained by neglecting  $\Delta$  in equation (15) and iterating equations (15) and (16) as follows: A value of  $T_{front}$  is assumed and the value of  $T_{rear}$  is calculated from equation (15). The value of  $T_{dif}$  is calculated from both equation (16) and equation (17). A new trial value of  $T_{front}$  is then chosen, based on the difference between the two calculated values of the temperature difference. The iteration is continued until the two values of  $T_{dif}$  are equal.

For silicon nitride this gives

$$T_{front} = 2,240 \text{ K} \quad (18)$$

and

$$T_{dif} = 300 \text{ K}. \quad (19)$$

The agreement between this calculated of 2,240 K from the front-surface temperature and the experimental value of 1,903 K is good. The difference between the calculated value of 300 K for the temperature difference and the experimental value of 120 K is not good. The difference may be the result of the inaccuracy in the experimental value for silicon nitride.